A DISSERTATION FOR THE DEGREE OF DOCTOR SCIENTIARUM

Bidirectional and Spectral Reflectance Properties of the *Cladina stellaris* and *Flavocetraria nivalis* lichens and the *Racomitrium lanuginosum* moss

Inger Solheim

May 1998

NORUT Information Technology
N-9005 Tromsø, Norway

Faculty of Science
Department of Physics
University of Tromsø, N-9037 Tromsø, Norway, Telephone +47 77 64 5150, Telefax +47 77 64 5580

Contents

Acknowledgments

I thank Alfred Hanssen for his patient proof reading, helpful suggestions, and help througout the project. I am grateful to Hans Tømmervik who had the original idea for this thesis, and who participated and provided botanical expertise during the field work and target collection, and for providing the photo in Figure 3.2.

A special thanks to Åsmund Hanssen for help with collecting the *Flavocetraria nivalis*, and Gunvor Solheim for help with preparing the *Flavocetraria nivalis* target.

This work would not have been possible without full access to the EGO facility and staff. I therefore thank Alois Sieber, Head of Advanced Techniques Unit, Space Applications Institute (JRC, Ispra), for the access to the lab. A special thanks to Brian Hosgood, Giovanni Andreoli and Jukka Piironen for help and expertise during the EGO experiment, and for providing auxiliary data througout the project. I thank Kjell Arild Høgda and Ola Engelsen for participation during the EGO campaign.

I thank Ola Engelsen for proof reading, providing the EMRPV1 code, and for the idea leading to Chapter 8. Bernt Johansen provided the classified Landsat-TM scene used in Chapter 8, and served as a reference in terms of the credibility of the results presented in Figure 8.1.

I thank Michel Verstraete for his constructive criticism in the early stages of this project, and for helping me to get the wonderful opportunity to work for five months at JRC. A special thanks to Yves Govaerts for suggesting the method I used in section 5.4.

I thank Arve Elvebakk for letting a physicist with no previous experience in botany follow his graduate course on bryophytes and lichens as environmental indicators. I thank Sigmund Spjelkavik for advise in connection with the Svalbard field work and for help identifying moss species.

I thank Elin Gulliksen at the University Library in Tromsø for ordering and copying numerous papers.

I acknowledge economic support from The Research Council of Norway, and NORUT IT, Norway under NORUT ITs strategic program GAIA. For the field work on Svalbard, I received economic support from The Norwegian Polar Institute. For the field work in Finnmark, I received a research grant from the Centre for Women's Studies and Women in Research at the University of Tromsø.

I thank Kjell Arild Høgda and Torbjørn Eltoft whom have been the formal advisors for this thesis.

Most of all I thank my dear Alfred, without his unconditional support, hundreds of dinners, enduring patientness and flexibility this thesis would never have been written.

Abstract

In this thesis we present a scientific investigation of the spectral and bidirectional reflectance properties of two lichen species, *Flavocetraria nivalis* and *Cladina stellaris*, and one moss, *Racomitrium lanuginosum*. The spectral and bidirectional characterizations were based on high-quality laboratory measurements made in the European Goniometer facility, at the Joint Research Center, Ispra, Italy. We found that the estimated reflectance factors were within 2% of their mean value, after corrections for an intensity drift in the illumination source, and non-Lambertian properties of the reference panel. We found that the spectral profile of the *Racomitrium lanuginosum* was similar to that of dry or stressed green vegetation. Moistened lichen canopies exhibited a higher reflectance factor than dry lichens in the visible and near-infrared spectral bands. Moistened moss however, had a lower reflectance than the dry moss. We compared our laboratory measurements with *in situ* spectral field measurements, and found an excellent agreement. Our goniometric measurements showed that the lichens are strongly backscattering canopies in both the visible and near-infrared parts of the spectrum. The moss however, scattered isotropically in the visible part of the spectrum, whereas it was strongly backscattering in the near-infrared part of the spectrum. We characterized our experimental bidirectional reflectance factors of the targets by means of a parametric and a physical model. By means of a statistical analysis, we showed that the parametric model was superior in terms of numerical convergence and flexibility. We applied cross-validation and bootstrap techniques to assess the accuracy of reflectance factor estimates. Lastly we demonstrated the possibility of simulating the top-of-the-atmosphere lichen reflectance factors based on laboratory measurements, and we explained how these results can be used to identify areas with a lichen cover of a Landsat-5 TM scene.

List of of Frequently Used Abbreviations and Acronyms

BRF Bidirectional Reflectance Factor

EGO The European Goniometric Facility

EMRPV1 A parametric BRF model (Engelsen *et al.* [30])

FOV Field of View

MISR Multi-angle Imaging Spectro-Radiometer

NIR Near-InfraRed

TM Landsat Thematic Mapper

PTFE Poly-Tetra-Fluoro-Ethylene

VPD Verstraete, Pinty and Dickinson [105, 147] BRF model

RF Reflectance Factor

RPV Rahman, Pinty and Verstraete [111] BRF model

6S Second Simulation of the Satellite Signal in the Solar Spectrum code

Chapter 1

Introduction

1.1 Nature and scope of the investigations

In this thesis we report novel experimental results from a bidirectional and multispectral laboratory measurement campaign carried out at the European Goniometer (EGO) facility, at the Joint Research Centre (JRC), Ispra, Italy. The objective of the project was to characterize the multi-directional spectral reflectance properties of common arctic- and sub-arctic vegetation types, through measurements and modelling. We present the spectral reflectance factors, and the measured and modelled bidirectional reflectance factors (BRF) for the *Cladina stellaris* and *Flavocetraria nivalis* lichens and the *Racomitrium lanuginosum* moss. We also show results from a coupling of the modelled BRF's with an atmospheric radiation transfer model. These results demonstrate how our findings can be used for classification of sub-arctic vegetation mapped from a satellite platform.

In the most general sense, remote sensing is the process of acquiring information about an object, surface or phenomenon, through analysis of data obtained without being in physical contact with the target of observation. Detailed descriptions of remote sensing principles can be found in a number of text books e.g. [3, 18, 47, 83, 114, 131]. Optical remote sensing of an object is based on the following basic assumptions. (1) The remotely sensed radiation has interacted with, and carries the unique signature of the target of interest. (2) The signature can be deciphered to obtain the unique characteristics of the object.

Radiant energy intercepted by a vegetative canopy is primarily scattered away from the leaf surface and/or towards the leaf interior. The scattered radiation is reflected, transmitted or absorbed by the leaves [153]. At the wavelength scale (μm) the amount of reflected, absorbed and scattered energy depends on the internal cell structure and pigmentation of the plant elements. Radiation scattered from the leaf interior is diffuse, whereas scattering from the surface often contains a strong specular component [150]. The spectral reflectance pattern characterizes

scattering at wavelengths comparable to the wavelength of light. At the canopy scale (cm to m), the directional scatter depends on the spatial organization of the canopy. Here we observe the so-called hot spot effect[1], which is a mutual shadowing phenomenon due to the finite size of the scattering elements [47, 76]. The canopy architecture can be characterized by the leaf area density and the leaf normal distribution [39, 43, 71, 77]. At the landscape length scale (m to km) we observe the scattering from heterogeneous surface of mixed vegetation. At this scale, the topography of the landscape also affects the scattering pattern.

The development of bidirectional reflectance factor functions [99] for ground cover types is particularly important for a quantitative analysis of pixels in a satellite scene, in terms of the angularly dependent reflectance [29]. This is exceedingly important for analysis of images acquired by satellites with variable view angle sensors, such as the High Resolution Visible instrument (HRV) on the SPOT satellite, or with wide-angle imagery sensors such as the Advanced Very High Resolution Radiometer (AVHRR) on the National Oceanic and Atmospheric Administration (NOAA) satellites. It is necessary to be able to compare observations at different angles or assimilate observations to represent a common geometric situation. In the near future, new opportunities will arise, as new generations of Earth observing satellites will be launched. Sensors capable of viewing the Earth's surface from various angles will play an important role in remote sensing over land, e.g., the Multi-angle Imaging Spectro-Radiometer (MISR) of NASA/JPL due to fly in 1998. Ground-based measurements are of great importance in developing the potential for monitoring the Earth's surface by the use of satellite data, since these measurements are critical in understanding the relationship between energy interaction with vegetation canopies and that observed in remote sensing measurements [150]. The *in situ* ground measurements are also necessary to obtain well-calibrated results from satellite data.

The main targets for our experimental investigations were lichens and bryophytes[2]. There has been reported 2000 species of lichens and 700 species of bryophytes in arctic and polar regions [86]. An estimated 80% of the bryophytes and 70% of the lichens have a circumpolar spread [86]. The traditional view is that lichens and bryophytes are effective colonizers during early stages of succession on dry land. Several studies have also been made of the evolution of bryophytes and lichens as secondary succession after destruction of vegetation [69, 86]. Lichens and bryophytes have long been recognized as sensitive indicators of environmental conditions. Certain species have been recognized to indicate the presence of specific mineral deposits, soil and site conditions, presence and level of atmospheric and aquatic pollutants, ages of rock surfaces, winter climate and snow depth etc. [5, 46, 64, 79, 86]. Successful monitoring of the lichen cover is therefore of

[1]The hot spot effect is also commonly referred to as the opposition effect, Heiligenschein or bright shadow [47].

[2]A primary division of plants comprising the true mosses and the liverworts [156]

great importance for monitoring the fragile arctic environment. As an economic resource some lichen species are important as grazing resources for reindeer and caribou [86, 89, 135], for evaporation control in perfumes, and for wool dyes.

The spectral profiles of lichens stand out as rather unusual among living plants. Most other types of vegetation, like mosses, grasses, shrubs and forest herbs, exhibit reflectance shapes much more similar to one another [102]. In habitats such as tundra and open woodland, mosses and lichens often constitute up to 70% of the ground cover. Hence, they are potentially observable from satellites. Lichen heaths in the arctic form where conditions are not favorable for flowering plants. This may be areas subject to frost disturbance, or thick long lasting snow cover. Moss heaths dominated by mat-forming *Racomitrium lanuginosum* are often characteristic for areas with strong winds and a porous volcanic substratum or stony grounds. Lichen mats often cover the floor of the circumpolar boreal forest, and is hence an important part of the remote sensing signature from these areas.

From an experimental point of view, lichens have a number of attributes which makes them particularly well suited for laboratory investigations. They have no root-system, which together with their small size makes them readily collectible and packed without stress to the thalli. Most lichens and some bryophytes have a high tolerance for irradiation, dehydration, temperature variations and water stress. Many mosses form tight cushions or large blankets, growing directly on rock or a thin soil substratum. This makes them readily movable. Furthermore their low growth rate makes them stable targets. The homogeneity and the physical size of this type of targets also make them well suited for laboratory studies.

1.2 Related publications

A substantial amount of experimental and theoretical effort has been carried out to characterize spectral and bidirectional reflectance of various surface types of the Earth. In this section, we briefly discuss some of the most relevant publications that are related to, or otherwise of interest to our work. We firstly discuss work dealing with spectral measurements of lichens, next we discuss some well known publications dealing with bidirectional measurements, and lastly we review some of the literature on BRF models.

1.2.1 Spectral measurements of lichens and bryophytes

Early directional reflectance measurements of lichens (*Cladina rangiferina*) were carried out in 1960 by Diggelen [140]. He needed a material with a "great number of irregular cups, pits or clefts" to model the lunar surface. His comparison of

lichen measurements with measurements of lunar crater floors showed a satisfactory agreement, with some minor deviations at large phase angles.

Petzold and Goward [102] made measurements with a Barnes Model 12 – 1000 Modular Multiband Radiometer (MMR) and a Spectron Engineering SE590 Spectrophotometer, of *Cladina stellaris*, *Flavocetraria nivalis*, *Cetraria ericetrum*, and *Stereocaulon paschale*. The measurements were acquired in the vicinity of Schefferville, Quebec. They found that lichens exhibited a stepped reflectance profile, similar to that of vascular plants, except that the step between visible and near-infrared was smaller. They also found that for *Cladina stellaris* the absorption of blue wavelengths was stronger than for other vegetation.

Mulhern [94] also used a SE590 to make spectral measurements of *Cladina stellaris*, *Flavocetraria nivalis*, *Cladina arbuscula*, *Stereocaulon spp.*, *Cladina rangiferina* and several sub-arctic vascular plants, shrubs and moss genera like *Racomitrium lanuginosum* and *Sphagnum spp.* Her study locations were stratified to represent regional variations in the dominant lichen composition of landscapes throughout the circumpolar sub arctic. She found similar lichen reflectance characteristics as Petzold and Goward [102]. She also found that lichens can be spectrally similar to a certain moss (*Racomitrium lanuginosum*) and non-vegetated soils. Another *in situ* measurement campaign of spectral reflectance of lichens carried out by using a hand-held spectrometer was reported by Meredith [89].

In connection with the Boreal Ecosystem-Atmosphere Study (BOREAS) in Northern Manitoba, Canada, the spectral reflectance of the forest floor was measured by [130]. Some of the forest floor areas measured had a lichen coverage of up to 30%.

An early measurement series of the spectral properties of plants, using an integrating sphere attachment to a spectrophotometer was performed by Gates *et al.* [34]. Among other investigations, they examined selected lichen species in both dry and wet states. They found that there were no "prominent" features of the spectral reflectance of lichens distinguishing them from higher order plants, with the possible exception is the absence of a strong green peak of spectral reflectance around 550 nm which occurs for the higher plants. They also found that the wet lichens reduced the reflectance in the visible and increased the reflectance in the near infrared.

Laboratory measurements with a spectrophotometer (400 – 1400 nm) of several lichen species in dry and wet states have been reported by Gauslaa [35]. Cox *et al.* [17] investigated the reflectance of *Cladonia mitis* in dry and wet states, and soaked in copper sulphate solution baths.

The decline of lichens in South Varanger, Norway and in the Nikel and Monchegrosk area, Russia, has been documented by NORUT IT in several reports and papers [52, 127, 135, 137, 136, 138]. These studies were based on Landsat MSS and TM data. Similar studies have been performed around Cu-Ni smelters in Sudbury in Canada [31] and from Kokkola in Finland [139]. Lichen as a grazing resource for reindeer herds have been mapped on the basis of Landsat

images in several studies by Johansen *et al.* [60, 61, 62].

We have come across very few publications on spectral measurements of bryophytes. However, in one very interesting paper presented by Hapke *et al.* [48], they use goniometric measurements with a circularly polarized light source to investigate the cause of the hot spot. One of their targets in this study was a moss of the *Bryales* species. Their results indicate that the primary cause of the hot spot in most vegetation is shadow hiding, whereas in vegetation with a large number of wavelength sized structures, like for the *Bryales* moss, the hot spot is dominated by coherent backscatter [7, 87, 92].

1.2.2 Directional measurements of vegetation

Bidirectional reflectance data of various vegetation canopies have been collected in field and in laboratories over the past few decades. Many of these data sets have been used to develop, test, or invert BRF models. In the following we list some of the most frequently cited and interesting investigations.

Deering *et al.* [19, 20, 21] have been involved in several large campaigns e.g. First International Satellite Land Surface Climatology Project (ISLSCP) Field Experiment (FIFE) and BOREAS, where field bidirectional reflectance data have been collected with the Portable Apparatus for Rapid Acquisition of Bidirectional Observations of Land and Atmosphere (PARABOLA) [19] apparatus. These measurements include both forest and grass land canopies. The PARABOLA BOREAS data [20] has been used to invert several BRF models [29, 30].

The Remote Sensing Laboratory of the University of Zürich has constructed a transportable field goniometer for the acqusition of BRF data under natural illumination [121, 122].

Early airborne directional measurements for savanna, bog, pasture land and coniferous forest were collected in seven narrow spectral regions by Kriebel [75, 74]. These data sets have been publicly available since 1977. Field directional measurements of various types of agricultural crops have been the target of many campaigns. Examples can be found in [6, 113, 141]. Kimes *et al.* [70, 73] has collected several directional reflectance data sets of corn, pine, hard-wood, grasslands, hard wheat, and plowed fields, amongst others.

Walter-Shea *et al.* [151] investigated canopy BRF measurements of grasses and soil from the FIFE site, with respect to biophysical properties like absorbed photosynthetic active radiation (APAR), leaf water content, and leaf age.

Laboratory measurements from the goniometric facility in Changchun, China have been reported by Strahler*et al.* [129] and Liang *et al.* [82]. In this campaign, BRF measurements were acquired for 1×1 m samples of wheat, soybean, and corn canopies.

1.2.3 Bidirectional reflectance models

In the following, we review some of the pertinent works on BRF models. Literature reviews of bidirectional reflectance models can be found in [39, 98, 97].

Goel [39] classified canopy reflectance models into four categories: geometrical models, turbid medium models, hybrid models, and computer simulation models. Another frequently used class of models are empirical models [145, 155]. The theoretical models have evolved significantly in recent years, and now often combine aspects from several of the model classes.

An empirical model describes the BRF in terms of suitable (phenomenological) mathematical functions. The goal of an empirical model is to give a satisfactory representation of the BRF for a wide range of canopies, rather than to explain the scatter explicitly in terms of physical parameters. Examples of empirical modelling can be found in [103, 154]. In the future, we expect that empirical models will be developed based on model free techniques like neural networks [49, 50, 55, 85, 160], or splines [67, 106].

An intermediate type of models are the semi-empirical models. The mathematical functions are chosen based on an understanding of the interaction between the radiation field and the surface. However, the parameters can not be interpreted in terms of biophysical or structural properties. Examples of this type of models can be found in [30, 54, 111, 119, 155]. The most important advantage of these models is their great ability to represent a wide variety of vegetation types and land covers.

In geometrical models, the BRF is derived from the theory of optics with a particular focus on the estimation illumination and shadowing within a given surface. These models often describe the scatterers as simple geometrical shapes like cones, cylinders etc. The geometrical models can be used to model sparse canopies where multiple scattering and mutual shadowing may be neglected. Several geometrical models are reviewed in [39].

In computer simulation models or Monte Carlo ray tracing models, the canopy reflectance is estimated based on a numerical ray to ray basis. The model can be used to generate synthetic BRF's of three-dimensional canopies of arbitrary complexity. All geometrical and physical quantities of the canopy elements are specified explicitly. With the aid of this type of model one can simulate canopies where the vegetation elements are specified by their optical properties, location and size. Examples of this type of model can be found in [37, 43, 45, 71, 117].

Analytical functions applied as approximations to the radiation transfer theory, emphasizes the representation of effects due to the orientation of the scatterers and the structure of the canopy. The advantage of using analytical functions is the ability to model the relation between backscattering, and the structure of the canopy. Generally, these models have three to five optical and structural parameters. Examples of analytical approximations to the radiation transfer theory can be found in [1, 47, 100, 118, 147].

In the turbid medium approach to the radiation transfer of a canopy, the canopy is divided into horizontal layers of small absorbing or scattering vegetation elements of given optical properties, orientation, and distribution. The optical and structural properties of each layer are assumed homogenious. A model in this class which has been given much attention is the Scattering by Arbitrary Inclined Leaves (SAIL) model by Verhoef [142]. This model has been tested, improved and further developed by many investigators or combined with other approaches, see e.g, [16, 33, 58, 77, 78]. Generally these models include many (e.g. seven in the original SAIL model) structural and optical parameters. This class of models has been criticized for the lack of ability to represent mutual shadowing and therefore also the hot spot [47]. In recent works, we have seen a tendency towards analytic solutions for the hot spot and single scattering component, combined with the Discrete Ordinate Method (DOM) [80] to approximate multiple scattering. Examples of this type of approach can be found in [38, 56, 59, 95, 96]. Examples of coupled models of soil-canopy and atmosphere can be found in [111, 144], among others.

1.3 Methods of investigation

We chose to concentrate our scientific efforts on performing an experimental study in a modern computer controlled laboratory facility. The main reason for our choice, was the wish to be able to control and manipulate variables in a systematic manner. The motivations for concentrating the effort to high-quality laboratory measurements, rather than top-of-canopy field measurements, or top-of-atmosphere satellite based measurements, were mainly:

- To perform all measurements in a controlled laboratory environment.
- To limit the study to direct collimated radiation, i.e., to minimize the effects of diffuse radiation and atmospheric disturbances.
- To avoid topographic effects.
- To use a homogeneous canopy of one species, placed on a known background.
- To be able to keep a stable irradiation source in a fixed position.
- To be able to characterize noise sources and the accuracy of the measurements.
- To be able to acquire a great number of measurements under stable laboratory conditions.

We chose to use one parametric and one physically based BRF model to represent the measurements. Both models have four unknown parameters. This is a relatively low number compared to many other BRF models (Section 1.2.3). The parametric model we chose [29, 30], was a variation of the Rahman, Pinty and Verstraete (RPV) model [111], henceforth called the EMRPV1 model. We selected this type of model because of its growing popularity, and because the RPV family of parametric BRF models has been proposed as part of the land surface product algorithm of the MISR instrument [30]. The physical model we implemented and inverted was the Verstraete, Pinty and Dickinson (VPD) [105, 147] model. The model was developed to predict the bidirectional radiation field over a fully covered, homogeneous, and semi-infinite canopy composed of leaves only. The canopy model contains physical parameters related to leaf orientation and density. Finally we simulated the top-of-the-atmosphere spectral signatures by means of the so-called 6S model [143, 144].

1.4 Organization of the thesis and main conclusions

The organization of this thesis is as follows: In Chapter 2 we review important basic concepts, theory and methodology of remote sensing, BRF modelling and parameter estimation. In Chapter 3 we characterize the chosen targets biophysically, primarily based on a literature study. In Chapter 4 we describe the Goniometric laboratory facility and the chosen measurement procedure. In Chapter 5 we characterize our measurements in terms of precision. We characterize the fluctuations in the irradiation source, and show how we can correct for this effect. We furthermore characterize the BRF of the reference panel, and explain how we can correct for the non-Lambertian properties. Last, we asses that the precision of the experimental BRF estimates are within 2% of their mean value after our proposed corrections.

In Chapter 6 we present the experimental spectral signatures of the chosen targets in dry and moist states. We compare our laboratory spectral signatures with those of field measurements. We observed that the geometrical organization of the canopy changed when the lichens were moisted. This in turn changed the spectral reflectance characteristics. We found that the moist lichens exhibit a higher reflectance factor (RF) than those of the dry canopies. The opposite was true for the moss sample.

In Chapter 7 we present our bidirectional measurements. Both lichen targets we investigated have a significant hot spot for both visible and near-infrared (NIR) wavelengths. The moss shows a quasi-isotropic reflectance pattern for visible wavelengths, but has a significant hot spot in the NIR. We modelled the data by means of the parametric EMRPV1 [29, 30], and the physical VPD [105,

147] models mentioned earlier. We found that the parametrical model was flexible because inversion results were valid for a large range of source zenith angles. Furthermore we found that the model was numerically stable because it converged to the same parametric solution, as long as a sufficient number of measurements were used for the inversion. The physical model was less flexible because we had to perform an inversion for each source zenith angle. The lack of stability also led to a convergence to different parametric solutions, depending on which specific measurements were included in the inversion data set, and in the initialization of the inversion. The biophysical interpretation of the model parameters was in this case questionable.

In Chapter 8 we used the modelling results of the parametric model in order to simulate the top-of-the atmosphere reflectance factor. The result was subsequently coupled to the analysis of a dense lichen cover in a Landsat-5 TM scene.

In Appendix A we have collected some of the larger tables commented in the text. In Appendix B we have included a description of all the datasets gathered during the project, including those that have not been explicitly commented or used in this thesis. The computer programs developed for this thesis have been written in IDL and C.

Chapter 2

Concepts and Theory

In this chapter we review important basic concepts, theory and methodology of remote sensing, BRF modelling and parameter estimation.

2.1 Remote sensing systems

Figure 2.1 illustrates the main principles and elements of a remote sensing system. The detector may be located on ground, airplane or on a space platform. Electromagnetic radiation emitted by the Sun propagates through the atmosphere and reaches the Earth's surface. The radiant flux is partially absorbed and partially scattered by the atmosphere. The Earth's surface is therefore irradiated both by direct flux from the Sun and by flux scattered from the surrounding hemisphere. Some of the incident flux is reflected by the Earth's surface in the direction of the detector. As the reflected flux passes trough the atmosphere, it is again absorbed and scattered. Only a fraction of the photons coming from the target surface reaches the satellite sensor, typically 50% for 450 nm, and 80% for 850 nm [143]. In addition to the flux scattered by the Earth's surface, the detector receives flux scattered by the atmosphere itself.

When the incident electromagnetic solar radiation reaches the Earth's surface, there are three possible fundamental interactions: reflection, absorption and transmission. The total flux that has interacted with the surface can thus be written as

$$\Phi_s(\lambda) = \Phi_r(\lambda) + \Phi_t(\lambda) + \Phi_a(\lambda) \tag{2.1}$$

where $\Phi_r(\lambda)$ is the reflected flux, $\Phi_t(\lambda)$ is the transmitted flux, and $\Phi_a(\lambda)$ is the absorbed flux. All flux components are functions of the wavelength λ. By dividing Eq. (2.1) by the incident flux $\Phi_s(\lambda)$ we get the dimensionless relation

$$1 = \rho(\lambda) + \tau(\lambda) + \alpha(\lambda) \tag{2.2}$$

where $\rho(\lambda)$ is the spectral reflectance, $\tau(\lambda)$ is the spectral transmittance and $\alpha(\lambda)$ is the spectral absorptance.

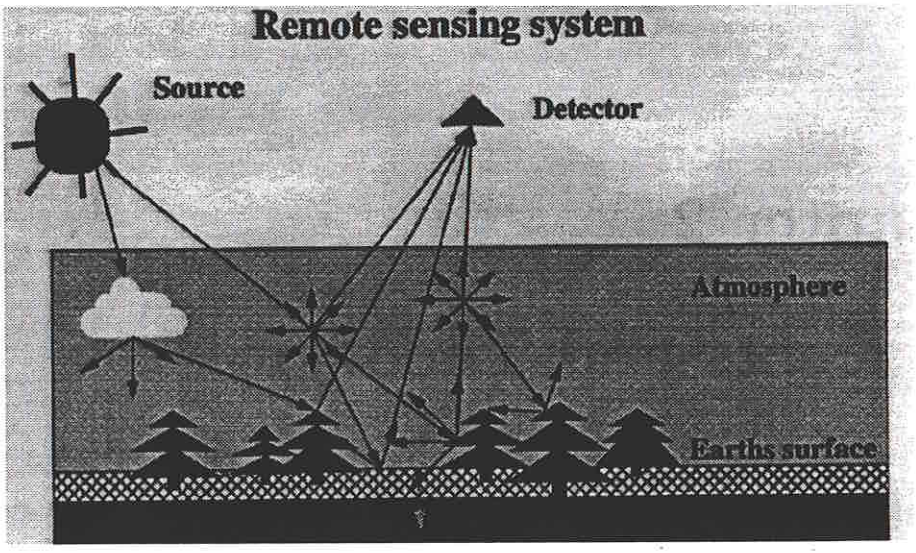

Figure 2.1: A remote sensing system.

The most important factors that determine the reflectance of a vegetation canopy are, incoming solar flux, optical properties of the vegetation elements (reflectance $\rho(\lambda)$, transmittance $\tau(\lambda)$), architecture of the canopy (leaf-angle distribution and leaf-area distribution) and scattering from the soil beneath the vegetation [39].

2.2 Radiative transfer theory

Radiative transfer theory has been developed to describe the scattering and propagation of electromagnetic radiation in multiple scattering media. It has been applied to study stellar and planetary atmospheres, the Earth's surface and oceans. The radiative transfer model is a partial integro-differential equation that describes the intensity variation of an electromagnetic wave affected by emission, absorption and scattering [15].

The basic assumption for radiative transfer model is that a medium scatters and emits the radiation incoherently and independently of each other. We further assume that the medium is illuminated by a highly collimated source that may be considered at an infinite distance above the medium, in a direction θ_s relative to the zenith, and that the medium is horizontally stratified. Derivations of the radiative transfer model can be found in [15, 47, 80, 84, 158], amongst others.

The radiative transfer equation for unpolarized radiation is given by

$$-\frac{\partial I(\tau,\omega_d)}{\partial \tau}\cos\theta_s = -I(\tau,\omega_d) + \frac{\bar{\omega_o}}{4\pi}\int_{4\pi} I(\tau,\omega_s)p(\tau,\omega_d,\omega_s)d\omega_s + \epsilon(\tau,\omega_d) \qquad (2.3)$$

where $I(\tau,\omega_d)$ is the intensity, τ is the optical thickness, $p(\tau,\omega_d,\omega_s)$ is the phase

function which gives the probability that radiance in the direction ω_s will be scattered into a solid angle about direction ω_d, $\epsilon(\tau, \omega_d)$ describes the radiation emitted by internal sources, θ_s is the source zenith angle, and $\bar{\omega_o}$ is the single scattering albedo defined by [84]

$$\bar{\omega_o} = \frac{\beta_s}{\beta_e} = \frac{\beta_s}{\beta_\alpha + \beta_s} \tag{2.4}$$

Here, β_s, β_e and β_α are the scattering, extinction and absorption coefficients, respectively. The single scattering albedo represents the percentage a of a light beam which will undergo scattering in a single scattering event.

2.3 The bidirectional reflectance factor

Nicodemus *et al.* [99] presented a unified nomenclature for specification of reflection in relation to the beam geometry of both the incident and reflected radiation. We present a review of the esential concepts used in this thesis. The best known concept from this work is the Bidirectional Reflectance Distribution Function (BRDF) which is defined as

$$f_t(\theta_s, \phi_s; \theta_d, \phi_d) = \frac{dL_d(\theta_s, \phi_s; \theta_d, \phi_d; E_s)}{dE_s(\theta_s, \phi_s)}, \qquad [sr^{-1}] \tag{2.5}$$

where (θ_s, ϕ_s) and (θ_d, ϕ_d) are the incidence and reflectance directions respectively, dL_d is the reflected radiance in the direction (θ_d, ϕ_d), $dE_s = L_s \cos\theta_s d\omega_s$ is the incident irradiance and $d\omega_s = \sin\theta_s d\theta_s d\phi_s$ is the solid-angle element within which the incidence radiance is confined. The BRDF is the ratio of the reflected radiance to the collimated incident flux per unit area. This quantity relates the directional radiance of the surface to the directional irradiance and directional source radiance, respectively. The BRDF describes the unique scattering properties of the surface, independent of the anisotropy of the incident radiation distribution [72]. The BRDF can take on any non-negative value. The case $f_t(\theta_s, \phi_s; \theta_d, \phi_d) = \delta(\theta_s - \theta_d; \phi_s - \phi_d)$, where $\delta(x, y)$ is the two-dimensional Dirac delta function, corresponds to a perfectly flat reflecting surface at which only perfectly specular reflectance occurs. The BRDF can never be measured directly because truly infinitesimal elements of solid angle do not include measurable amounts of radiant flux [99].

Reflectance is the ratio of reflected to incident flux [99]. The reflectance factor (RF) is defined as the ratio of the reflectance from the target surface to that of a perfectly diffuse surface under the same conditions of illumination and measurements [99]. Since diffuse reflection implies $f_t(\theta_s, \phi_s; \theta_d, \phi_d) \equiv 1/\pi$, we find

$$\frac{d\Phi_t}{d\Phi_{diff}} = \frac{dA \int_{\omega_s} \int_{\omega_d} f_t(\theta_s, \phi_s, \theta_d, \phi_d) L_s(\theta_s, \phi_s) d\Omega_s d\Omega_d}{(dA/\pi) \int_{\omega_s} \int_{\omega_d} L_s(\theta_s, \phi_s) d\Omega_s d\Omega_d} \tag{2.6}$$

where ω_s, ω_d are the solid angles of incident and reflected radiation, dA is an area element, L_s is the incidence radiance and $d\Omega_s = \cos\theta_s d\omega_s$, $d\Omega_d = \cos\theta_d d\omega_d$ are elements of projected solid angle of incident and reflected radiation. If we make the assumption that L_s is constant within the solid angle of incidence ω_s, L_s cancels along with dA is Eq. (2.6), and we get the general expression for the biconical reflectance factor [99]

$$\rho(\omega_s, \omega_d) = \frac{\pi}{\Omega_s \Omega_d} \int_{\omega_s} \int_{\omega_d} f_r(\theta_s, \phi_s, \theta_d, \phi_d) d\Omega_s d\Omega_s \tag{2.7}$$

When the solid angles ω_s and ω_d are infinitesimal, we again get the bidirectional reflectance factor

$$\rho(\theta_s, \phi_s, \theta_d, \phi_d) = \pi f_t(\theta_s, \phi_s, \theta_d, \phi_d) \tag{2.8}$$

If however $\omega_d = 2\pi$ we get the directional hemispherical reflectance factor

$$r(\theta_s, \phi_s, 2\pi) = \int_{2\pi} f_t(\theta_s, \phi_s, \theta_d, \phi_d) d\Omega_d \tag{2.9}$$

This quantity is also commonly known as the albedo. The diffuse or hemispherical albedo is equivalent to the bihemispherical reflectance factor

$$r(2\pi, 2\pi) = \frac{1}{\pi} \int_{2\pi} \int_{2\pi} f_t(\theta_s, \phi_s, \theta_d, \phi_d) d\Omega_s d\Omega_d \tag{2.10}$$

All the above quantities can be defined spectrally, and the albedo is often given as an average over all wavelengths.

The bidirectional or biconical reflectance factors are easy to estimate based on experimental measurements (see Section 4.5 for details). The term bidirectional reflectance factor (BRF), or sometimes simply reflectance factor (RF), is often used to describe field measurements. The approach is then that the target surface radiance is divided by the radiance of a reference surface. For a small field of view (FOV $< 20°$) these terms are appropriate [19].

2.4 A parametric bidirectional reflectance factor model

Rahman, Pinty and Verstraete [111], developed a parametric BRF model that has gained some popularity. In the following, their model will be referred to as the RPV model. The RPV model was developed to account for observed variability of reflectance measurements under laboratory and field conditions. Rahman *et al.* [111] coupled their model with a simple atmospheric radiation transfer model, and inverted it against NOAA/AVHRR data.

In this thesis we use the RPV model with the modifications implemented and presented by Engelsen *et al.* [30], hereafter called the EMRPV1 model. Engelsen

et al. tested the model on selected field BRF datasets, as well as simulated BRF data obtained by radiative transfer modelling.

The RPV models are a family of parametric models where mathematical functions are fitted to represent the BRF datasets. The model is semi-empirical in the sense that the mathematical formulation is based on an understanding of the physical interaction between the radiation field and the surface. However, the parameters derived from the model have no direct interpretation in terms of biophysical or structural parameters.

The EMRPV1 model used in this analysis uses the following expression for surface bidirectional reflectance factor [30]

$$\hat{\rho}_s(\theta_s, \theta_d, \phi; \rho_0, k, b, \bar{\rho}) = \rho_0 M(\theta_s, \theta_d, k) F(g, b) H(\bar{\rho}, G) \tag{2.11}$$

where θ_s and θ_d are the source and detector zenith angles, respectively. The relative azimuth angle ϕ is defined as the azimuthal angle between the source and detector arcs. A zero azimuthal angle indicates that the source is behind the detector. The parameter ρ_0 is the reflectance of the surface for illumination and viewing at zenith. The function $M(\theta_s, \theta_d, k)$ represents the variation in the reflectance field, and is given by

$$M(\theta_s, \theta_d, k) = \frac{\cos^{k-1}\theta_s \cos^{k-1}\theta_d}{(\cos\theta_s + \cos\theta_d)^{1-k}} \tag{2.12}$$

The numerator of Eq. (2.12) is the empirical model of Minnaert [91] ($\rho(\theta_s, \theta_d) = \rho_0 \cos^{k-1}\theta_s \cos^{k-1}\theta_d$) developed to describe the reflectance of the moon. The parameter k indicates the level of anisotropy of the surface. The non-unity denominator in Eq. (2.12) was included to get a better representation of the variations in the reflectance field [112]. Henyey-Greenstein (see e.g. [47]) introduced an empirical phase function given by

$$F(g, \Theta) = \frac{1 - \Theta^2}{(1 + 2\Theta\cos g + \Theta^2)^{3/2}} \tag{2.13}$$

This function was included in the RPV model in order to modulate the overall contributions in the forward and backward scattering. The parameter Θ controls the amount of forward ($0 \leq \Theta \leq 1$) and backward ($-1 \leq \Theta \leq 0$) scattering. The phase angle g is given by

$$\cos g = \cos\theta_d \cos\theta_s + \sin\theta_d \sin\theta_s \cos\phi \tag{2.14}$$

To speed up the inversion of the RPV model, and making it more reliable, the Henyey-Greenstein phase function given in Eq. (2.13) was replaced in [30] by the simple function

$$F(g, b) = \exp(bg) \tag{2.15}$$

where b is a shape parameter. In the EMRPV1 model. Eq. (2.15) yields a good approximation of the Henyey-Greenstein phase function for asymmetry factors $-0.3 \leq \Theta \leq 0.1$ [30].

The hot spot scattering effect is modelled by the geometrical factor

$$H(\bar{\rho}, G) = 1 + \frac{1 - \bar{\rho}}{1 + G} \tag{2.16}$$

where G is given by

$$G = (\tan^2 \theta_s + \tan^2 \theta_d - 2 \tan \theta_s \tan \theta_d \cos \phi)^{1/2} \tag{2.17}$$

and where $\bar{\rho}$ is the average measured reflectance factor.

2.5 A physical reflectance factor model

A physically based bidirectional reflectance factor model was developed by Verstraete, Pinty and Dickinson [105, 147]. Their model was developed to predict the bidirectional reflectance field over a radiometrically homogeneous scattering surface. The paper by Verstraete *et al.* [147] gives the theoretical foundation for the analytic model. In an accompanying paper, Pinty *et al.* [105] describes the parameterization and implementation, and they provide results from inversions on real data. The following basic assumptions were made

- The target is semi-infinite.
- The target behaves like a cloud of leaves, where the leaves are idealized as plates of finite size, with inclination given by a probability density distribution of leaf normals.
- The target is made up of finite size leaves for the single scattering case.
- The target is made up of infinitely small size leaves for the multiple scattering case.
- The target is horizontally homogeneous in the treatment of the divergence flux.

The model is a generalization of Hapke's bidirectional reflectance model [47] for particulate surfaces. The Verstraete *et al.* [105, 147] model incorporates the statistical orientation and geometrical arrangements of the leaves in a canopy. The formulation of the hot spot term in the Verstraete *et al.* model takes into account the joint transmission of the incoming and outgoing radiation. In [104], the Verstraete *et al.* model was compared with the Hapke model.

The bidirectional reflectance factor ρ presented by Pinty *et al.* [105] has the form

$$\hat{\rho}(\theta_s, \theta_d, \phi; \omega, \chi_l, \Theta, 2\tau\Lambda) = \frac{\omega}{4} \frac{\kappa_s}{\kappa_s \mu_d + \kappa_d \mu_s} [P_v(G) F(g, \Theta) + H(\frac{\mu_s}{\kappa_s}) H(\frac{\mu_d}{\kappa_d}) - 1] \tag{2.18}$$

where $\mu_s = \cos\theta_s$, $\mu_d = \cos\theta_d$ and $\phi = \phi_s - \phi_d$. The parameter $\kappa_i = \langle \cos\alpha_i \rangle$ is the average cosine of the angle between the leaf normal and the direction of the source α_i. Likewise, κ_d is the average cosine of the angle between the leaf normal and the detector. Note that κ can be estimated based on the leaf orientation distribution function (e.g [145]). In [105] the average leaf orientation distribution is approximated by

$$\kappa_i(\mu_i) = \Psi_1 + \Psi_2 \mu_i \tag{2.19}$$

where

$$\begin{aligned} \Psi_1 = &\quad 0.5 - 0.6333\chi_l - 0.33\chi_l^2 \\ \Psi_2 = &\quad 0.877(1 - 2\Psi_1) \end{aligned}$$

The function $P_v(G)$ accounts for the joint transmission of the incoming and outgoing radiation, and is approximated by

$$P_v(G) \approx 1 + \frac{1}{1 + V_p(G)} \tag{2.20}$$

where

$$V_p(G) = 4(1 - \frac{4}{3\pi}) \frac{G}{2\tau\Lambda} \frac{\mu_d}{\kappa_d} \tag{2.21}$$

and where G is the geometrical factor given in Eq. (2.17), and $F(g, \Theta)$ is the Henyey-Greenstein empirical phase function given in Eq. (2.13). The term $H(\mu_s/\kappa_s)H(\mu_d/\kappa_d) - 1$ approximates multiple scattering and H is given by

$$H(x) = \frac{1 + x}{1 + (1 - \omega)^{1/2} x} \tag{2.22}$$

The present model has four parameters:

ω – average single scattering albedo for the particles constituting the canopy

χ_l – leaf orientation distribution parameter. This parameter is used to estimate the average cosine of angle between the leaf normal illumination (κ_s) and observation (κ_d) directions. The parameter χ_l is negative ($\sim$ -0.4) for an erectophile canopy, zero for uniform and positive ($\sim$ 0.6) for a planophile canopy [105].

Θ – the asymmetry factor in the Henyey-Greenstein function, ranges from -1 for backward scattering to $+1$ for a forward scattering canopy.

$2r\Lambda$ – Λ leaf area density, r- the radius of the Sun flecks on the inclined leaf, which can be related to the average size of the voids between the leaves projected perpendicularly on the horizontal plane. The joint parameter $2r\Lambda$ controls the shape of the hot spot [105].

2.6 Stochastic processes and parameter estimation

The estimation of canopy parameters from reflectance data is often referred to as the *inversion problem* [39]. The solution of the inverse problem is often given as a central estimator (mean, median or maximum likelihood) of the model parameters. The central estimator should always be accompanied by an appropriate error bar or dispersion measure. The *stability* of the central estimator is defined as the property of being insensitive to small random errors in the data values. The *robustness* is the property that the central estimator being insensitive to a small number of large errors (outliers) in the data set [132]. In this thesis, the inversion problem refers to estimating model parameters based on experimental measurements. The model parameters thus provide a low-dimensional BRF representation of the targets. When we invert a model, such as those described in Sections 2.4 and 2.5, we are interested in estimates of a set of unknown parameters, using a finite set of sample values. We are interested in finding the sample distribution of the estimators, so that the respective mean and variance can be calculated with some degree of confidence. Thus, it is necessary to make some kind of probability statement with respect to the unknown values of the parameters.

Some of the techniques that may be used to solve the inverse problem are analytic solutions, systematic exploration of the model space, Monte Carlo methods or computation of the maximum likelihood. The most common approach to invert BRF models [146], is to minimize the total square error of prediction

$$e^2(x_1, x_2, \ldots, x_n) = \sum_{i=1}^{I} (\hat{\rho}(\theta_d, \phi, \theta_s) - f(\theta_d, \phi, \theta_s; x_1, x_2, \ldots, x_n))^2 \qquad (2.23)$$

where $\hat{\rho}(\theta_d, \phi, \theta_s)$ is a BRF estimate based on measurement for a given illumination, intrumentational and geometrical configuration, I is the number of measurements, $f(\theta_d, \phi, \theta_s; x_1, x_2, \ldots, x_n)$ is the predicted or modelled value for the same configuration, and $x_1, x_2, \ldots, x_n$ are the model parameters. The inversion procedure consists of finding the model parameters that minimize the error function. However, not all models turn out to be invertible. A model is regarded as non-invertible if it is not possible to retrieve a set of unique model parameters from error free data, i.e. data generated by the model itself. Some models are only invertible if the inversion procedure is initialized with parameter values

"close to" the correct solution. Most numerical libraries includes algorithms that finds the extremum of a given function of one or more independent variables. What particular type of algorithm to choose depends strongly on the type and complexity of the model [107, 132]. If one uses e.g. a gradient search algorithm, and the error surface has a complicated structure, one can easily get trapped in a local minimum, i.e. one obtains a "false" or a "non-optimal" solution. The number of measurements required for an inversion, depends on the complexity of the model. If the model is linear, and it contains n variables, one needs at least $n+1$ measurements for noise free data. If the data are contaminated by noise, however, one needs more data, depending on the noise level of the measurements. If the model is non-linear, the number of measurements needed to invert the data can be much higher. As we have already seen in Section 2.4 and 2.5, the BRF models can be highly non-linear. The expectation is thus that a reliable inversion can only take place if $N \gg n$, where N is the number of available measurements and n is the number of model parameters. Examples of inversions of various BRF models can be found in [30, 40, 41, 56, 58, 81, 109, 112].

Since the measured BRF $\hat{\rho}$ must be regarded as a realization of a stochastic variable for each set of angles $(\theta_s, \theta_d, \phi)$ and each observation time t, the parameter estimates themselves are stochastic variables [68, 132]. If we furthermore include a continuous temporal dimension, it is obvious that the stochastic variable $\hat{\rho}$ comes from an underlying stochastic process. This background stochastic process is simply the full ensemble of time dependent BRF's for all possible times and angular positions.

The physical process of light scattering is itself a stochastic process by nature. In the most simplified approximation, there are two possible outcomes of an encounter of a photon with a particle. It can be scattered or it can be absorbed. We call the probability that the photon will be scattered for the single scattering albedo. If a scattering occurs, the direction of the scattered photon is determined by the roughness of the particle. The directional probability density function of the scattering is characterized by the phase function $p(g)$ where g is the phase angle[1].

In an optical measurement the detector collects the energy of the recieved photons. A measurement is also random process resulting from the random process of scattering, the random process of emittance of radiance from the illumination source, and random noise in the detector and photon counting system.

Figure 2.2 illustrates the stochastic nature of radiance measurements in the EGO system. The figure shows two time series of radiance measurements taken from the nadir position, over the same reference panel target at two different days. Each curve clearly represent a realization of a random process $x(t)$, where $t_s \leq t \leq t_e$, and t_s and t_e is the start and end time of the experiment, respectively. To fully characterize the BRF of a target, we would thus need an infinite

[1] $p(g) > 0$ and $\frac{1}{4\pi}\int_{4\pi} p(g)d\Omega = 1$ [47]

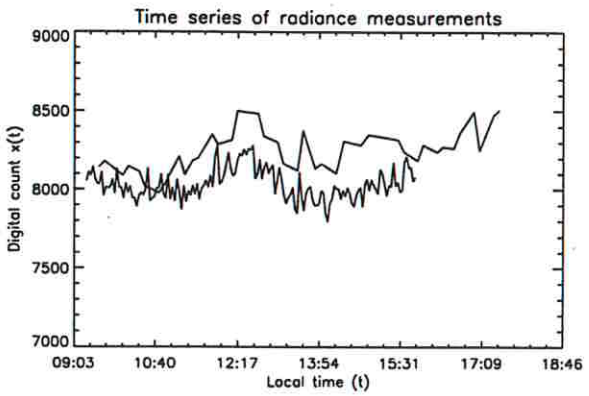

Figure 2.2: The time series of measurements from the nadir position over a reference panel. Measurements from Experiments 48 and 49 in Appendix B.

number of measurements from an infinity of measurement positions. From these measurements we could estimate the mean reflectance factor at each position, and these average reflectance factors would together form the BRF. However, during a real experiment, we can only make one measurement from each selected measurement position at a given time. These measurement make up a noisy and incomplete BRF estimate. Hence, we use a large number of noisy BRF estimates to invert models containing a few parameters. As discussed earlier, the outcome of the inversion process is strongly dependent on the quality of the input data. For a numerical inversion of certain BRF models, a different initialization of the inversion process will result in completely different parameter estimates. Since we clearly use random variables as input data to the inversion process, the output parameters will also be random variables.

2.6.1 Estimation accuracy and bootstrapping

The standard techniques for computing variance of parameters or for setting confidence intervals for the true parameters assume that the size of the available set of sample values is sufficiently large, so that "asymptotic" results can be applied [159]. However, in our optical measurement experiment, this assumption cannot be made. Because of time constraints we could only make one "full" measurement series of each target. Thus, the large sample method is inapplicable for our data. To overcome this problem we applied the so-called "bootstrap" method [26, 27, 159] to obtain estimates of mean values and variances. The bootstrap is a recent technique, where the observations are randomly reassigned and the estimators recomputed. These assignments and re-computations are done a large number of times, and thereby treated as repeated (synthetic) experiments. The bootstrap was introduced by Efron [26, 27] for estimation of bias, variance, confidence intervals and measurement errors.

The bootstrap is an extremely attractive tool in that it requires very little in the way of modeling assumptions or analysis. It is essentially a computer based method that substitutes theoretical analysis with a considerable amount of computations [159].

The bootstrap principle for estimating the statistical distribution of a parameter $\hat{\vartheta}$ [159] is as follows:

Step 1 Conduct an experiment to obtain a random sample $x = \{X_1, X_2, \ldots, X_n\}$.

Step 2 Construct an empirical distribution $\hat{F}$, which puts equal mass, $1/n$, at each observation, $X_1 = x_1, X_2 = x_2, \ldots, X_n = x_n$.

Step 3 From the selected $\hat{F}$, draw a sample $X^* = \{X_1^*, X_2^*, \ldots, X_n^*\}$ called the bootstrap (re)sample.

Step 4 Approximate the distribution of $\hat{\vartheta}$ by the distribution of $\hat{\vartheta}^*$ derived from X^*.

A model inversion can be viewed as a realization of a random process, where the resulting parameters characterize the inversion. We can therefore repeat the "inversion experiment" by inverting for different input data, and using different initializations. Based on the bootstrap principle we now define the following procedure for estimating BRF model parameters $\hat{\vartheta}_1, \ldots, \hat{\vartheta}_p$ of the models

Step 1 Estimate the reflectance factors (RF) from all the available measurements for a target.

Step 2 Draw randomly n values of the estimated RF, and use these for inversion of the model, resulting in a bootstrap set of parameter estimates $\hat{\vartheta}_1^*, \ldots, \hat{\vartheta}_p^*$.

Step 3 Replace the randomly drawn samples and repeat **step 2**.

Step 4 Repeat **Step 3** a number of B times.

Step 5 For the final estimate of the mean and the variance for each of the parameters $\hat{\vartheta}_1, \ldots, \hat{\vartheta}_p$ based on the B bootstrap estimates $\{\hat{\vartheta}_1^1, \ldots, \hat{\vartheta}_1^B\}, \{\ldots\}, \{\hat{\vartheta}_p^1, \ldots, \hat{\vartheta}_p^B\}$.

We believe that the bootstrap principle will find many uses in assessing the accuracy of measurements in future optical scattering experiments.

2.7 Statistical estimators

In this section we list the definitions of some frequently used statistical estimators necessary for the data analysis presented in Chapters 5, 6 and 7. We list the pertinent empirical estimators used to estimate the center value and the dispersion of the experimental data, in addition to empirical correlation measures. Detailed

discussions on the properties of the statistical empirical estimators can be found in standard textbooks e.g. [8, 27, 68, 88, 132]

The empirical average value of a dataset $\mathbf{Y} = \{y_1, y_2, \ldots, y_I\}$, consisting of I measurements for a specific wavelength and geometrical location is defined by

$$\overline{Y} = \frac{\sum_{i=1}^{I} y_i}{I} \tag{2.24}$$

The sample standard deviation of the dataset is given by

$$\hat{s}_Y = \sqrt{\frac{\sum_{i=1}^{I}(y_i - \overline{Y})^2}{I-1}} \tag{2.25}$$

and the sample variance is thus

$$(\hat{s}_Y)^2 \tag{2.26}$$

The empirical mid-range is defined by

$$Y_{mid} = \frac{y_{max} + y_{min}}{2} \tag{2.27}$$

where y_{max} and y_{min} are the maximum and minimum values of the dataset. The empirical half-range is likewise defined by

$$\hat{s}_{half} = \frac{y_{max} - y_{min}}{2} \tag{2.28}$$

The absolute range is defined as the difference between the maximum and minimum of the data set

$$\hat{s}_{abs} = y_{max} - y_{min} \tag{2.29}$$

The linear correlation coefficient between two different data sets $\mathbf{X}$ and $\mathbf{Y}$ is estimated by

$$\hat{r}_{XY} = \frac{\widehat{cov}}{s_X s_Y} \tag{2.30}$$

where

$$\widehat{cov} = \frac{\sum_{i=1}^{I}(x_i - \overline{X})(y_i - \overline{Y})}{I-1} \tag{2.31}$$

is the empirical covariance between data sets $\mathbf{X}$ and $\mathbf{Y}$. The root-mean square error *rms*, between two different, L-dimensional vectors $\mathbf{x}$ and $\mathbf{y}$, is further estimated by

$$rms = \sqrt{\frac{\sum_{l=1}^{L}(x_l - y_l)^2}{L}} \tag{2.32}$$

Sometimes it is convenient to express the dispersion as a *percentage*, or a normalized dispersion value

$$p = 100\frac{\hat{s}}{\overline{Y}} \tag{2.33}$$

where $\overline{Y}$ is the average value or the mid range, and $\hat{s}$ is correspondingly the standard deviation or the half range (absolute range).

The absolute difference can thus be written as

$$\hat{s}_{abs} = 200\frac{y_{max} - y_{min}}{y_{max} + y_{min}} \tag{2.34}$$

Under the assumption of normally distributed data, the probability that a sample y is contained in the interval

$$\overline{Y} - z_{\alpha/2}s < y < \overline{Y} + z_{\alpha/2}s \tag{2.35}$$

is α. For a probability of 0.95, $z_{\alpha/2} = 1.96$. An estimate of the 95% dispersion is then $100 \times 1.96s/\overline{Y}$.

When the number of samples I is large ($I > 30$), and the population standard deviation σ is unknown, a $100(1 - \alpha)$ confidence interval for the mean value is given by

$$(\overline{Y} - z_{\alpha/2}\frac{\hat{s}}{\sqrt{I}}, \overline{Y} + z_{\alpha/2}\frac{\hat{s}}{\sqrt{I}}) \tag{2.36}$$

For a 95% confidence level $z_{\alpha/2} = 1.96$, i.e. with a probability of 0.95, the true mean value of the parameter is within the confidence interval. The 95% confidence interval for the population mean is used extensively in the parameter estimation.

Chapter 3

Characterization of the Targets

In this chapter we summarize some important characteristics of spectral signatures and leaf optical properties of plants. Subsequently we describe the three selected targets, and the main reference panel used in this thesis.

3.1 Leaf optical properties

Numerous studies have shown that spectral signatures can be used to distinguish plant species [101, 108, 94]. Spectral signatures and vegetation indices have been used to extract information on chlorophyll content, photo-synthetic efficiency, biomass, pigments, water content, vitality etc. [4, 9, 11, 12, 13, 14, 35, 34, 101, 124], amongst others.

Chlorophyll and other plant pigments strongly absorb energy in wavelengths centered around 450 nm (blue) and 670 nm (red). A relative lack of absorption at the wavelengths between the two chlorophyll absorption bands allows a reflectance peak to occur at approximately 540 nm (green) [34, 51, 83, 153]. Plants under stress have a decreased chlorophyll production, and thereby a decreased absorption by the pigments. Stressed plants have a much higher reflectance, particularly in the red portion of the spectrum and therefore appear yellowish [14, 51, 53]. The pigmentation is the dominating factor of reflectance spectrum in the visible wavelengths. The internal structure of a plant leaf largely controls the reflectance in the NIR [34, 51, 83].

A decrease in leaf water content can increase the reflectance and transmittance from leaves at all wavelengths. This is due to an increase in internal air space or cell breakdown as the water content decreases, which may increase reflectance and decrease transmittance [153]. When water is lost from plants, cell sap and the internal fluids become more concentrated, resulting in reduced plant water potential, relative water content and cell turgor.

Leaves in general exhibit both diffuse and specular scattering characteristics. The diffuse component arise from the interaction of radiation within the interior

of the leaf. Radiation is scattered at each refractive index discontinuity, especially between air and cell walls, and randomly directed back through the leaf surface as diffuse radiation [153].

Vogelmann [148] has reviewed the topic of light micro environment within plant tissue, and how the light penetrating to various tissue layers relate to its perception and utilization. The attenuation of light inside plant leaves results from complex absorption and scattering processes controlled by the biochemical composition and the morphological features of the various tissues. The epidermis plays an important role in determining the overall BRF of the leaf, whereas the chlorophyll and other plant pigments controls the level of light absorption [44]. The epidermal cells of vascular plants focus light to levels levels substantially higher than incident light [22, 148, 149].

Non-Lambertian scattering properties of individual leaves have been measured, modelled and documented by [10, 150, 153] amongst others. Govaerts *et al.* [44] presents a study where they use a three-dimensional ray tracing light scattering model to describe the transfer of radiation inside a dicotyledon leaf as a function of its internal structure and morphologiocal properties.

3.2 Special features of lichens and bryophytes

Lichens and bryophytes have long been recognized as sensitive indicators of environmental conditions. Certain species have been recognized to indicate the presence of specific mineral deposits, soil and site conditions, presence and level of atmospheric and aquatic pollutants, ages of rock surfaces and historical cominity of forest cover, winter climate and snow depth etc. [5]. The indicator power follows from the characteristic that these organisms have very limited control of the uptake and loss of water. The metabolic process follow the rain fall and evaporation pattern more closely than for vascular plants [110]. The lack of a root system makes them unreliant of soil, and enables them to grow on rock, bark or hard surfaces. Since their hydration level follows their surroundings, this sometimes leads to hypersensitivity to microclimatic dryness or pollutants. Much research has been devoted to studying the effects of man-made environmental changes and lichen species distribution patterns [5, 46, 64, 79, 86]. Lichens tend to absorb, trap and concentrate chemicals and radionuclides. The chemicals and isotopes can be analyzed to determine pollution levels. Many lichens are sensitive to elevated SO_2 concentration, since high levels cause chlorophyll degradation, resulting in an breakdown of symbiosis between the fungal partner and its photobiont [36].

Attenuation of solar radiation within bryophytes and lichen canopies is much more intense than in vascular plant canopies. Longton [86] reports that light irradiance fell to 10% of the top-of-canopy irradiance at a depth of 4 cm in a *Cladina stellaris* stand. At the base of the canopy the irradiation level was less

than 5%. Photosynthetic active tissue is thus concentrated in the uppermost parts of the lichen colony.

3.3 *Cladina stellaris*

Cladina stellaris [1] is a fruticose lichen. *Cladina stellaris* is particularly pollution sensitive since it does not have a protective bark. Its natural habitat is tundra and open woodland (see Figure 3.2), and is typical of dry and sandy environments, where it forms 5 – 15 cm deep mats. It is more common in inland habitats than in marine habitats. The thallus is richly branched into spherical clusters, and the "leaf" orientation distribution is therefore spherical. Figure 3.1 shows a picture and a sketch of the cross-section of a *Cladina stellaris* thallus. The *Cladina stellaris* has a layered structure where the algae are concentrated in the outer layer. The algae and medulla (loosely organized hyfens) are not protected by an outer cortex, but are exposed as a whitish loosely woven fiber layer. The hollow core is surrounded by a layer of strengthening tissue.

Studies have shown that the growth is concentrated to the uppermost 6 mm of the podetia [86]. After 10 – 15 years of accumulation the base starts to degenerate, at approximately the same rate as the upper parts extend. After 15 – 20 years the degeneration rate exceeds the generation rate, and the podetia dies. The chlorophyll, and thus the photosynthetic activity is concentrated in the younger parts of the podetia [86]. The annual growth rate is estimated to be approximately 5 mm [2]. Drying usually occurs from the surface and downwards. The drying of a deep *Cladina stellaris* stand saturated by water has been studied in field [86]. During a single day, the relative humidity stayed close to 100% at the bottom layer, whereas at the top it fell to 30 – 50%. At the same time the temperature difference between the top and the bottom layer was 17°C. This indicates that the *Cladina stellaris* helps keeping the moisture in the light-texture woodland soils. The *Cladina stellaris* often grow in areas of deep long lasting snow. Under these conditions the *Cladina stellaris* receives no light for several months. Detailed discussions on photosynthetic activity, respiration rates, and other biophysical characteristics of *Cladina stellaris*, can be found in [2, 69, 86, 133].

3.4 *Flavocetraria nivalis*

Flavocetraria nivalis [2] has erect foliose thallus that are 5 – 8 cm high and approximately 120 μm thick. Figure 3.3 shows a photograph of the *Flavocetraria*

[1] The *Cladina stellaris* was formerly referred to as being of the genus *Cladonia*, and is therefore found under the names *Cladonia stellaris* and sometimes *Cladonia alpestris*.

[2] The *Flavocetraria nivalis* was re-classifed to the genus *Flavocetraria* from the genus *Cetraria* in 1994 [65, 66].

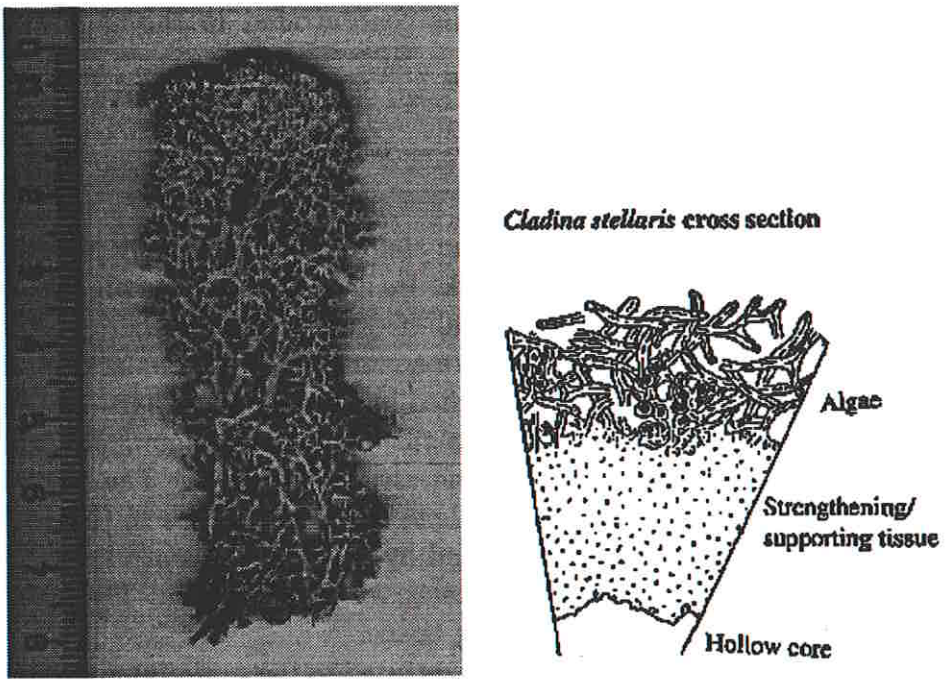

Figure 3.1: A *Cladina stellaris* element, and the cross section of the thallus.

nivalis thallus, and a scetch of the cross section of the thallus. The strongly wrinkled lobes are up to 7 mm broad, rather flat, with a glossy yellow upper surface, and a pale yellow lower surface. The basial portion of the thallus (lowest 5 – 10 mm) has a dark yellow colour. The upper and lower cortex are ca. 20 μm and 15μm thick respectively. The upper and lower cortex are composed of 2 – 3 and 2 layers, respectively, of pachydermatous cells of size up to 5μm. The largest cells are closed to the algae layer. The mudullary hyphae are 3 – 8μm. A more detailed description of the anatomy of *Flavocetraria nivalis*, can be found in Kärnefelt *et al.* [65, 66].

The *Flavocetraria nivalis* is widely distributed in arctic-boreal areas, mainly in the northern hemisphere [66]. It is found in arctic-alpine, boreal, exposed and moderately exposed environments.

3.5 *Racomitrium lanuginosum*

The *Racomitrium lanuginosum* moss forms 5 – 12 cm deep compact mats on acid rocks, blanket bogs or peatland mires. The compact mats has a spatial density of 4.5 shoots cm^{-2} [86]. Each leaf has a colorless tip, which is transparent when wet, and white when dry. This gives the moss a greyish look when it is dry, while in a moist state the moss appears more greenish. It is found in boreal environments, from marine to alpine areas. *Racomitrium lanuginosum* mats are often found in

Figure 3.2: A forest landscape in Pechenga, Russia, where lichens covers the floor.

dry and windy environments, where the snow is blown away in the winter. This gives a severe winter environment, but a long growing season. Figure 3.4 shows a picture of *Racomitrium lanuginosum* shoots. The "fluffy" shoots in the left half of the picture are of moisten *Racomitrium lanuginosum*, wheras the shoots on the right side are dry.

The *Racomitrium lanuginosum* is an ectohydric moss. It takes up water freely over the whole surface of the plant. The *Racomitrium lanuginosum* has little development of internal conduction tissue, but has a well developed external capillary conducting structures [110]. Figure 3.4 shows magnified images of the surface and cross section of a *Racomitrium lanuginosum* leaf. Water is conducted from one part of the shoot system to another by the papillose hair points. Bryophytes generally lack inter cellular space, but they often have proportionally thick cell walls. Nearly 60% of the total cross section of *Racomitrium lanuginosum* leaf is occupied by cell walls [110].

The leaf area index (LAI) of moss patches is high compared to flowering plants. Proctor [110] has estimated the LAI of several moss species to vary from 6 to 25. For his estimates of water-potential gradients in ectohydric mosses, he argues that he can safely assume a LAI value of 10.

3.6 GORE–TEX^{TM} reference panel

GORE–TEX^{TM} is the trade mark of W. L. Gore & Associates, Inc. They manufacture a variety of expanded polytetrafluoroethylene (PTFE) fluid sealing products for industrial applications. GORE–TEX^{TM} is a PTFE material, which is the material used in the commercially available Spectralon reference panels [128].

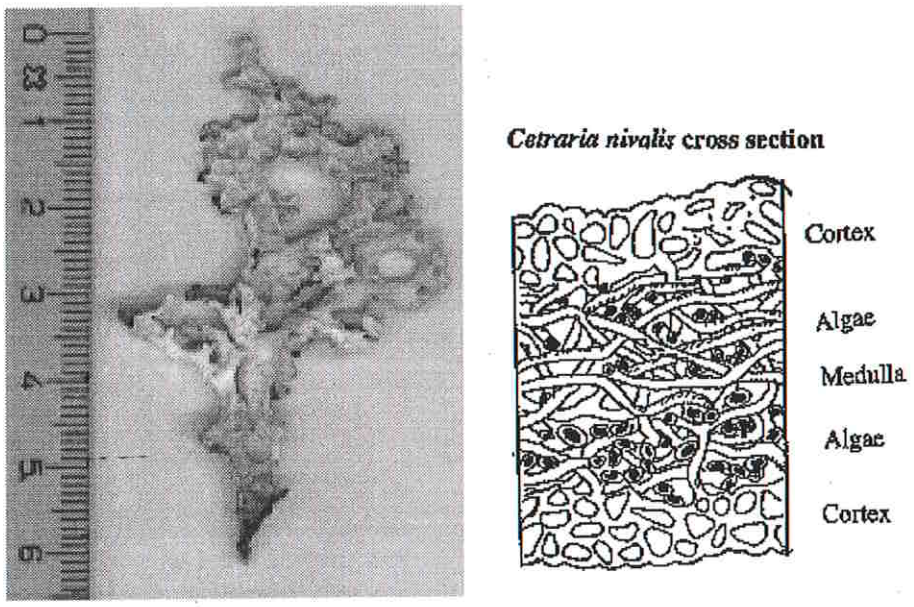

Figure 3.3: A *Flavocetraria nivalis* thallus and its cross section.

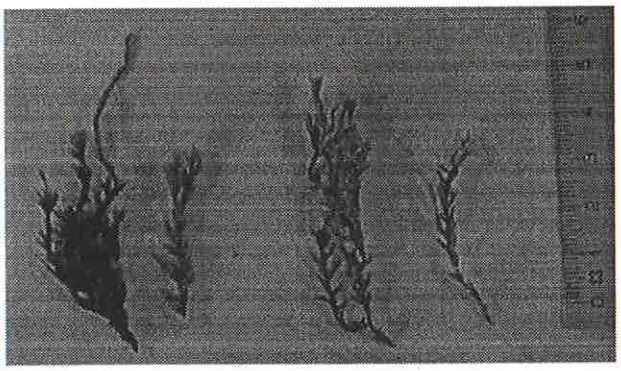

Figure 3.4: *Racomitrium lanuginosum* shoots.

The main reference panel we used in this study, was manufactured at the Italian W. L. Gore & Associates, Inc. manufacturing site. PTFE has several physical and optical properties which makes it ideal for a standard of diffuse reflectance. The reflection properties of pressed PTFE powder has been thoroughly documented by the National Bureau of standards, Washington D.C. [157]. They showed that pressed PTFE powder reflects 99% or higher for visible and near infrared wavelengths. Compared to pressed Barium Sulfate powder, the PTFE became more specular at high ($\leq 70°$) angle of incidence. However, the physical properties makes PTFE more attractive: it is non-sticky, water repellant and it does not degrade with age (the exception is that exposure of high-intensity UV radiation will degrade the reflectance properties in the UV regions of the spectrum), and it is not affected by any common chemicals. However, the re-

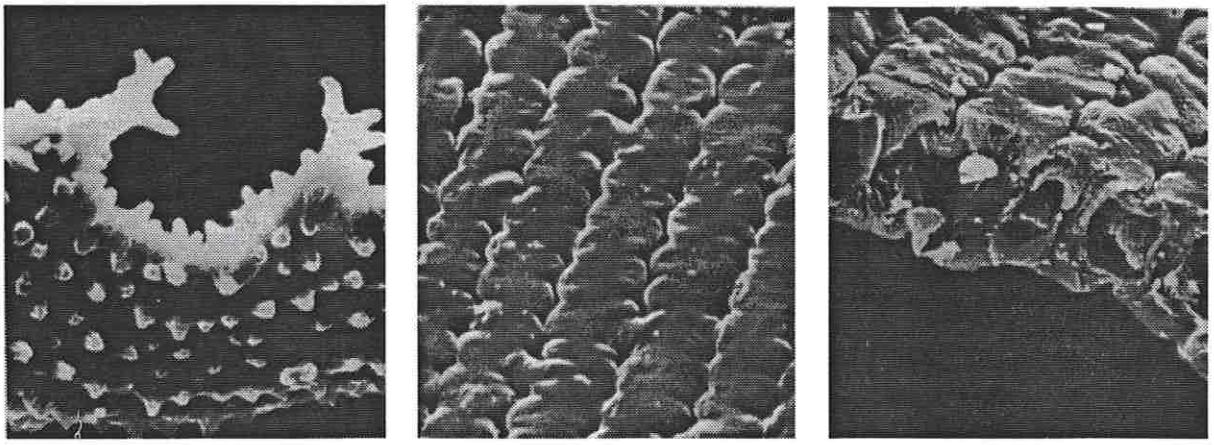

Figure 3.5: Air dried *Racomitrium lanuginosum*, Left: part of leaf (× 830), Central: upper surface of leaf (× 1670), Right: Cross section of leaf (× 1670). Adapted from Proctor [110].

flectance properties of the surface depends on the surface roughness as well. The GORE–TEX^{TM} reference panel available at the EGO, was not manufactured from pressed PTFE powder, but from the special patented stretching technique of W. L. Gore & Associates, Inc. GORE–TEX^{TM} is produced by stretching PTFE to form a strong and porous materials. The original surface appeared to be very smooth, and therefore had a strong specular reflectance component. The surface of the GORE–TEX^{TM} reference panel was therefore manually roughened before use.

Chapter 4

Experiment and BRF Estimation

In this chapter we describe the experimental setup and the data acquisition procedure we applied in the EGO laboratory. We also explain how we estimated the bidirectional reflectance factors for the experimental data. Details on each experiment can be found in Appendix B.

4.1 The experimental setup in the EGO

Figure 4.1 shows a schematic overview of the EGO and its coordinate system. The detector and the source are mounted on two independent steerable rails. The source can be positioned in zenith (θ_s) from 0° to 80°, where $\theta_s = 0°$ corresponds to the top vertical position (zenith). The source can be rotated in azimuth. However, in the experiments described in this thesis, the source was kept at a constant azimuth position. The detector can be positioned at zenith angles in a range from $\theta_d = -80°$ to $\theta_d = 80°$. The vertical center position $\theta_d = 0°$ corresponds to the nadir position of the EGO. The detector can be positioned in azimuth from $\phi = 0°$ to $\phi = 360°$, relative to the source. In the principal plane, ($\phi = 0°$), θ_d is negative for the forward scattering direction, and positive in the backscatter direction, and vice versa for $\phi = 180°$.

We selected a 1000 W Tungsten Halogen collimated lamp as the source for the experiments. We used the lamp at its maximum beam aperture opening (39°). When the source was positioned at $\theta_s = 30°$, the beam was centered at the center of the target platform. The center of the source was not changed during the measurement campaign. We always switched on the lamp at least 30 minutes prior to the first measurement of an experiment, to allow the lamp to reach a stable temperature before the measurements took place. Further details on the temperature inside and outside of the lamp spot can be found in Section 5.1.

We used a Spectron Engineering SE590 data logger with the CE390WB-R-G10 wideband, high-sensitivity detector. We used the spectro-radiometer with a $1°, 6°$ and 15° degrees field of view (FOV). The 6° FOV corresponds to using

the detector with no front optics. Spectron Engineering reports (*Spectron Engineering Inc., personal communication, 1996*) that the light acceptance angle has been verified in the horizontal and vertical plane. When the boundaries of the FOV is defined as the light acceptance angle, at which the peak value of a point source decreased to 50% of its maximum value (Full-Width-at-Half-Maximum (FWHM)), the detector head has a 6° FOV in the horizontal plane and a 5° FOV in the vertical plane. To determine the maximum light acceptance angle of the detector (positioned at $\theta_d = 0°$ and $\phi_d = 0°$) we carefully moved a sheet of black cardboard into the FOV of the detector in the vertical and the horizontal directions. We found that the maximum acceptance area in the principal plane (vertical) was 18 cm, and in the cross plane (horizontal) 28 cm. Thus, the maximum acceptance angle is approximately 8° in the vertical plane and 12° in the horizontal plane. The SE590 was mounted on a 55 cm long extension arm. The distance from the detector to the target was thus 130 cm.

The SE590 contains a 256 elements photodiode array which records a discrete spectrum from 368.4 to 1113.7 nm. The signal is conducted to a microprocessor based controller via a cable. The controller processes the signal by amplifying and digitizing it with 12 bit resolution. For each spectral scan, the controller actuates the shutter to measure and store the dark current. The controller calculates the optimum integration time, acquires the spectrum and then automatically subtracts the noise for all 256 spectral elements. For more details see the SE590 operating manual [123]. The raw data from the SE590 is given in Digital Counts [DC]. A spectro-radiometric calibration was made for the SE590 by the EGO staff, 18 months after our experiment. A presentation of this calibration is shown in Figure 4.2. Since the calibration was made such a long time after our experiment, it is not used.

During our experiments a relative humidity and temperature logger (AGENT HT1-A:, Module No: 53206) was active. We used the logger to make a recording every 10 minutes. The logger was placed on top of the *Flavocetraria nivalis* and *Racomitrium lanuginosum* targets, close to an edge, but outside the field of view of the detector. For the *Cladina stellaris* target, we placed the logger 5 cm beneath the target surface.

4.2 Data acquisition

We used the following algorithm for collecting the experimental data presented in this thesis:

Step 1) Position the detector at the first $(\theta_s, \theta_d, \phi)$ position

Step 2) Acquire data for all the θ_d positions ($\theta_d \in \{-70°, -65°, ..., 65°, 70°\}$) or ($\theta_d \in \{70°, 65°, ..., -65°, -70°\}$), in the current ϕ plane.

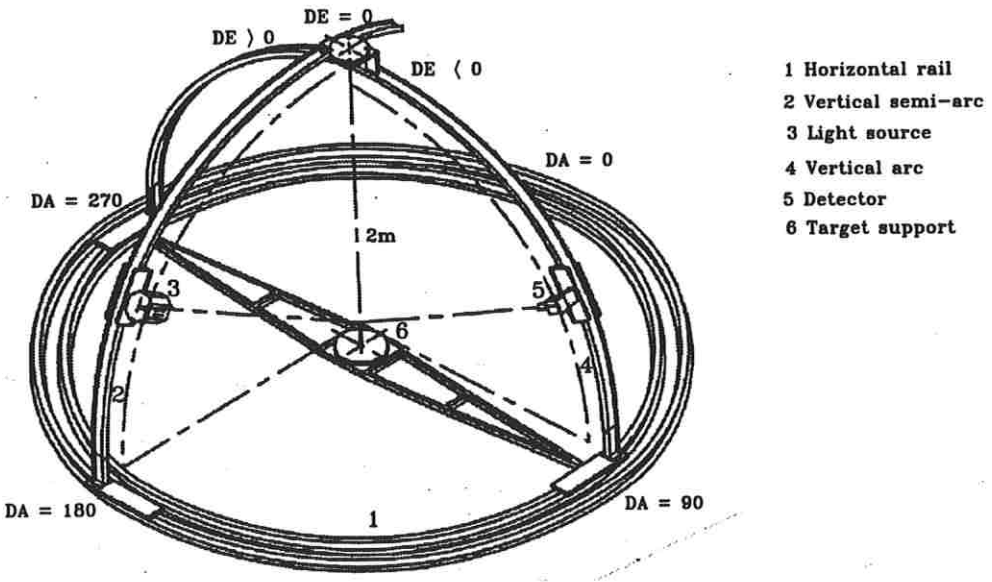

Figure 4.1: Overview of the EGO system with the EGO coordinate system. DE - detector zenith (θ_d), DA - detector azimuth (ϕ_d).

Step 3) If the current ϕ position is not the final ϕ, move the detector to the next ϕ position and goto *Step 2)*

Step 4) If the current ϕ position is the final ϕ, move the detector to the initial $(\theta_s, \theta_d, \phi)$ position, and repeat the initial measurement.

For each measurement acquired, the system time and the EGO position was logged in a separate file. The data acquisition was usually carried out in automatic mode, which means that the commands for the detector motion and data acquisition were pre-programmed. Figure 4.3 shows the sampling positions for the three source zenith angles. A minimum angular separation of 10° in azimuth and zenith between the SE590 detector and the 1000 W source is necessary in order to avoid a collision between the detector and the source. Unfortunately, the positioning constraints of the EGO restrict measurements in the back-scattering region of the target.

4.3 Target preparation

In this section we describe the target preparation procedures for the EGO experiment. Biophysical descriptions of the *Cladina stellaris*, *Flavocetraria nivalis*, and *Racomitrium lanuginosum* targets were given in Sections 3.3, 3.4 and 3.5, respectively.

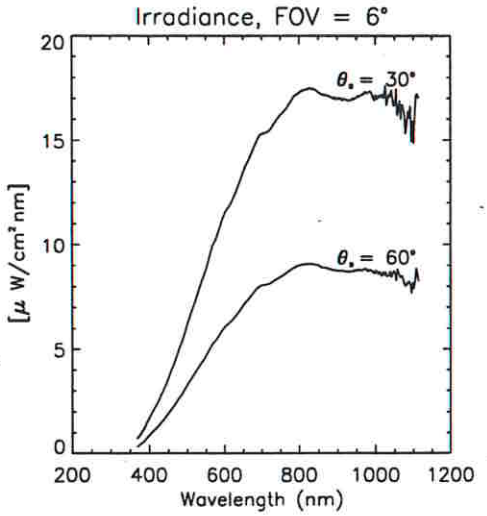

Figure 4.2: The spectral energy distribution of the 1000W lamp, measured over the GORE–TEX^{TM} reference panel, by means of the SE590.

Target: *Flavocetraria nivalis*

The *Flavocetraria nivalis* canopy was approximately 6 cm deep. Height variations within the mat were less than 2 cm. We collected the *Flavocetraria nivalis* lichens in Balsfjord, Norway. The collection site was approximately 260m above sea level. We rinsed the *Flavocetraria nivalis* target to remove all other lichen species, mosses, soils, and dry leaves. The *Flavocetraria nivalis* was then assembled in an EGO target box at its natural density. Figure 4.4 shows the *Flavocetraria nivalis* photographed in its natural environment.

Target: *Cladina stellaris*

The *Cladina stellaris* target had a depth of 12 – 15 cm. We bought the *Cladina stellaris* from Norske Moseprodukter [93], who had collected the lichen from the floor of a pine forest in Østerdalen, Norway. The dry weight of the *Cladina stellaris* was approximately 3.5 kg. We soaked the *Cladina stellaris* target in water, and rinsed it for dry leaves and pine needles before we assembled it in an EGO target box. Figure 3.2 shows a pine forest landscape similar to where the *Cladina stellaris* was collected.

Target: *Racomitrium lanuginosum*

The *Racomitrium lanuginosum* sample mat was approximately 12 cm deep, with local height variations of approximately 5 mm. We collected the sample patch on a blanket bog (sub-arctic peatbog), on Marisletta at Kvaløya near Tromsø, Norway. When the *Racomitrium lanuginosum* was placed in the EGO target

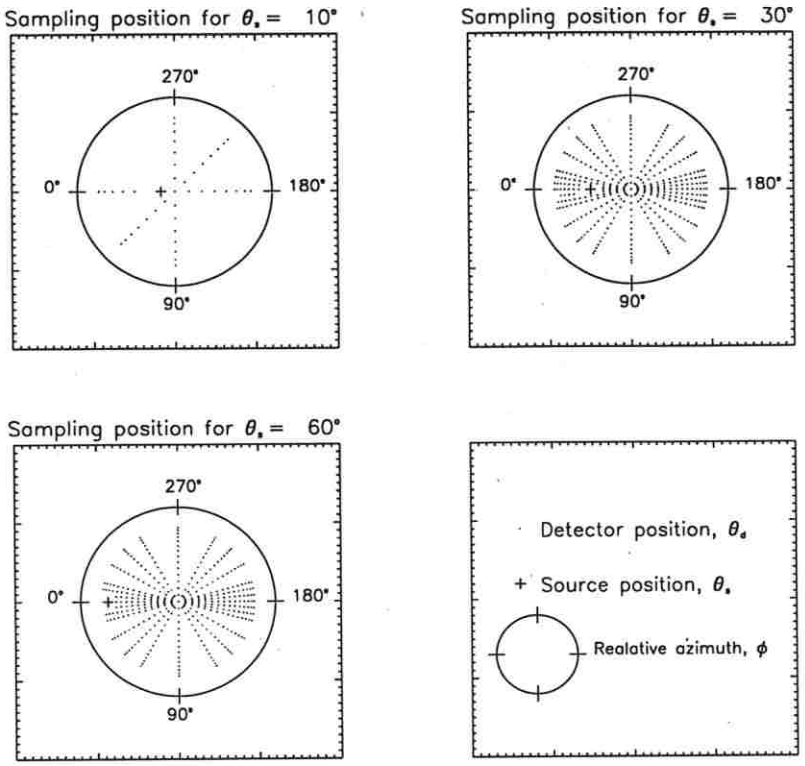

Figure 4.3: The sampling positions for the main data sets.

box, it was not flat, but formed a micro landscape of valleys and mountains. The maximum height difference of this landscape was approximately 5 cm. We kept the moss in a phytochamber when it was not in use. The setting of the chamber was 16°C, 24 hours of light, with relative humidity of 80%. Figure 4.5 shows the moss in the target box. The central part of the target was moistened, which gave the moss a green color. The edges were dry, and therefore appeared greyish.

The GORE–TEX^{TM} reference panel

We used a GORE–TEX^{TM} (1×1) m^2 white reference panel that was manufactured especially for the EGO facility by Gore Sealant Technologies. We chose to use the GORE–TEX^{TM} reference panel because this was the largest reference panel available at the EGO facility, and because it was large enough to cover the 6° Field of view (FOV). More details on the GORE–TEX^{TM}panel can be found in Sections 3.6 and 5.5.

Figure 4.4: A patch of *Flavocetraria nivalis* photographed at the target collection site in Balsfjord, Norway.

The EGO target boxes

The (1×1) m^2 EGO target boxes were spray-painted black inside and outside. The floor of the boxes were built up with polysterene so that the upper layer of the canopies were aligned with the top edge of the box wall. The box floor was covered with black cardboard.

4.4 The experiments

We performed a total of 62 experiments. We have provided a description of the system configuration, target temperature and humidity state, measurement positions and auxiliary data for each experiment in Appendix B.

Experiments 1 to 18 are the "initial measurement" series. The purpose of these measurements were to get a first impression of the reflection properties of the targets, the instrumentation, and the data flow. We therefore made several short measurement series of the lichen and reference panel targets, experimenting with different fields of view, source elevation angles, rotation and shifting of the targets and so on. The series contained 100–150 measurements and lasted from 1 to 1.5 hours. Most of the data in these series were made for $\theta_s = 55°$, $\theta_d = \{-60°, -55°, \cdots, 55°, 60°\}$ and $\phi = \{0°, 45°, 90°, 135°\}$. During the initial experiments, the lichen targets went from a "wet" to "dry-on-top" to a "dry" hydration state. Simultaneously with the initial measurements, we developed visualization and analysis programs that enabled us to make decisions regarding the sampling density etc.

When the targets were dry, and we had gained a high degree of confidence in

Figure 4.5: The *Racomitrium lanuginosum* in an EGO target box, placed in the EGO laboratory.

the system set up, we started the "long series". Experiments 19 to 31 contain 390 – 412 measurements each. The acquisition time for each of these experiments was approximately 3 hours. The targets were sampled at a 5° resolution in detector zenith angles $\theta_d \in \{-70°, 70°\}$, for 14 azimuth positions. Each target was measured for source zenith angles $\theta_s = \{30°, 60°\}$. The reference panel was measured with a detector elevation resolution of 10°. We later simulated the "missing" measurements for a 5° detector elevation resolution by linear interpolation. We used the data from these experiments to construct the BRF's of the target described in detail in Chapter 7.

Experiment 32 to 46 are "supplementary measurements", where we made shorter measurement series (100 – 150 measurements) of the targets in dry and wet states. The spectral signatures from these experiments are presented in Section 6.2. We repeated some of the experiments with the target rotated. We made measurements for additional source zenith angles $\theta_s = \{50°, 40°, 20°\}$, for $\phi = \{0°, 45°, 90°\}$. Last, we made a measurement the *Flavocetraria nivalis* on a white card-board back ground.

Experiments 47 to 54 are of the GORE–TEX^{TM} reference panel. We performed these experiments in order to estimate the measurement precision and system noise. The result of that analysis is presented in Chapter 5. Finally, Experiment 55 to 62 are of the GORE–TEX^{TM} and Spectralon reference panels, and were used to estimate the BRF of the GORE–TEX^{TM} reference panel presented in Section 5.5.

4.5 Experimental BRF estimation

In a laboratory environment the BRF of a target surface is estimated based on measurements of the response $y_t^\lambda(\theta_s, \theta_d, \phi)$ of the detector viewing the target, and measurements of the detector response $y_r^\lambda(\theta_s, \theta_d, \phi)$ viewing a reference panel, for a wavelength λ. An approximate BRF of the target can then be estimated as [19, 47, 113, 150]

$$\hat{\rho}_t^\lambda(\theta_s, \theta_d, \phi) = \frac{y_t^\lambda(\theta_s, \theta_d, \phi)}{y_r^\lambda(\theta_s, \theta_d, \phi)} \hat{\rho}_r^\lambda(\theta_s, \theta_d, \phi) \tag{4.1}$$

where $\hat{\rho}_r^\lambda(\theta_s, \theta_d, \phi)$ is an estimate of the BRF of the reference surface. The BRF of the reference surface, $\hat{\rho}_r^\lambda(\theta_s, \theta_d, \phi)$, is required to correct for non-ideal properties of the reference panel.

The calibration of the reference reflectance panel consists of determining its BRF distribution in terms of a "standard surface". The standard surface should be traceable to a National Institute of Standards and Technology (NIST) Standard reference material [152] or a material whose non-Lambertian properties are well documented [57].

To our knowledge, there are no publications describing laboratory tests of the optical properties or BRF distribution of GORE–TEX^{TM}, manufactured as the reference panel we applied. Figure 4.6 shows our measurements of the energy profile for reflected radiation with respect to wavelength, from the GORE–TEX^{TM} and the white Spectralon reference panels, for the nadir position for source zenith $\theta_s = 30°$, when illuminateding with a 1000 W lamp. We see that the GORE–TEX^{TM} reference panel has a slightly higher reflectance than the Spectralon reference panel for most wavelengths. In Section 5.5 we present an experimental estimate of the BRF of the GORE–TEX^{TM}reference panel, relative to the white Spectralon panel.

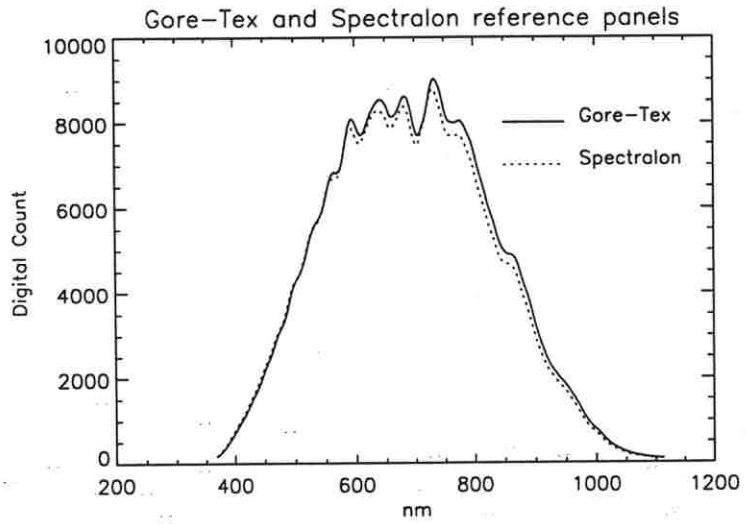

Figure 4.6: Energy profile of 1000 W halogene light scattered from theGORE–TEX^{TM} and Spectralon reference panels. The data are from Experiments 57 and 58

Chapter 5

Error Sources and Measurement Precision

The bidirectional reflectance factor (BRF) is defined [99] as the ratio of the radiant flux from the target surface to that of a perfectly diffuse surface under the same conditions of illumination and measurements (see section 2.3 for details). A BRF experiment is therefore based on the following two assumptions (1) The illumination and measurement conditions are the same for the target and reference measurements. (2) The reference panel is a perfectly diffuse surface. Violations of these assumptions lead to errors in the estimates of the bidirectional reflectance factors. In this chapter we present experimental results identifying some of the error sources in the EGO, and quantify the precision[1] of the BRF estimates.

The initial analysis of the lichen BRF data showed several effects that *could* be system dependent (detector, source or physical construction). A new series of experiments was therefore performed to examine these effects in greater detail.

In general, the first and the last measurement of each experiment were taken with identical detector position as explained in Section 4.2. The absolute difference in measured light intensities between the first and the last measurement of each experiment was found to vary between 0.5% and 3.0% (see Appendix B for details). Since the difference was observed for both targets and reference panels, we suspected that this effect was not only due to physical changes in the targets, but had to be related to time variations in source or detector.

The second effect we noticed was that the intensities measured in the left side of the goniometric hemisphere could be up to 5% higher (s_{abs}) than for corresponding positions in the right hemisphere. A similar effect was previously pointed out by Govaerts [43]. Govaerts used a laser source and a silicon photodiode detector, in his experiment.

The third effect we noticed was that the absolute intensity difference between

[1]Precision: The extent to which a given set of measurements of the same sample agree with their mean [156] i.e., how repetitive a measurement is.

measurements made for positions $(\phi, |\theta_d|) = (175°, \leq 60°)$ and $(185, \leq 60°)$ could be up to 14%, for target[2] and reference panel data. This resulted in a "step" in the BRF when the data were plotted. We therefore investigated further the following possible error sources of the EGO facility:

- Temperature variations in the laboratory and in the light spot.
- The stability of the irradiance from the lamp.
- The homogeneity of the lamp spot

We further examined the following system characteristics:

- The diffuseness of the GORE–TEX^{TM} reference panel.
- The alignment and leveling of the EGO arcs.

Other possible error sources, that we have not investigated further are:

- Changes in the instrument response due to thermal noise.
- Light pollution and optical noise from people present in the laboratory, computer screens and work-lights.
- Changes in the organic targets due to stress, evaporation and pigmentation changes.
- Quantization errors.

If not otherwise is stated, the SE590 data referred to in this chapter are for the wavelength $\lambda = 670.2$ nm. We used this particular wavelength, because it is close to one of the MISR spectral bands centered at 670 nm, used in Chapter 7 of this thesis. The SE590 was used with a 6° FOV over the GORE–TEX^{TM} reference panel, with a source zenith angle $\theta_s = 30°$.

5.1 Temperature variations on the target surface and in the laboratory

The temperatures on the target surface, inside and outside the lamp spot were collected during a six hour long experiment (auxiliary data for Experiment 48 in Appendix B). This was done in order to monitor fluctuations in target surface and ambient room temperature during the experiment. The assumption was that

[2]The *Racomitrium lanuginosum* target was excluded from this analysis. Because of local height variations in the target, the reflectance did not show a symmetrical pattern. For the *Racomitrium lanuginosum*, the above mentioned BRF "step" could be up to 35%.

possible significant changes in temperature might cause changes in the target that again could be linked to some of the variation found in the radiant intensity data.

A BARNES Instatherm detector (labelled "Insta" in Table 5.1) was used to measure the temperature in the light spot every 30 minutes. The Instatherm is a hand-held instrument that measures the temperature of a surface without contact. It operates by detecting and measuring the infrared energy emitted from the object it is aimed at. The Instatherm has a field of view of 2.8°, and it can measure temperatures in the range from $-10°C$ to $+60°C$.

The temperature on the panel outside the light spot was recorded with the "Ambient temperature" ("At" in Table 5.1) generic digital hygro/thermometer (AGENT HT1-A:, Module No: 53206).

Figure 5.1 shows the temperature recordings as a function of time. Table 5.1 summarizes the experiment statistics. We clearly see that after a transient phase, the temperature in the target stabilizes at a saturated level. The time duration of the transient was typically 1 hour. After thermal equilibrium was achieved, the maximum temperature variations observed was less than $1°C$. We thus consider temperature variations as a minor error source, and it was not investigated any further.

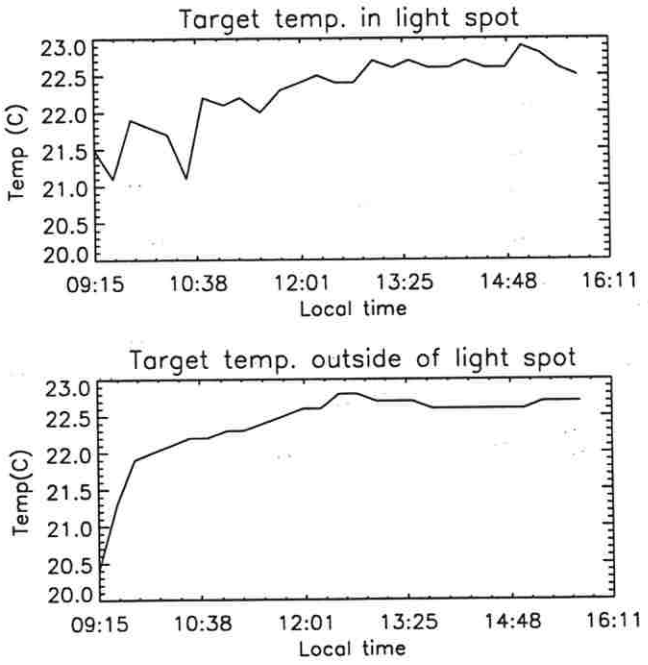

Figure 5.1: Temperature data from Experiment 48. The top panel shows the surface temperature of the target in the light spot (Insta) as a function of local time. The lower panel shows the temperature on the surface of the target outside the light spot (At).

Table 5.1: Summary of nadir intensity measurements. The measurements marked with an asterisk, are from Experiment 50, and were acquired with a stabilized power source. The other measurements are from Experiment 48

Instrument	$\overline{Y}$	$\hat{s}_Y$	Y_{mid}	s_{half}	I	95% dispersion
Insta	22.28 [°C]	0.49	22.0	0.9	27	6.14%
At	22.38 [°C]	0.52	21.6	1.2	27	6.31%
SE590	7890 [DC]	97	8039	242	150	2.37%
Lux	6614 [Lux]	80	6660	180	27	0.27%
SE590*	8102	78.7	8144	150	170	1.9%
SE590/G1*	570	5.7	572	10.5	113	2.0%

5.2 The stability of the illumination source

In order to examine the stability of the light radiation from the illumination source, a set of experiments were conducted. We first examined the variations in the radiation from the source measured from the nadir position. We next examined the intensity variations across the lamp spot by repeated measurements from different detector zenith position in the cross plane. We also tested the effect of stabilizing the power to the source. To further investigate the effect of the power variation on the source radiation, we performed several experiments using other sources and detectors than the 1000W lamp and the SE590 detector.

5.2.1 The irradiation variations measured from the nadir position

We carried out an experiment consisting of six hours of spectral measurements, keeping the SE590 detector stationary at the nadir position (Experiment 48). A measurement was acquired every 2.5 minutes.

A GOSSEN lux-meter (called "Lux" in Table 5.1 and 5.3 and Figure 5.2) was positioned at the brightest edge of the spot outside the field of view of the instrument. The GOSSEN lux-meter is a digital-readout instrument that provides measurements of illumination in Lux $[lm/m^2]$(e.g. [125]). According to the GOSSEN lux-meter users manual, the accuracy of the lux-meter is $\pm 3\%$ relative to the measured value. The lux-meter has a pen-recorder output of 0 to 1.0 Volt [V] for a selected Lux measurement range. The range selected for the 1000 W lamp was from 10 to 20 000 Lux.

The first Lux reading was taken a few minutes after the lamp was switched on. The average value, the standard deviation, and the dispersion for each of the instruments (Lux and SE590), are summarized in Table 5.1.

Figure 5.2 shows a plot of normalized SE590 and Lux data. Both data sets

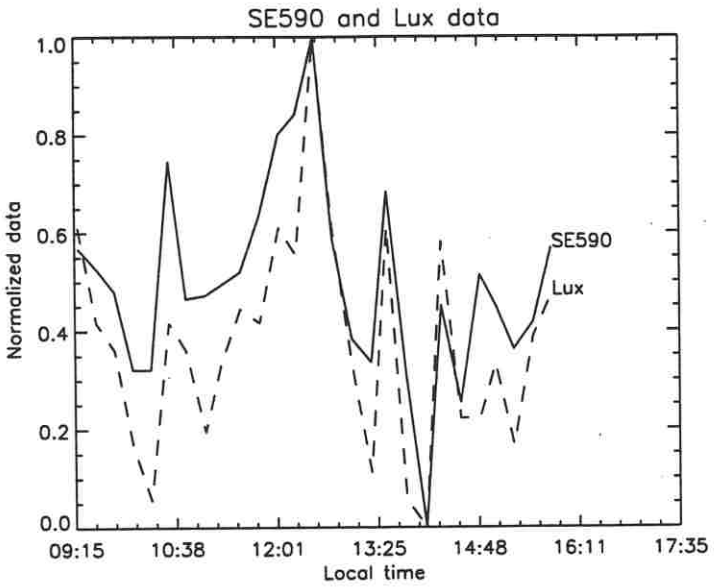

Figure 5.2: Normalized re-sampled SE590 and Lux data from Experiment 48.

were normalized according to

$$\|y_i\| = \frac{y_i - \min(Y)}{\max(Y) - \min(Y)} \tag{5.1}$$

where y_i is measurement number i of data set Y, and $\max(Y)$ and $\min(Y)$ are the maximum and minimum values of data set Y.

The SE590 data were re-sampled in time, to be in phase with the Lux readings. The Lux readings were always taken between 30 and 60 seconds after a SE590 measurement. Since an experimentalist had to be present in the vicinity to the Lux meter, this might have induced additional optical noise on the Lux readings. The linear correlation coefficient (Eq. (2.30)) between the Lux and SE590 was estimated to be $\hat{r}_{XY} = 0.85$. The high value of the correlation coefficient shows that there was a clear co-variation between the SE590 and the Lux readings. This is an indication that the variations in the intensity measurements were due to variations in the illumination source, rather than in the SE590 spectrometer.

5.2.2 Variations in the irradiation after stabilization of the power to the lamp

The experiment where the irradiation was monitored from the nadir position was later repeated (Experiment 50), but this time we connected a voltage stabilizer to the lamp. A second detector (SE590/G1) was used to get independent measurements of spectral intensity data, in order to determine the source of the fluctuations. The detectors were attached together and positioned as close as

possible to the nadir position. Measurements were acquired simultaneously every 2.5 minutes with both instruments. The original SE590 recorded data for 7 hours and 15 minutes, while the SE590/G1 was stopped 40 minutes ahead. The correlation coefficient between the two SE590 instruments was estimated to be $\hat{r}_{XY} = 0.95$. Table 5.1 summarizes the central and dispersion estimates for the two instruments.

Figure 5.3 (upper panel) shows a plot of the data measured with and without power stabilization of the lamp. As can be seen from the figure, the variation in the irradiance consists of a high frequency component, and a slowly varying "drift". The low frequency drifts on the two different days do not resemble each other. An estimate of the high frequency variation of the two data sets can be made by applying a simple high pass filter to the data

$$y^{HP}(t_i) = y(t_i) - y(t_{i-1}) \tag{5.2}$$

where $y(t_i)$ and $y(t_{i-1})$ are the measurements at time t_i and t_{i-1} respectively. Figure 5.3 (lower panel) shows the resulting high frequency variations for the two measurements series. The 95% dispersion interval for the high frequency variations of Experiment 48 data was 2.1%, whereas for the Experiment 50 it was 0.7%. The dispersion interval for the Experiments 48 and 50 were 2.4% and 1.9%, respectively. It is thus obvious that the power stabilization of the source only affected the high frequency variations, whereas the low frequency variations are unaffected.

Figure 5.4 shows the 95% dispersion interval for the nadir position measurements as a function of wavelength. In particular we have marked the readout for the four MISR wavelengths used later in this thesis. We see that the dispersion is approximately (5.1%,3.9%, 3.2%,2.9%) for $\lambda = (441, 553, 670, 861)$ nm, respectively. The same analysis was performed for the other positions, and showed the same tendency as for the nadir position. The 95% dispersion interval was consistently widest for the shorter wavelengths.

5.2.3 The illumination drift as a function of detector zenith angle.

We performed an experiment designed to examine the stability of the irradiance at different detector zenith angles (Experiment 49). This was done in order to investigate whether the detector zenith positions had an effect on the observed irradiation.

The measurements were made in the cross plane, $\phi_d = 90°$, for $\theta_d = (-50°, \cdots, +50°, \cdots, -50°)$ taken at 5° intervals. Each sequence took 6 minutes to complete. The sequence was repeated every 16 minutes. Figure 5.5 shows a plot of the average value of the digital counts from each of the θ_d position, as well as the maximum, minimum and standard deviation of the measurements from each

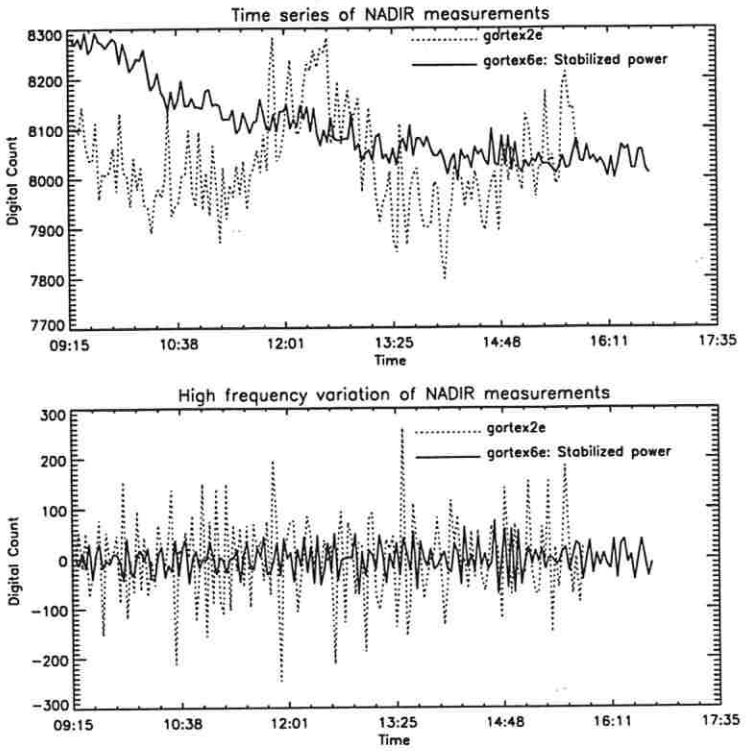

Figure 5.3: Experiment 48 (gortex2e) and 50 (gortex6e) illumination drifts. Upper panel raw data from the two experiments. Lower panel high frequency variations of the two data sets.

position. Table 5.2 summarizes the statistics for each of the examined detector zenith angle. As can be seen from the table, the 95% dispersion varies from 2.5% to 3.5% at each position.

Figure 5.6 shows the time series of the irradiance measured from different detector zenith positions. The $\hat{r}_{0,\theta_d}$ column of Table 5.2 shows the estimated correlation between the time series acquired at the nadir position, with the time series acquired at the other θ_d positions. As expected, measurements acquired at positions close to the nadir have a stronger correlation with the nadir measurement than measurements acquired at positions further away from nadir (i.e. $\hat{r}_{0^\circ,5^\circ} = 0.96$ and $\hat{r}_{0^\circ,50^\circ} = 0.70$).

5.2.4 The irradiation drifts of other sources

In a set of experiments, we maintained a HeNe laser on for three subsequent nights. The laser was positioned over the GOSSEN lux-meter. A fourth measurement series was made with a CCD camera over a 100 W lamp spot. All the measurements started before the end of the work day, i.e. at 17:30, and were left logging through the night until the next workday started. All four measurement

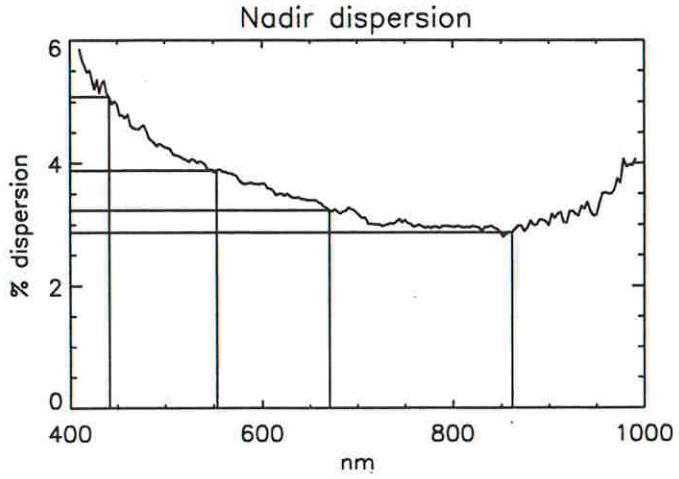

Figure 5.4: The 95% dispersion values for the nadir position, plotted as a function of wavelength. We have indicated the MISR wavelengths in the plot. Data are from Experiment 49.

series showed intensity drifts of a non consistent pattern. The drift in the 100 W lamp and the laser source stabilized in three of the four data sets after 20:00 hours local time. At that time very few, if anyone, were working in the building, which seems to coincide with less variability in the AC power feeding the source (see [126] for additional details).

5.3 The symmetry of the measurements taken from the left and the right EGO hemisphere

In the previous section we examined the stability of the irradiation source at different source elevation positions in the cross plane. During the analysis we noticed that measurements taken at symmetric positions in the cross plane, i.e. $\theta_d = \pm 10°$, where not equal, and that the difference was greater than what could be explained by the illumination drift. In this section we examine the relative difference between measurements made in the left and the right EGO hemisphere.

The goniometric hemisphere is illustrated in Figure 5.7. The left hand side of the goniometric hemisphere is defined as the quarter sphere where $\phi_d < 180°$ and $\theta_d < 0°$ or where $\phi_d > 180°$ and $\theta_d > 0°$. We have defined the sign of θ_d to be negative for detector azimuth positions greater than 180°, the detector elevation is always negative on the left side of the goniometric hemisphere, and positive on the right side of the hemisphere. In the principal plane ($\phi_d = 0°$), θ_d is negative for the forward scattering direction, and positive in the backscatter direction. The detector is in an upright position on the right hand side, and

Table 5.2: Summary of SE590 data from Experiment 49

θ_d	$\overline{Y}$ [DC]	$\hat{s}_Y$	95% dispersion	Y_{Mid}	$\hat{s}_{half}$	$\hat{r}_{0,\theta_d}$	$\hat{r}_{-\theta_d,\theta_d}$
-50	7711	126	± 3.2 %	7734	238	0.836	0.623
-45	7892	135	± 3.3 %	7919	275	0.851	0.641
-40	8044	142	± 3.5 %	8111	280	0.884	0.681
-35	8131	133	± 3.2 %	8194	247	0.878	0.623
-30	8209	144	± 3.4 %	8298	302	0.865	0.746
-25	8278	146	± 3.4 %	8347	269	0.861	0.752
-20	8314	149	± 3.5 %	8359	272	0.909	0.786
-15	8315	134	± 3.1 %	8319	244	0.911	0.835
-10	8323	140	± 3.3 %	8336	267	0.943	0.854
-5	8306	146	± 3.4 %	8336	292	0.952	0.940
0	8247	136	± 3.2 %	8242	264	1.000	1.000
5	8112	136	± 3.3 %	8105	286	0.964	0.940
10	8066	126	± 3.1 %	8025	284	0.900	0.854
15	7997	127	± 3.1 %	7970	289	0.890	0.835
20	7931	122	± 3.0 %	7938	263	0.869	0.786
25	7876	114	± 2.8 %	7878	288	0.876	0.752
30	7834	111	± 2.8 %	7858	258	0.838	0.746
35	7831	111	± 2.8 %	7853	238	0.708	0.623
40	7807	100	± 2.5 %	7828	219	0.746	0.681
45	7774	103	± 2.6 %	7819	225	0.731	0.641
50	7698	118	± 3.0 %	7722	253	0.698	0.623

inverted (upside down) on the left hand side.

5.3.1 The left–right symmetry of the measurements in the cross plane.

The data from the experiment explained in the previous section (Experiment 49) were also used to examine the difference between reflection properties of the left and the right hand side of the EGO hemisphere. Figure 5.5 shows a plot of the average value of the digital counts from each θ_d position, as well as the maximum, minimum and standard deviation of the measurements from each position. We clearly see that the left hand side has higher intensity values than the right hand side. Figure 5.6 shows the time variation of the intensity data for the $\theta_d = \{\pm 50°, \pm 30°, \pm 20°, 0°\}$ positions. We see that the asymmetry is a systematic offset, regardless of the time variations. However, the offset is dependent of the θ_d position. At $\theta_d = \pm 50°$ there appears to be no significant offset. The $\hat{r}_{-\theta_d,\theta_d}$

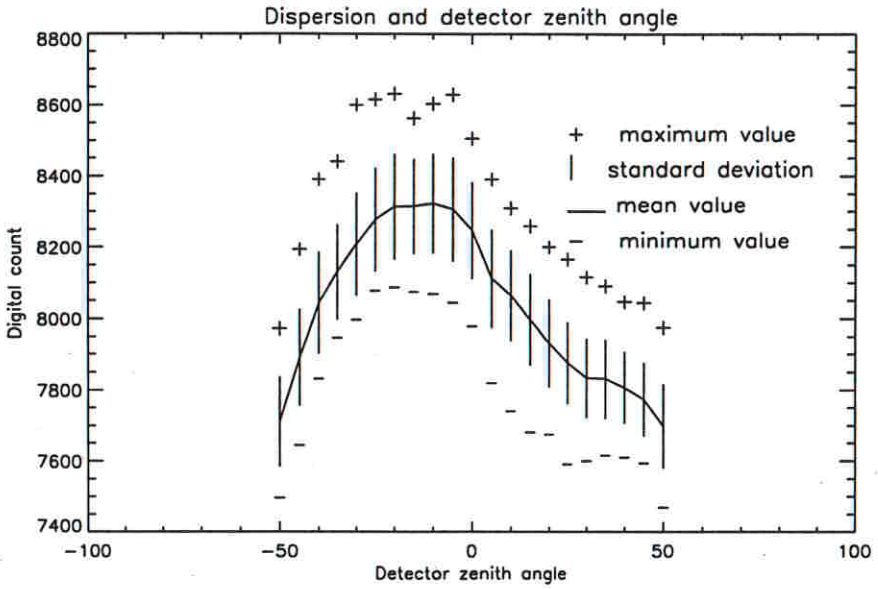

Figure 5.5: The average digital count value as a function of detector zenith angle (θ_d) position in the principal plane ($\phi = 90°$, $\theta_s = 30°$), plotted together with the maximum, minimum and standard deviation of the digital count. Data from Experiment 49.

column of Table 5.2 gives the estimated correlation coefficient between the time-series acquired on the left and the right hand side of the EGO. The low correlation for the time series acquired at low zenith angles ($\hat{r}_{\pm 50°} = 0.62$), is most likely due to the long time span (up to 6 minutes) between the measurements from the two hemispheres of the EGO.

Figure 5.8 shows scatter plots of the measurements from the right hand side of the hemisphere, against the measurements from the left hand side of the hemisphere. The straight line in each plot is the symmetry line, around which the measurements should be grouped if no asymmetries were present. The average value of the measurements from the left side of the goniometric hemisphere were $\{0.2\%, 3.0\%, 4.7\%, 4.7\%, 3.1\%, 2.4\%\}$ higher ($\hat{s}_{abs}$), respectively, than on the right side of the goniometric hemisphere for the angle pairs $\theta_d = \{\pm 50°, \pm 40°, \pm 30°, \pm 20°, \pm 10°, \pm 5°\}$ respectively. There is a significant difference (at the 95% confidence level) for all of these positions, except for the $\theta_d = \pm 50°$ positions.

5.3.2 The difference between measurements made from the left and the right EGO hemispheres

Experiments 52 and 54 were designed to further examine the apparent difference between the left and the right hemisphere of the goniometer. In this experiment, the detector recorded at azimuth positions 330° around the goniometer. The

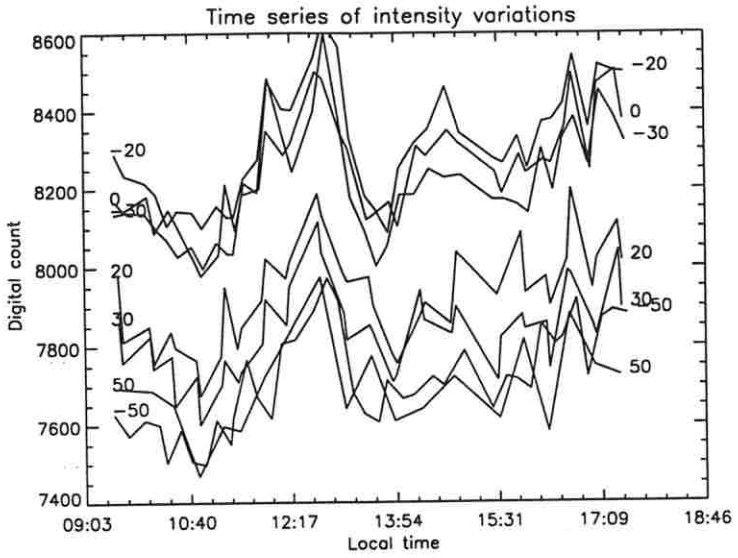

Figure 5.6: The time series for some of the measured detector zenith positions. The number at the start and at the end of each curve indicates the detector zenith angle (θ_d). Data from Experiment 49.

data for positions $\phi_d \leq 180°$ were taken first. The lamp was then shut off and cooled for 10 minutes, before it was dismounted in order to move the ϕ_d arc past the lamp. The lamp was re-mounted, and the measurements for $\phi_d > 180°$ were then performed. For the measurements made with $\phi_d < 180°$, the detector was in an upright position in the right hemisphere of the EGO, and in an inverted (upside down) in the left EGO hemisphere. Likewise for measurements made with $\phi_d > 180°$, the detector was upright in the left EGO hemisphere.

We attached an voltage stabilizer to the 1000 W lamp, and a second SE590 (SE590/G1) was set up in a fixed position adjacent to the goniometer. The measurements with the extra spectrometer were acquired manually, synchronous with the measurements acquired with the principal spectrometer (SE590). A GOSSEN lux-meter was positioned on the brightest edge of the spot, outside the field of view of the detector. The lux-meter acquired measurements once every minute. Table 5.3 shows the dispersion statistics for the auxiliary data logged during the experiment.

Table A.1 and Figure 5.16, presented at the end of this chapter, shows the intensity data from Experiments 52 and 54, as logged from $\phi_d = x°$ and $\phi_d = x° + 180°$. The shift of the curves ($\phi_d = x$ and $\phi_d = x + 180°$) is probably due to the intensity drift of the source. The average difference between the data logged from $\phi_d = x$ and $\phi_d = x + 180°$ varied between 2% and 4% ($\overline{\overline{Y}_{\phi=x°} - \overline{Y}_{\phi=x°+180°}}$), for $\theta_s = 30°$. We see from the figure that for detector zenith angles $\theta_d < |50°|$ the shape of the curves follow each other closely, but for some of the more extreme an-

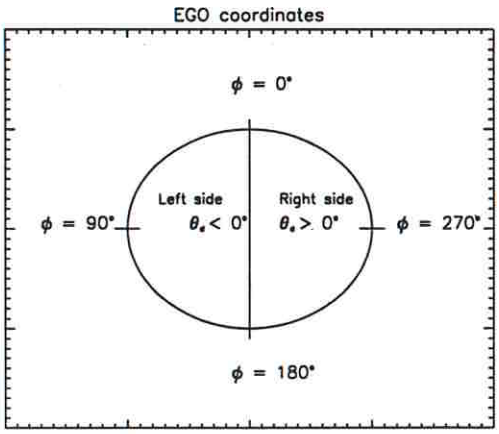

Figure 5.7: An illustration of the left and the right EGO hemisphere.

Table 5.3: Summary of auxiliary data for Experiment 52 and 54

Instrument θ_s	$\overline{Y}$	$\hat{s}_Y$	$V(Y)$	I
Lux 10°	5882 [Lux]	28	0.96%	55
Lux 30°	6416 [Lux]	19	0.59%	149
Lux 60°	6622 [Lux]	28	0.82%	50
SE590/G1 10°	531.0 [DC]	8.9	3.27%	83
SE590/G1 30°	526.3 [DC]	4.2	1.57%	311
SE590/G1 60°	376.5 [DC]	1.6	0.81%	108

gles there is a gap or step, of up to 8% (at $(\theta_s, \theta_d, \phi) = (30°, -70°, 150°/330°)$ and $(\theta_s, \theta_d, \phi) = (30°, 70°, 30°/210°)$). Another interesting feature to note from Figure 5.16, is the specular reflectance of the reference panel which appears in these plots for $(\theta_s, \phi) = (60°, 0°/180°)$. The specularity of the GORE–TEX^{TM} reference panel is commented further in Section 5.5.

5.3.3 The beam profile of the lamp spot

We used a SBIG-8 CCD camera to form an image of the beam profile of the light sources. The CCD image of the 1000 W lamp spot was taken from the nadir position. A contour plot of the lamp spot is shown in Figure 5.9. As can clearly be seen from the image, the lamp spot is not left-right symmetrical. Figure 5.10 shows the principal plane ($\phi_d = 0°$ or $\phi_d = 180°$) and the cross plane ($\phi_d = 90°$ or $\phi_d = 270°$). We registered a 20% intensity drop 15 cm from the center of the EGO in the backward direction, and a 50% drop in the forward direction. In the cross plane the intensity drop 10 cm from the EGO center was 15% on the left

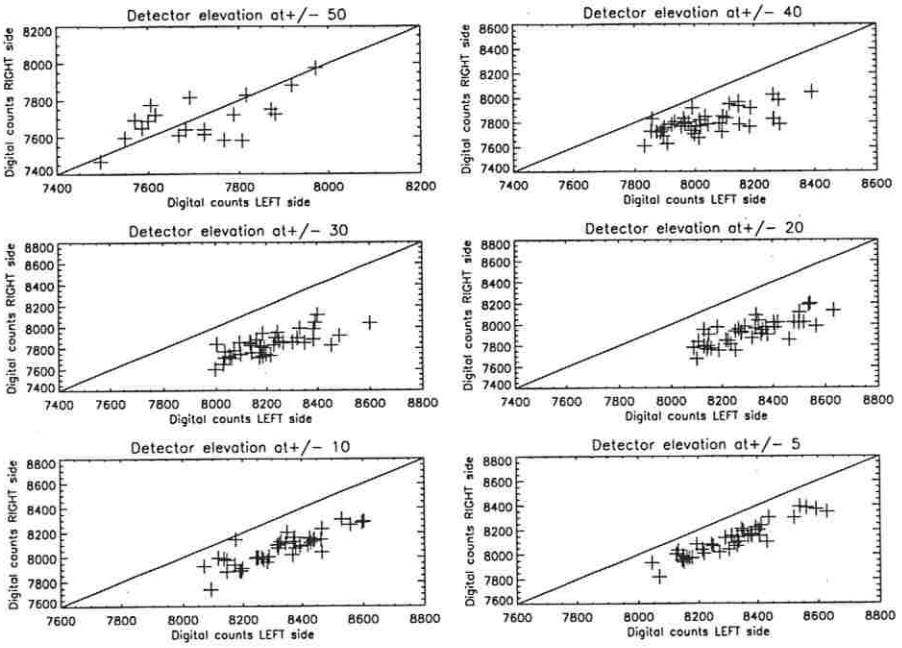

Figure 5.8: Scatter plots showing measurements from the right hand side plotted against those from the left hand side. Data from Experiment 49.

side, and 25% on the right side. The inhomogeneity of the lamp spot is expected to be worse for larger source zenith angles.

An EGO investigator group from The University of Zürich, Switzerland, made a footprint of the lamp with a GER-3700 -radiometer at $\lambda = 450$ nm and $\theta_s = 35°$. They found a similar decrease of the lamp irradiance of up to 50%. They report no wavelength dependence of the lamp footprint [120, 121].

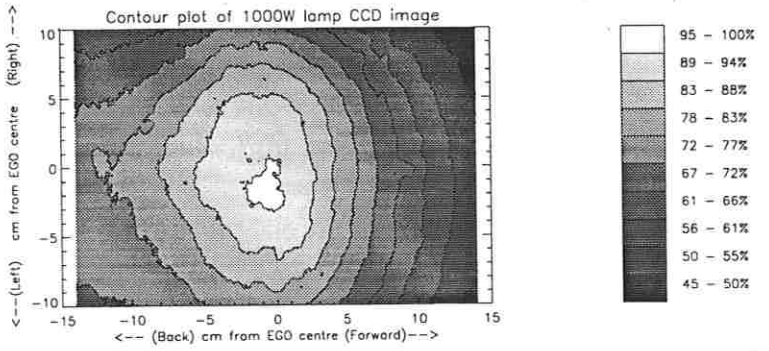

Figure 5.9: Contour plot of a CCD image of the 1000 W lamp spot. $\theta_s = 30°$

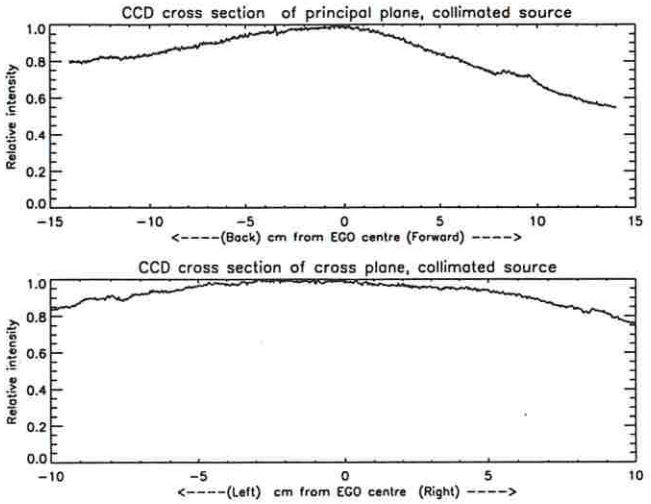

Figure 5.10: The cross plane and the principal plane of the 1000W lamp spot.

5.4 The alignment of the EGO arcs

In the previous sections we documented a drift in the intensity of the radiation and a left–right asymmetry in the light spot. In this section we examine the accuracy of the positioning of the detector center of view.

In order to study the structural alignment of the EGO arcs, we mounted a laser on the EGO detector sled, pointing at the target platform. We then recorded the position of the laser spot as a function of the EGO detector sled position. This is equivalent to testing how much the center of field of view of a detector changes as the detector moves along the EGO arcs.

A MELLES GRIOT HeNe green laser (543 nm) was mounted on the detector arc at the correct height and distance from the the detector sled. The detector arc was then moved from $\theta_d = -70°$ to $\theta_d = 70°$ for azimuth positions $\phi_d \in \{0°, 45°, 90°, 135°\}$, in order to map the variation of the center point as a function of detector zenith. The position of the laser spot at each position was recorded on a fixed millimeter paper. The diameter of the laser spot was approximately 2 mm, when positioned at nadir, and approximately 10 mm when positioned at -70^0.

To check the effect of the level of the target, the target platform was moved up 1 cm (+1 cm) or down 1 cm (-1 cm), relative to the Level 0 position. Level 0 is the mechanical baseline of the system, where a targets should normally be placed.

Figure 5.11 shows some of the resulting measurements (a summary of the data can be found in Table A.2 in Appendix A). The coordinate systems in the figures have the vertical center point ($\theta_d = 0°$, the measurement marked 7) as their origin. We see that the displacement of the laser is largest for $\theta_d = -70°$ and

$\theta_d = -60°$ (the measurements marked 0 and 1 in Figure 5.11). The maximum displacement of the laser spot was 9.3 cm, measured for $\phi = 90°$, and level $= -1$. The average displacement from the center point varied between 1.1 cm and 3.0 cm for the twelve measurement series. As seen from the figure, the leveling of the target has an effect of the center of the field of view. We observe that the measurements for positions $\theta_d < -60°$ deviate the most from the nominal center of view. We found that if the detector arc was leveled only 1 mm differently, it could have an effect of displacing the center of view by several centimeters for $|\theta_d| > 60°$

A similar test was performed for the detector azimuth. The center of the coordinate system in these measurements was the mechanical center of the system. The laser was positioned at three different zenith positions $\theta_d \in \{-70°, -45°, 0°\}$ and then moved in azimuth to positions $\phi_d \in \{0°, 15°, \ldots, 345°\}$. These measurements are shown in Figure 5.12 (a summary of the data can be found in Table A.3 in Appendix A). We see from the figure that the radius of the circle mapped by the laser increases from 1.2 cm for $\theta_d = 0°$ to 3.0 cm for $\theta_d = -70°$.

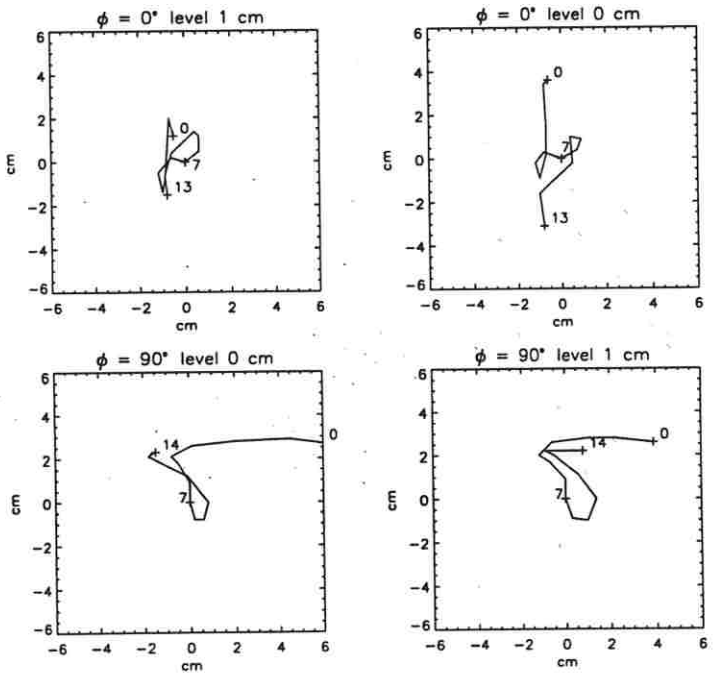

Figure 5.11: The trace of the laser spot incident on the target support, as the laser was moved in zenith. The points marked by the number 7 corresponds to the $\theta_d = 0°$ position, points marked 0 are the $\theta_d = -70°$ positions and points 13 or 14 are the $\theta_d = 60°$ or $\theta_d = 70°$ positions.

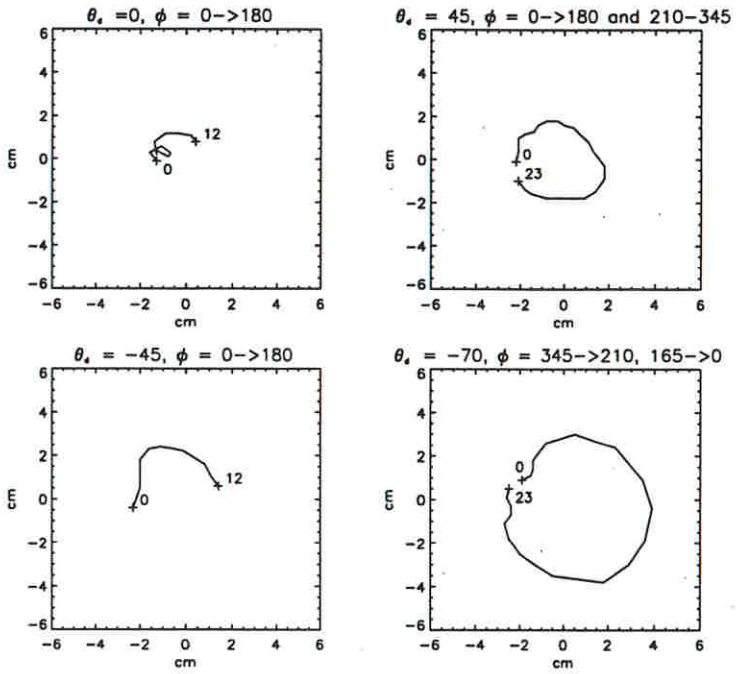

Figure 5.12: The trace of a laser spot incident on the target support as the laser was moved in azimuth. The points marked by the number 0 corresponds to the $\phi = 0°$ position, point 12 is the $\phi = 180°$ position and point 23 is the $\phi = 345°$ position.

5.5 Estimation of the BRF of the GORE–TEX^{TM} reference panel

As noted in the introduction to this chapter, one of the underlying assumptions for BRF estimation is that the reference panel is a perfectly diffuse surface. The errors introduced by this assumption and the calibration of reference panels have been the purpose of many investigations e.g. [57, 72, 116, 152]. In this section we examine the directional reflectance properties of the GORE–TEX^{TM} reference panel.

The BRF distribution of the GORE–TEX^{TM} reference panel, $\hat{\rho}_r^{\lambda}(\theta_s, \theta_d, \phi)$, was estimated based on corresponding measurements of the GORE–TEX^{TM} panel and a Spectralon reference panel using a 1° FOV:

$$\hat{\rho}_r^{\lambda}(\theta_s, \theta_d, \phi) = \frac{y^{\lambda}_{GORE-TEX}(\theta_s, \theta_d, \phi)}{y^{\lambda}_{Spectralon}(\theta_s, \theta_d, \phi)} \tag{5.3}$$

where $y^{\lambda}_{GORE-TEX}$ and $y^{\lambda}_{Spectralon}$ are the measurements of the GORE–TEX^{TM} and Spectralon reference panels respectively. The 1° FOV was used to ensure that the 50 cm$\times$ 50 cm Spectralon panel was within the field of view of the detector for all zenith angles. Figure 5.13 shows the principal plane measurements for

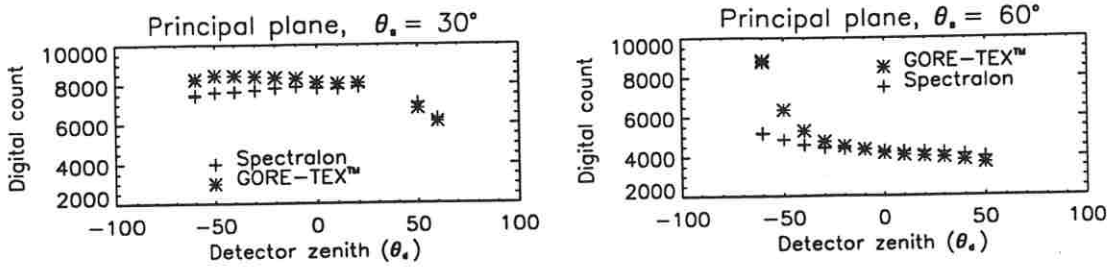

Figure 5.13: The principal plane measurements for the GORE–TEX^{TM} and Spectralon reference panel, measured with a stabilized voltage source and FOV = 1°. The data are from Experiment 55 to 58

the GORE–TEX^{TM} and Spectralon reference panels. The Spectralon reference panel was less specular than the GORE–TEX^{TM} reference panel for large illumination zenith angles. In the case of a field of view of 1°, and source zenith angle $\theta_s = 60°$, the $\hat{s}_{half}$ of the reflectance in the principal plane was 41% for the GORE–TEX^{TM} panel, whereas for the Spectralon panel the $\hat{s}_{half}$ was 13%. This result shows that both panels are specular, but that the GORE–TEX^{TM} panel is more specular than the Spectralon panel. We therefore chose to use this estimate of the BRF of the GORE–TEX^{TM} to correct the BRF estimates as in Eq. (4.1). Figure 5.14 shows the estimated BRF for the GORE–TEX^{TM} reference panel, for source zenith angle $\theta_s = 30°$ and $\theta_s = 60°$. As can be seen from the figure, the BRF for $\theta_s = 30°$ has a weak depression in the backscattering direction, whereas for $\theta_s = 60°$, and $\lambda = 670$ nm the BRF has a sharp specular peak. The measurements (Experiment 55 to 58) used to estimate the BRF of the GORE–TEX^{TM} reference panel were made with a stabilized power source.

The Spectralon reference panel was certified by Labsphere Inc. to have a hemispherical reflectance factor of 0.99 for a source incidence angle of 8°. However, in the cross plane, the GORE–TEX^{TM}/Spectralon reflectance factor was 1.02± 0.03 for $\theta_s = 30°$, and 0.97 ± 0.01 for $\theta_s = 60°$. The difference can be explained by the intensity drift of the source, and the non-diffuse reflectance properties of the reflectance panels (see Section 3.6 for additional details on general properties of GORE–TEX^{TM} and other PTFE materials).

5.6 Correction for irradiation drift

Since we have found (Section 5.2.3) that the variation in the irradiation at different detector elevation positions were highly correlated with the intensity drift measured at the nadir position, we decided to use this to correct for the low-frequency intensity variation.

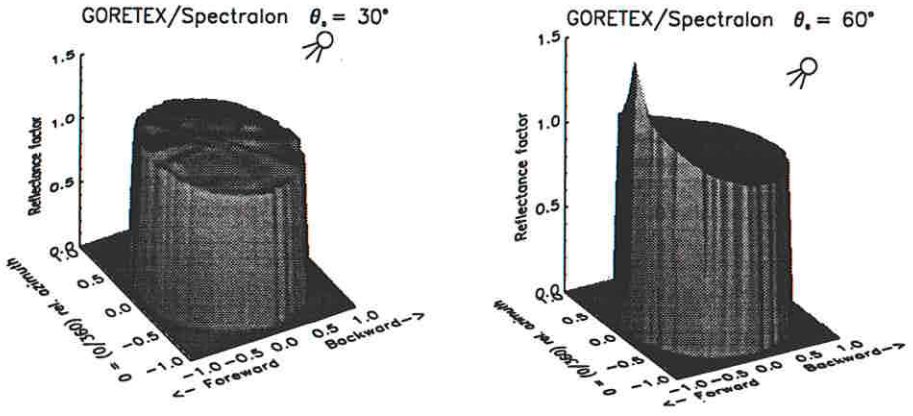

Figure 5.14: The estimated BRF distribution of the GORE–TEX^{TM} reference panel. The estimate was based on corresponding measurements of the GORE–TEX^{TM} panel and a Spectralon reference panel using a 1° FOV. The BRF to the left is for source zenith angle 30° and to the right for 60°. The data are from Experiment 55 to 58

A way of correcting the EGO data for the irradiation drift in the acquired intensity data may be to model the drift in each data set by constructing a correction function based on the nadir measurements from each series. The high correlation ($\hat{r}_{0°,\theta_d} > 0.7$, in Table 5.2) indicates that the same correction function may be used at all detector zenith angles. A source intensity correction function can be constructed from measurements from an independent detector that is dedicated to monitor the intensity of the source. This could not be done for our data, since the auxiliary lamp monitoring was not available, at the EGO.

To correct for the intensity drift effect, we estimated a correction factor based on the measurements made at the nadir position of the system. The detector returned to nadir approximately every 10'th minute, which is thus the typical update time for the intensity drift. The correction factor $\hat{C}^{\lambda}(\phi, \theta_s)$ for each relative azimuth angle, ϕ, and source zenith angle θ_s was estimated as:

$$\hat{C}^{\lambda}(\theta_s, \phi) = \frac{y^{\lambda}(\theta_s, \theta_d = 0°, \phi)}{\sum_{i=1}^{I} y^{\lambda}(\theta_s, \theta_d = 0°, \phi_i)/I} \tag{5.4}$$

where I is the number of nadir measurements $(\theta_s, \theta_d = 0°, \phi_i)$.

An estimate of the effect of the correction is to examine the data that were continuously recorded in the cross plane. In Experiment 49, the detector made 40 passes through the cross plane. The illumination drift at each detector elevation position were commented in detail in Section 5.2.3. The measurements from each cross plane pass was updated using a correction factor estimated as in Eq. (5.4). The reduction in the 95% dispersion around the mean value for each detector elevation position is clearly evident from Figure 5.15 (for details see Table A.4). We see that the dispersion reduction is largest for the positions close to the nadir

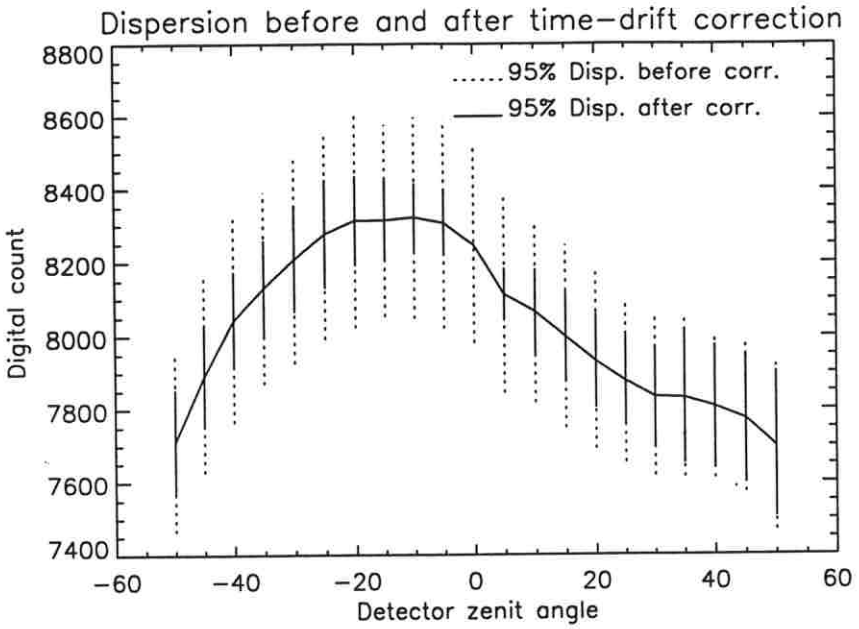

Figure 5.15: The average value for each detector zenith angle (θ_d) position in the principal plane ($\phi = 90°$, $\theta_s = 30°$), plotted together with the 95% dispersion before and after time-drift correction. (Data from Experiment 49.)

position. We also note that the positions where the time-series data had the lowest correlation with the nadir time series, have gained least from the correction. The details on the improvement of the data precision before and after the intensity drift correction are summarized in Table A.4. The average 95% dispersion was reduced from $3.1 \pm 0.2\%$ to $1.6\% \pm 0.6\%$, by the use of our correction factor.

5.7 Final precision and correction of the reflectance factor estimates

In the following section we give a short discussion of the results of the investigated sources of variation in the EGO data, and their effect on the reflectance factor estimates.

The illumination drift

The drift of the radiant intensity data documented in Experiments 48, 49 and 50, and discussed in Sections 5.2.1 and 5.2.3, shows that with the present configuration one can expect a dispersion of up to 3.5% due to the irradiation drift of the 1000 W lamp. Data from a HeNe laser and a 100 W lamp source, showed that an intensity drift of the same order was present also for these light sources.

The high frequency variations in the intensity of the 1000 W halogen lamp was reduced from 2.1% to 0.7% by using a voltage equalizer across the lamp. A plausible explanation for the intensity drift is an unstable power supply to the laboratory. However, to verify if variations in the voltage supply is the main cause of the variations in the light sources, the power supply to the EGO laboratory should be monitored during a long period of several weeks. Other explanations for the high frequency ripple is thermal noise in the detectors, and "room" optical noise induced by people and computer screens. By correcting for the low frequency component of the intensity drift, the dispersion in the reflectance measurements can be improved to 2% or better.

The asymmetry of the lamp spot

The CCD image of the light-spot presented in Figure 5.9, Section 5.3.3, clearly shows a left/right asymmetry in the light-spot. This is an indication that the local intensity variations within the footprint is the cause of the asymmetry found in our SE590 data. This asymmetry is probably due to irregularities in the collimating lenses of the 1000 W lamp. The data from Experiment 52 showed that the same asymmetry was found when rotating the detector 180° in azimuth. This is again an indication that the asymmetry is caused by the source. Since this effect is equally present for both target and reference panels, the effect of the asymmetry of the lamp-spot will be reduced automatically in the reflectance factor estimates.

The step

A "step" of up to 14% (Table 5.4) was observed in the intensity data for measurements acquired at $|\theta_d| \geq 60°$. The "step" is probably caused by a combination of the asymmetry in the source, documented in Section 5.3 and by the displacement of the center of the detector field of view, discussed in Section 5.4. For detector zenith positions $|\theta_d| > 60°$ the field of view covers most of the lamp spot. The lamp spot is less homogeneous in the vicinity of the edges than in its center. The displacement of the center of the detector field of view is largest at these angles, as seen from Figure 5.11.

To determine if it is possible to correct for the "step", a closer analysis must be carried out of the homogeneity of the lamp spot compared to the field of view of the detector. However, since we found that the displacement of the field of view was strongly dependent upon the EGO detector position, one would have to document the displacement at all detector positions. The displacement is dependent on the leveling of the target, and on how the detector is mounted on the detector sled. It is therefore probably not possible to correct accurately for this effect.

We found in Section 5.3 that the intensity measurements acquired from both

sides ($\phi_d = x°$ and $= x° + 180°$) of the EGO hemisphere, were displaced by the illumination drift for detector azimuth angles in the range $|\phi_d| < 50°$. The source dependent asymmetry was consistently measured from both sides for the same range of azimuth angles. For extreme detector zenith angles $|\theta_d| > 60°$ the difference between the data logged from the two sides varied in a non-consistent way. For the measurements acquired at $\pm 70°$ e.g., the difference varied between 3% and 8%.

Since we found that the "step" described in this chapter can be explained by the inhomogeneity of the lamp spot and the displacement of the center of the area of view, this effect is reduced for the reflectance factors. However, since we found that the displacement is dependent on the level of the target, there will be a measurable difference, since the targets and reference panel have different heights.

Reflectance factor estimates of the targets

In Table 5.4 we show the results of a comparison of measurements from the detector azimuth planes $\phi = 175°$ and $\phi = 185°$. The results are presented for the lichen targets, the GORE–TEX^{TM} reference panel reflectance data, and for the reflectance factor data. If we assume that the targets are homogeneous with a random orientation in azimuth, and that the target and reference panel are measured under equal illumination and measurement conditions, the reflectance factor estimates will exhibit a symmetrical reflectance for these two planes. We found that for the reflectance data, the "step" varied between 6–14% (absolute difference between $y(|(\theta_d| \leq -60, \phi = 175°)$ and $y(|\theta_d| \leq -60, \phi = 185°))$, for the target and reference panel measurements. For the reflectance factor data, the step was reduced to an absolute difference of 1–8%. This corresponds to an absolute difference in the reflectance factor of 0.008–0.032. The effect was reduced further by the time drift correction to 1–6% or a 0.0015–0.0052 reflectance factor difference. The column for $\theta_d = 10°$ in Table 5.4 is included to illustrate the precision at positions where the precision is affected only by the variations in the illumination. In the reflectance factor data we see that for the position $(\theta_d, \phi) = (10°, 175°/185°)$, $\hat{s}_{abs} < 0.025$ for the uncorrected data, and $\hat{s}_{abs} < 0.008$ for the illumination drift corrected reflectance factors. We repeated this analysis for the other MISR wavelengths and found that for the corrected data $\hat{s}_{abs} < 0.016$. We thus conclude that the estimated RF values are within 2% of their mean value. This estimate agrees with the results of Sandmeier *et al.* [121] who report that the reproducibility of BRF data obtained in the EGO lies within 1–9% rmse, depending on target type, wavelength range and measurement duration.

Table 5.4: Improvement of precision. Data from Experiments 23, 24, 26, 29, 31. Comparison of data from the planes $\phi = 5°$ and $\phi = 175°$. The "after" refers to illumination-drift corrected data.

Target	θ_s	θ_d	$= 70°$	$\theta_d =$	$60°$	$\theta_d =$	$10°$
		$100\hat{s}_{abs}/Y_{mid}$	$\hat{s}_{abs}$	$100\hat{s}_{abs}/Y_{mid}$	$\hat{s}_{abs}$	$100\hat{s}_{abs}/Y_{mid}$	$\hat{s}_{abs}$
GORE–TEX^{TM}	30°	7.06%	571.88	5.75%	487.50	1.43%	115.63
after:		6.75%	566.40	5.43%	477.68	1.12%	93.54
GORE–TEX^{TM}	60°	8.92%	937.50	14.20%	1318.75	7.84%	337.50
after:		2.68%	288.80	7.98%	758.46	1.59%	70.38
Flavocetraria nivalis	30°	11.99%	195.31	12.44%	207.81	4.38%	100.00
after:		7.51%	122.04	7.96%	132.64	0.11%	2.54
Flavocetraria nivalis	60°	10.74%	114.06	6.50%	65.63	2.91%	32.81
after:		7.97%	85.17	3.73%	37.92	0.14%	1.61
Cladina stellaris	30°	9.47%	127.34	11.33%	159.38	2.25%	40.63
after:		5.79%	76.21	7.65%	105.37	1.43%	25.35
Cladina stellaris	60°	7.88%	61.72	8.95%	70.31	3.77%	34.38
after:		9.13%	69.94	10.20%	78.37	2.52%	22.49
Reflectance Factor							
Flavocetraria nivalis	30°	4.94%	0.0099	6.70%	0.0132	2.95%	0.0083
after:		0.76%	0.0015	2.53%	0.0048	1.23%	0.0033
Flavocetraria nivalis	60°	1.82%	0.0018	7.72%	0.0084	4.93%	0.0129
after:		5.29%	0.0052	4.24%	0.0045	1.45%	0.0037
Cladina stellaris	30°	2.42%	0.0040	5.60%	0.0093	0.82%	0.0018
after:		0.96%	0.0015	2.22%	0.0035	2.55%	0.0054
Cladina stellaris	60°	1.04%	0.0008	5.27%	0.0045	11.60%	0.0246
after:		6.45%	0.0046	2.23%	0.0018	4.12%	0.0083

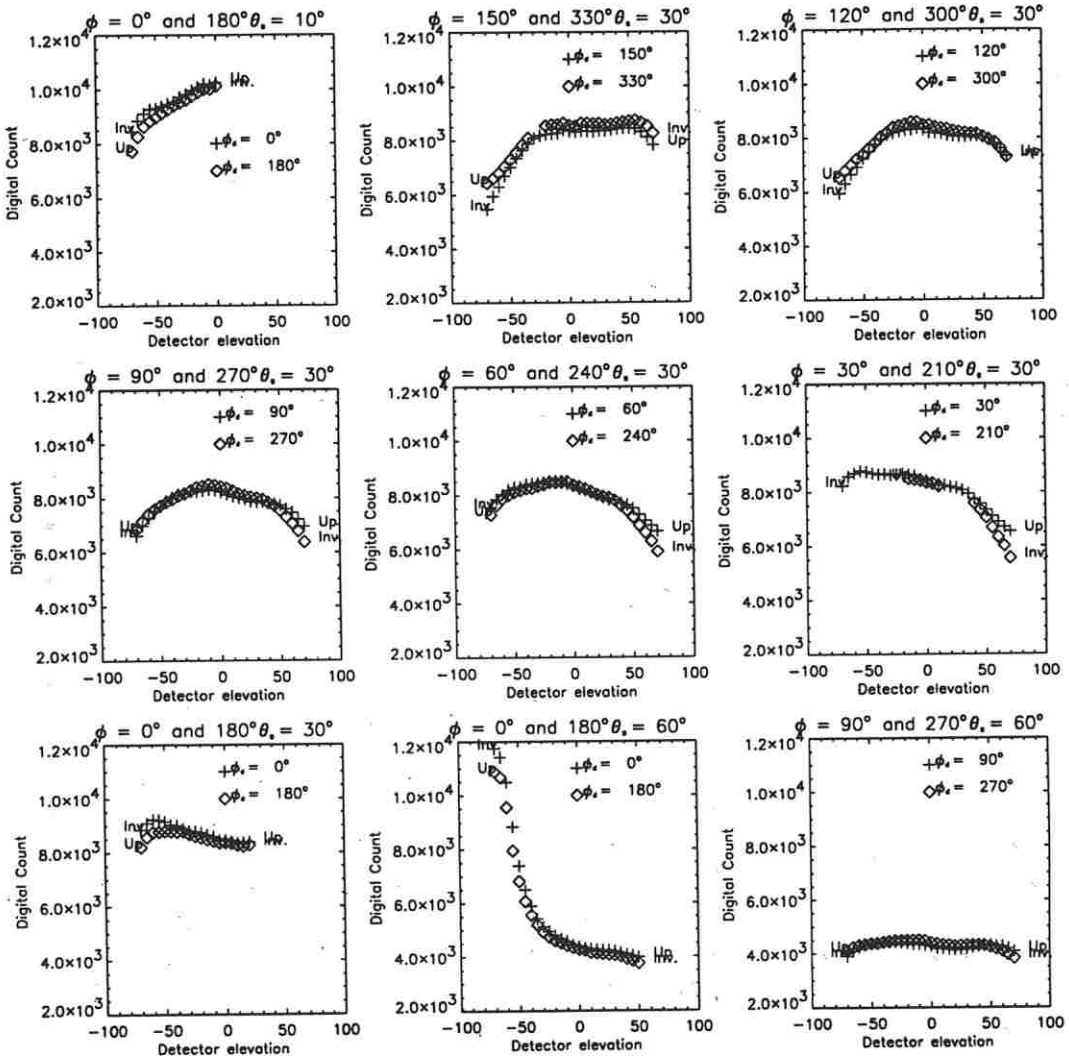

Figure 5.16: Data from Experiment 52, logged from the two sides of the goniometer. The step in the data can be seen as a large difference between the $\phi_d = x$ and $\phi_d = x + 180^o$ measurements for detector zenith angles $|\theta_d| > 60^o$. "Inv." denotes that the detector was in an inverted position, and "Up" denotes an upright position.

Chapter 6

Spectral Characterization of the Targets

In this chapter we characterize the estimated spectral RF of the main targets in the wavelength range 400 nm $< \lambda <$ 1100 nm. We present the spectral signatures for dry as well as wet targets. We compare the spectral signatures measured in the EGO laboratory with spectral signatures measured during a field campaign to natural habitats of the selected lichen and moss targets. The EGO based RF estimates presented in this chapter were estimated by means of Eq. (4.1), and the intensity drift was corrected in accordance with Eq. (5.4).

6.1 Spectral signatures of dry targets

In the following section we discuss the spectral signatures of the main targets, measured in a dry condition. Figure 6.1 shows the spectral RF for the main targets, measured from the nadir position for source zenith angles $\theta_s = \{10°, 30°, 60°\}$.

As seen in Figure 6.1, the green-greyish moss *Racomitrium lanuginosum* has a lower RF than the lichens for 450 nm $< \lambda <$ 900 nm. Below 450 nm and above 900 nm the moss has the same level of reflectance as the lichens, for $\theta_s = \{30°, 60°\}$. The moss has a high absorption of energy in the visible bands typical for green vegetation [34, 51, 83]. However, it lacks the sharp reflectance peak at 540 nm which is typical of fresh green vegetation. Instead it has a plateau of higher reflectance between 550 nm and 650 nm. Similar RF curves are typical for the reflectance spectra of dry or stressed leaves, regardless of species [14, 53].

The lichens have a sharp rise in the spectral signatures at about 450 nm. For the $\theta_s = 30°$ case, the estimated RF increases from approximately 0.07 to 0.25 for the *Cladina stellaris* and to 0.34 for the *Flavocetraria nivalis*. The green *Racomitrium lanuginosum* and the yellow *Flavocetraria nivalis* both have a distinct local minimum in the RF curve at 670 nm. This minimum is clearly one

of the chlorophyll absorption bands, and is therefore typical for green vegetation [34, 148]. The "white" *Cladina stellaris* does not have this particular local minimum in the visible red wavelengths. The lichen targets have a sharp increase in the reflectance in the transition between the visible and the NIR wavelengths. The RF of the lichens level out to about 0.53 for $\lambda > 750$ nm. The RF curve for the moss has a longer transition zone, before it flattens out to the same level. Most green vegetation have a steep increase between the visible and the NIR part of the spectrum [34, 51].

The "shape" of the spectral profile of the *Cladina stellaris* agrees with the field measurements of Mulhern [94]. Mulhern however reports a lower reflectance magnitude for the *Flavocetraria nivalis* than for *Cladina stellaris*. The spectral profile of her *Flavocetraria nivalis* is much more similar to the *Cladina stellaris* than to our *Flavocetraria nivalis* spectral profile.

The spectral RF decrease with increasing source zenith angle for the lichen targets in the green and the red part of the spectrum. At 600 nm, the RF is approximately 8% higher for $\theta_s = 10°$ than for $\theta_s = 60°$. In the NIR, the $\theta_s = 10°$ RF estimates are 5% higher than the $\theta_s = \{30°, 60°\}$ estimates which are practically of the same magnitude.

The correlation coefficient (see Table 6.1) estimated as in Eq. (2.30), shows that there is a strong degree of linear correlation between the nadir RF estimates of the targets for different source zenith angle. For the same target, but different source zenith, the estimated correlation coefficient was $\hat{r} \geq 0.994$. Between different targets the correlation coefficient was $\hat{r} \leq 0.979$. The estimated correlation coefficients between the *Cladina stellaris* and the two other targets were also quite high, $0.933 < \hat{r} < 0.979$, while $\hat{r} \approx 0.85$ between the *Flavocetraria nivalis* and *Racomitrium lanuginosum*. This shows that the shape of the spectral signature of the *Cladina stellaris* lies between the *Flavocetraria nivalis* and *Racomitrium lanuginosum*. It shows that by correlating the spectral profiles one can distinguish, or classify the targets, independent of the source zenith angle. The *rms* values in Table 6.1 show that the levels of reflectance of the three species are well separated for the same source zenith angle.

The dry moss has a slightly different shape of the spectral reflectance factor than the lichens. The RF curve for $\theta_s = 60°$ has higher values for all the measured wavelengths than the RF estimates for $\theta_s = \{10°, 30°\}$. The RF estimates of the moss for source zenith $\theta_s = 60°$ showed both a specular peak and a hot spot region, which obviously explains the increase in the RF for the $\theta_s = 60°$ spectral signature. This peculiar result was further verified by examining other EGO datasets.

Ranson *et al.* [113] found that for nadir view angles, the RF's were strongly source zenith angular dependent for canopies with low leaf area index. They explained this by a decrease in contrast between bare soil and vegetation due to shadows as the solar zenith angle increases. They also found that the effect of the solar angle on reflectance was small for well developed canopies with high

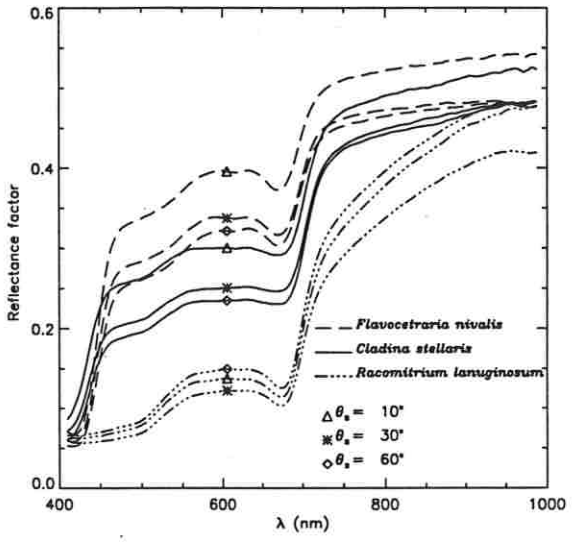

Figure 6.1: Spectral RF for the main targets for position $\theta_d = 0°$, $\phi = 0°$, for $\theta_s = \{10°, 30°, 60°\}$. The target data are from Experiments 24, 25, 27, 33, 36 and 37 (see Appendix B).

leaf area indices. Our results agree with these observations since the moss is a much denser canopy than the lichens. This gives small source zenith dependent variations in the visible part of the spectrum. For the lichens, differences in internal shadowing were observed when the source zenith angle was changed.

6.2 Spectral signatures of moist targets

Several studies have been performed to determine the effects of water content on the spectral reflectance of leaves. In the mid-infrared the spectral response of vegetation is dominated by water absorption. Water absorbs radiation strongly in bands near 1400 nm, 1900 nm and 2700 nm [51]. These wavelengths are outside the range of the spectrometer used in our experiment. However, there is a minor water absorption band at 960 nm, which is in the range of the SE590.

Carter [13] found that a decrease of leaf water content generally increased the reflectance through the 400 – 2500 nm wavelength range for green leaves of six different species. Cox *et al.* [17] found that wet *Cladonia mitis* (a "white" lichen species) had a lower reflectance in the visible wavelengths than a dry sample, and a higher reflectance in the NIR.

To measure the spectral signatures of moistened targets, the $1m^2$ target samples were sprinkled with approximately 3 to 4 liters of water each. The targets where left to soak for approximately 2 hours before the spectral measurements were acquired. When lichens are moistened, the thallus swells as water is ab-

Table 6.1: Correlation ($\hat{r}$) and *rms* between the spectral curves in Figure 6.1.

	C.stellaris $\theta_s = 10°$	*C.stellaris* $\theta_s = 30°$	*C.stellaris* $\theta_s = 60°$	*F.nivalis* $\theta_s = 10°$	*F.nivalis* $\theta_s = 30°$	*F.nivalis* $\theta_s = 60°$	*R.lanug.* $\theta_s = 10°$	*R.lanug.* $\theta_s = 30°$	*R.lanug* $\theta_s = 60°$
C. stellaris $\theta_s = 10°, r$	1.000								
rms	0.000								
C. stellaris $\theta_s = 30°, r$	0.999	1.000							
rms	4.484	0.000							
C. stellaris $\theta_s = 60°, r$	0.998	1.000	1.000						
rms	5.585	1.213	0.000						
F. nivalis $\theta_s = 10°, r$	0.952	0.939	0.933	1.000					
rms	6.101	10.168	11.257	0.000					
F. nivalis $\theta_s = 30°, r$	0.968	0.958	0.953	0.997	1.000				
rms	3.102	5.459	6.535	5.192	0.000				
F. nivalis $\theta_s = 60°, r$	0.976	0.968	0.963	0.994	0.999	1.000			
rms	3.060	4.303	5.309	6.386	1.396	0.000			
R. lanug. $\theta_s = 10°, r$	0.962	0.972	0.975	0.849	0.876	0.895	1.000		
rms	13.749	9.524	8.383	19.411	14.717	13.411	0.000		
R. lanug. $\theta_s = 30°, r$	0.961	0.972	0.975	0.848	0.875	0.894	1.000	1.000	
rms	15.951	11.544	10.446	21.518	16.579	15.296	3.122	0.000	
R. lanug. $\theta_s = 60°, r$	0.966	0.976	0.979	0.856	0.883	0.902	1.000	1.000	1.000
rms	12.669	8.517	7.377	18.339	13.724	12.415	1.283	4.288	0.000

sorbed. When the moss was sprayed with water, the grey leaf tips became transparent. The dry lichens had a relative humidity of approximately 60% and a surface temperature outside the light spot of approximately $23°C$. The moistened lichens had a relative humidity of approximately 83%, and a surface temperature of $21°C$. The dry moss had a relative humidity of 71% and a temperature of $21°C$, whereas the relative humidity and temperature of the moistened moss was 76% and $23°C$, respectively. Figure 6.2 shows the spectral signatures of the main targets in dry (black) and moist (blue) states, observed from nadir.

From Figure 6.2 we seee that the wet *Flavocetraria nivalis* has a higher RF for wavelengths $\lambda > 450$ nm than the dry *Flavocetraria nivalis*. For $\lambda > 500$ nm, the RF for the wet *Flavocetraria nivalis* is approximately 7% higher than the RF for the dry sample.

The wet *Cladina stellaris* has a 2% higher RF for the green and the red wavelengths (500 nm $< \lambda <$ 700 nm) than the dry sample. In the NIR the RF of the moistened sample was 5% higher than for the dry sample. The moistened moss *Racomitrium lanuginosum* has a 2% to 4% lower RF in the visible part of the spectrum, than the dry samples. This result agrees with studies of

Table 6.2: Estimated correlation coefficient $\hat{r}$ and *rms* between the dry and wet spectral reflectance curves in Figure 6.2.

	F. nivalis Dry $\theta_s = 30°$	*F. nivalis* Dry $\theta_s = 60°$	*F. nivalis* Wet $\theta_s = 30°$	*F. nivalis* Wet $\theta_s = 60°$
F. nivalis Dry $\theta_s = 30°, \hat{r}$	1.000			
rms	0.000			
F. nivalis Dry $\theta_s = 60°, \hat{r}$	0.999	1.000		
rms	1.397	0.000		
F. nivalis Wet$\theta_s = 30°, \hat{r}$	0.996	0.992	1.000	
rms	6.654	7.827	0.000	
F. nivalis Wet $\theta_s = 60°, \hat{r}$	0.998	0.997	0.998	1.000
rms	3.948	4.932	3.080	0.000
	C.stellaris Dry $\theta_s = 30°$	*C.stellaris* Dry $\theta_s = 60°$	*C.stellaris* Wet $\theta_s = 30°$	*C.stellaris* Wet $\theta_s = 60°$
C. stellaris Dry $\theta_s = 30°, \hat{r}$	1.000			
rms	0.000			
C. stellaris Dry$\theta_s = 60°, \hat{r}$	1.000	1.000		
rms	1.214	0.000		
C. stellaris Wet $\theta_s = 30°, \hat{r}$	1.000	0.999	1.000	
rms	2.216	3.119	0.000	
C. stellaris Wet $\theta_s = 60°, \hat{r}$	0.999	1.000	0.999	1.000
rms	2.013	2.290	1.541	0.000
	R. lanug. Dry $\theta_s = 30°$	*R. lanug.* Dry $\theta_s = 60°$	*R. lanug.* Wet $\theta_s = 30°$	*R. lanug.* Wet $\theta_s = 60°$
R. lanug. Dry $\theta_s = 30°, \hat{r}$	1.000			
rms	0.000			
R. lanug. Dry $\theta_s = 60°, \hat{r}$	1.000	1.000		
rms	4.287	0.000		
R. lanug. Wet $\theta_s = 30°, \hat{r}$	0.997	0.998	1.000	
rms	4.641	2.828	0.000	
R. lanug. Wet $\theta_s = 60°, \hat{r}$	0.996	0.997	0.999	1.000
rms	5.720	2.524	1.661	0.000

primary[1] effects of water content on reflectance of leaves from several different plant species [13]. In the NIR the moistened moss has a 5% higher RF than the dry sample. Table 6.2 lists the correlation coefficients between the curves in Figure 6.2 and it shows that the correlation between the moist and dry samples are $\hat{r} \geq 0.992$. The weak water absorption band at 960 nm can be observed for the *Flavocetraria nivalis* and the *Racomitrium lanuginosum* in Figure 6.2.

The directional reflectance effects of moistening the targets for the MISR wavelengths, can be examined in Figure 6.3 to 6.6. In these plots, the RF has been plotted for the principal plane only.

For the *Flavocetraria nivalis* and *Cladina stellaris*, the RF's for the moist target are higher than for the dry target for all the investigated wavelengths and $\theta_s = 30°$, in the principal plane. The same pattern is observed for *Flavocetraria nivalis* for $\lambda = \{441, 559\}$ nm, and $\theta_s = 60°$ (Figure 6.3 and 6.4, right column). For $\lambda = \{670, 862\}$ nm and $\theta_s = 60°$ (Figure 6.5 and 6.6, right column), the

[1]Primary effects can be explained by radative properites of water, thus secondary effects of water include the influence of water on absorption by other substances in the leaf such as pigments [13].

forward scattering is higher for the wet *Flavocetraria nivalis* than for the dry *Flavocetraria nivalis*. In the backscattering direction, there is no significant difference. The same directional reflectance pattern can be observed for the *Cladina stellaris* for $\lambda = \{559, 862\}$ nm and $\theta_s = 60°$ (Figure 6.4 and 6.6, right column). We observe no significant difference in the directional scattering for the *Cladina stellaris* target for $\lambda = \{441, 670\}$ nm and $\theta_s = 60°$(Figure 6.3 and 6.5, right column).

For the *Racomitrium lanuginosum* the RF in the principal plane of the moist target is lower than for the dry target for $\lambda = \{441, 670\}$ nm and $\theta_s = \{30°, 60°\}$ (Figure 6.3 and 6.5). For $\lambda = 559$ nm and $\theta_s = 30°$ (Figure 6.4, left column), there is a minimal difference in the directional RF's. For $\lambda = 559$ nm and $\theta_s = 60°$ (Figure 6.4, right column), the wet *Racomitrium lanuginosum* has a slightly higher reflectance factor than the dry target in the forward scattering direction, whereas the opposite is the case in the backscattering direction. For $\lambda = 862$ nm (Figure 6.6), the wet *Racomitrium lanuginosum* has a higher RF than the dry target, except for $\theta_s = 60°$, which is in the backscattering direction.

Gauslaa [35] reports lower reflectance of wet *Cladina stellaris* and *Flavocetraria nivalis*, than for dry, for both visible and NIR wavelengths. However, these measurements were made from samples consisting of several layers of lobes, carefully arranged in order to minimize the voids between the individual lobes. In his experiments the samples were first measured in a dry state, and subsequently moistened, without removing the samples from the photospectrometer. Carter [14] found a higher reflectance in the visible wavelengths for leaves of vascular plants under water stress. However, in the case of the EGO and in field measurements, we measured the response of a whole canopy, in contrast to the reflectance of a single reflecting element of the canopy. The reflectance of the canopy is of course dependent on the structure of the whole canopy, as well as on the absorption features of the single elements comparing the canopy.

Our results indicate a higher RF for the wet lichens, than for the dry, in both visible and NIR wavelength bands. A possible explanation for the increased spectral reflectance of the moistened lichens in the visible region, is that the physical swelling of the lichens resulted in a denser canopy and therefore less internal shadowing. A second explanation is linked to biophysical properties of the pigments of the lichens. Lichens becomes metabolically active within a few minutes after they have absorbed water [115], although it may take longer for photosynthesis to reach optimal levels.

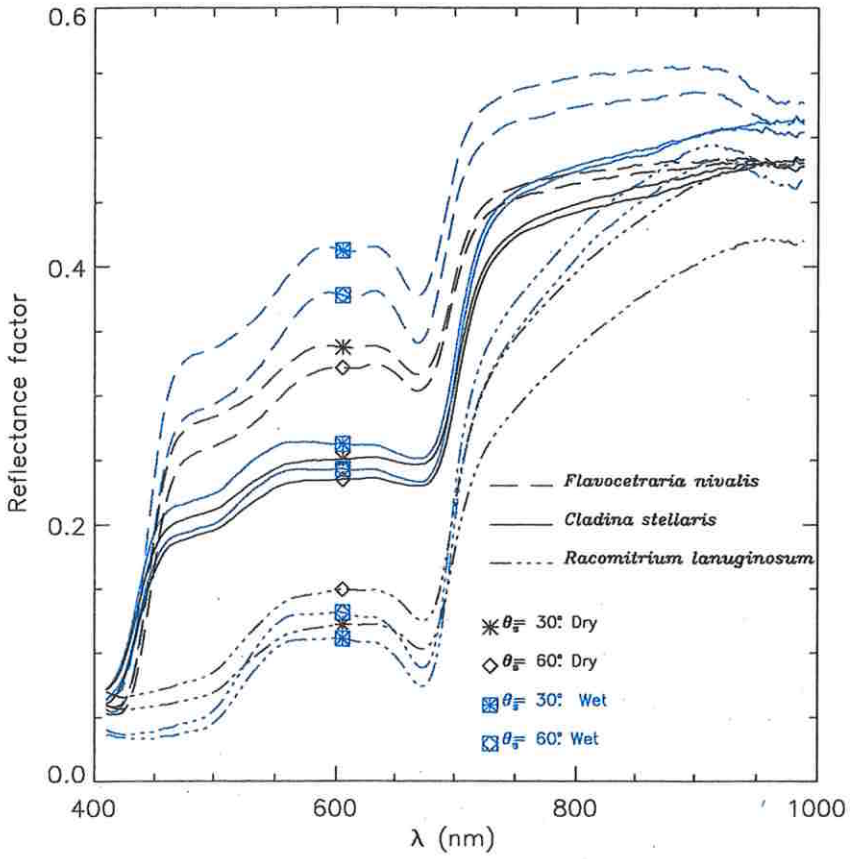

Figure 6.2: Spectral RF of the main targets in dry and wet conditions. The plot is based on measurements from position $\theta_d = 0°$, $\phi = 0°$. The target data are from Experiments 24, 25, 27, 33, 34, 36 – 39 and 41 (see Appendix B).

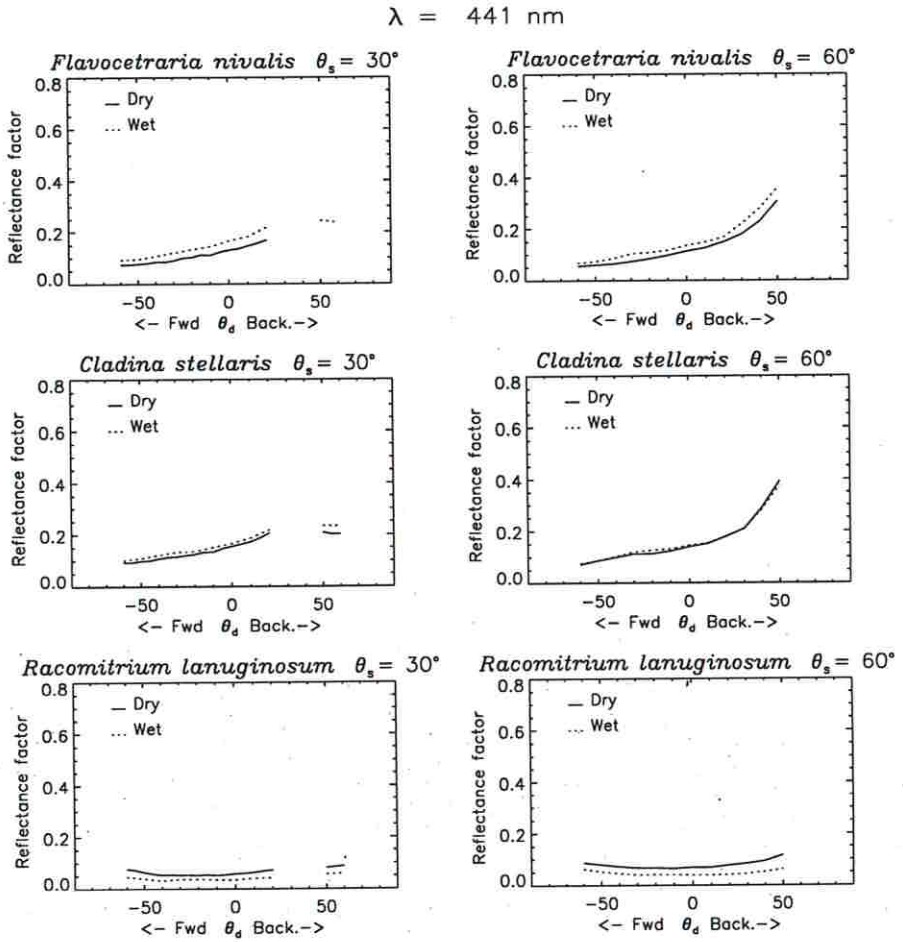

Figure 6.3: Spectral RF of the main targets in dry and wet conditions in the principal plane, for $\lambda = 441$ nm. Based on data from Experiments 24, 25, 27, 33, 34, 36 – 39, and 41 (see Appendix B).

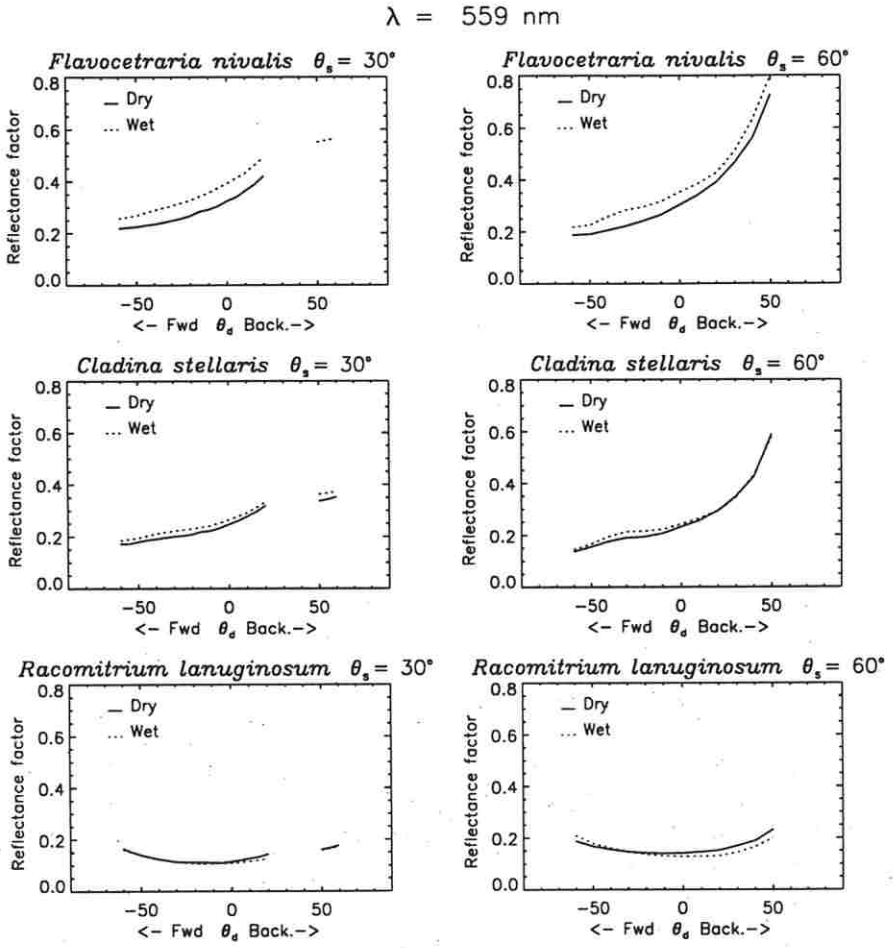

Figure 6.4: Spectral RF of the main targets in dry and wet conditions in the principal plane, for $\lambda = 559$ nm. Based on data are Experiments 24, 25, 27, 33, 34, 36 – 39, and 41 (see Appendix B).

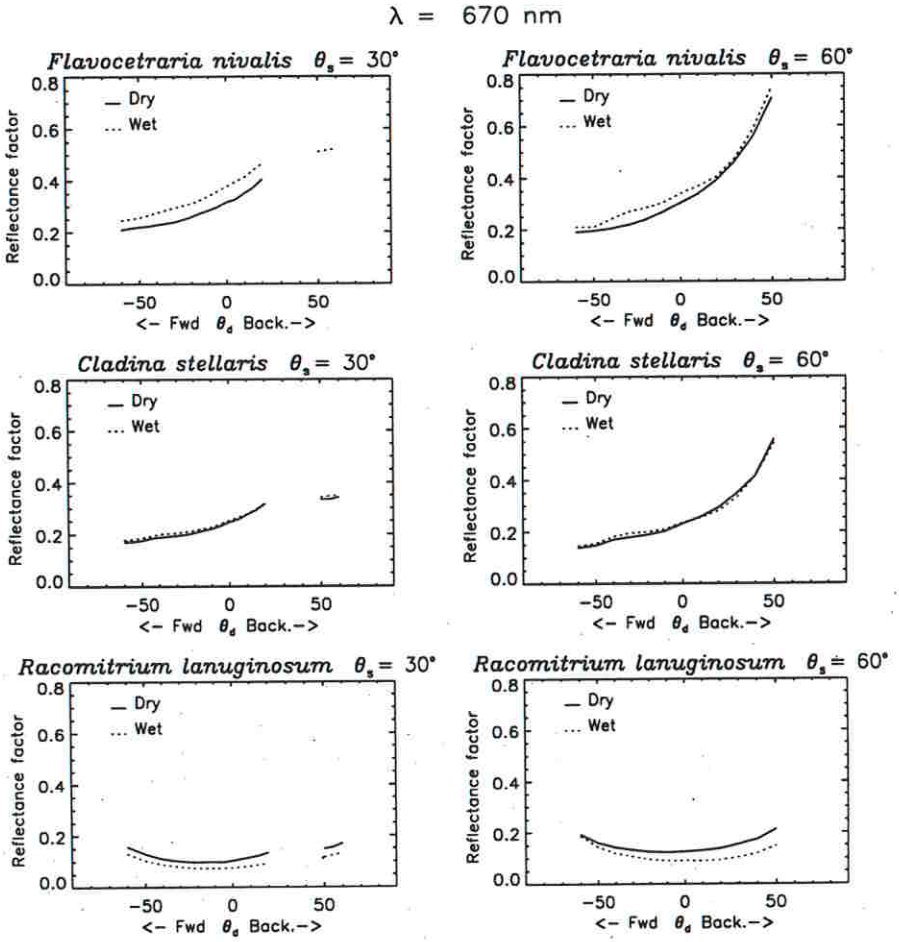

Figure 6.5: Spectral RF of the main targets in dry and wet conditions in the principal plane, for $\lambda = 670$ nm. Based on data from Experiments 24, 25, 27, 33, 34, 36 – 39, and 41 (see Appendix B).

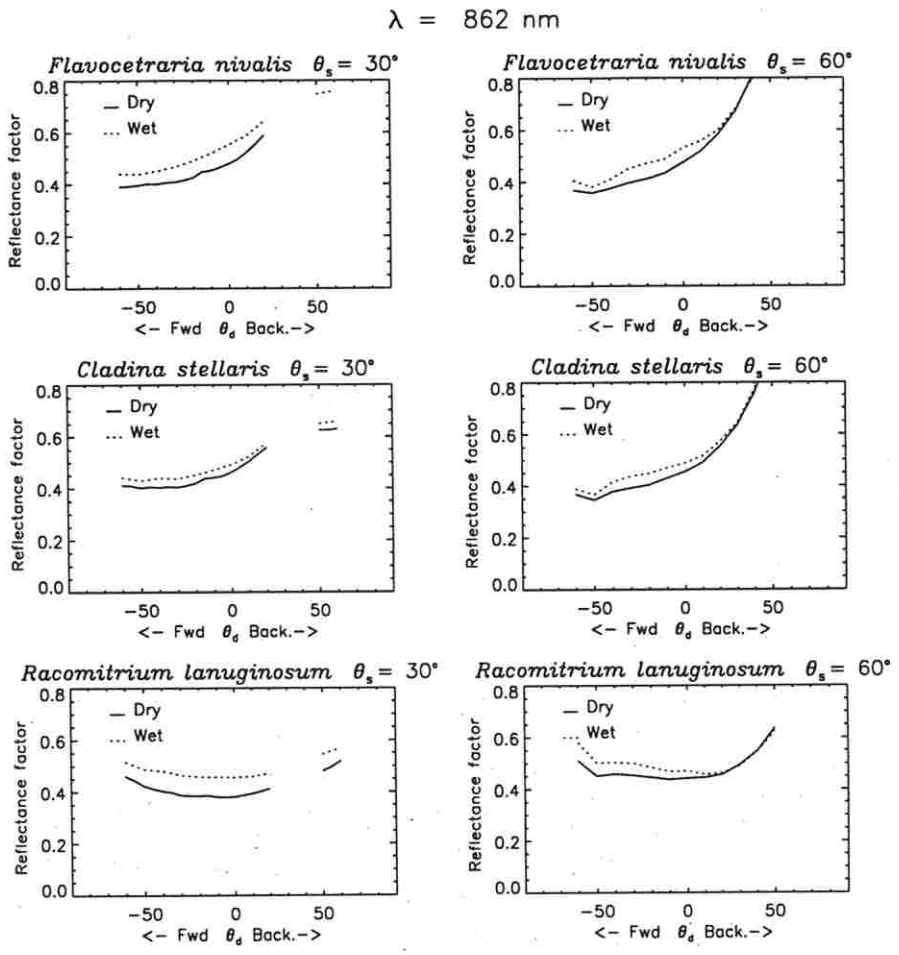

Figure 6.6: Spectral RF of the main targets in dry and wet conditions in the principal plane, for $\lambda = 862$ nm. Based on data from Experiments 24, 25, 27, 33, 34, 36 – 39, and 41 (see Appendix B).

6.3 Comparison of EGO spectral signatures with field measurements

In late June and early July 1996, we carried out a field campaign to measure the spectral reflectance of the targets in their natural habitats. We applied a SE590 spectrometer with a FOV of 15°. The spectrometer was mounted on a 1.5 m high tripod. All measurements were taken from the nadir position. The measurements were taken under clear to partly overcast cloud conditions, which gave both direct and diffuse light. A white Spectralon reference panel was used for reference measurements.

The spectra were collected near Isfjord Radio on Svalbard (70° : 3′N, 13° : 38′E), and at two different locations near Kautokeino in Finnmark, Norway (69° : 0′40″N, 23° : 6′27″E and 68° : 47′30″N, 23° : 19′20″E). The Isfjord Radio area has been classified as a northern arctic tundra zone by Elvebakk [28]. The *Salix polaris* and *Saxifraga oppositifolia* are most often dominant together with cryptograms[2]. On stable sites the vegetation cover is normally between 50% and 100%. A conspicuous lichen cover of *Cetraria delisei* is often present. Ecologically, the Kautokeino area belongs to the lichen forest in the north-boreal zone [32]. The north-boreal lichen forest is dominated by birch, alpine bearberry, black crowberry and reindeer lichens.

The solar zenith angle was in the range form 55° to 59° on Isfjord Radio and from 45° to 50° in Kautokeino. At each measurement site, homogeneous patches of the targets were first localized. For each measurement location the field of view was photographed. We then did alternate spectral measurements and reference measurements. This was repeated five times, before the area of view was slightly changed, and new measurements were acquired. The target patch was then sprinkled with water from nearby lakes or streams, and left to rest for a few minutes before measurements of the moist targets were acquired. The time of each measurement was automatically recorded. On average, it took three minutes to acquire five target and five reference spectra. In the data analysis, "outlier" target spectra were screened from the analysis. A spectrum was classified as an "outlier" if it deviated strongly from the other spectra in the same measurement series. This typically took place if there were rapid changes in the cloud cover. Other auxiliary information that was recorded at each measurement site was air and ground temperature and humidity. In Appendix B.5 we give a summary of each field data measurement in terms of the $\hat{s}_{abs}$ of the target, reference panel, and RF data. The $\hat{s}_{abs}$ were calculated before the outliers were excluded.

Figure 6.7 shows the average spectral signatures from the Kautokeino and Isfjord Radio field data. Each spectral signature is the average of all the measurements made of that particular target in the dry or the moist state. The field measurements confirms the observation made from the EGO data, that the wet

[2]Cryptograms: ferns, mosses and thallophytes (algi, fungi and lichens).

Flavocetraria nivalis and *Cladina stellaris* have a higher RF than the dry targets, whereas the opposite is the case for the *Racomitrium lanuginosum*.

During the field campaign we also measured the reflectance from common arctic vegetation. Some of the spectral RF estimates are presented in Figure 6.7. The *Cladina stygia*, *Cladina arbuscula*, *Cladina rangiferina* and *Stereocaulon paschale* are light colored mat-forming lichens, with similar canopy structure as *Cladina stellaris* and *Flavocetraria nivalis*. However, their spectral RF are lower. The wet *Cladina arbuscula* had a higher RF than the dry sample. The opposite was observed for *Cladina stygia*. The most interesting lichen measured at Isfjord Radio was the *Cetraia delisei*, a dark brown mat-forming lichen that often covers 50% or more of the tundra.

There is a surprisingly good agreement between the RF estimates of *Flavocetraria nivalis* from Kautokeino and the nadir RF estimates acquired in the EGO (*Flavocetraria nivalis* collected in Balsfjord). Figure 6.8 shows the average nadir RF for different FOV and source zenith angle, for the target in dry and wet state, based on measurements from the EGO and from field measurements.

The correlation coefficient between the wet EGO *Flavocetraria nivalis* RF estimate at FOV = 6° and $\theta_s = 60°$, and the Kautokeino RF is $\hat{r} = 0.99$, and for the Isfjord Radio RF we found $\hat{r} = 1.00$. The rms was 3.13 and 15.25 respectively. The EGO spectral RF estimates are approximately 5% lower than the Kautokeino estimates in the NIR. The spectral reflectance curve of the Svalbard *Flavocetraria nivalis* is 10% lower in the visible and 15% lower in the NIR than the lichens RF estimates from the EGO and Kautokeino. However, the high correlation shows a great similarity of the shape of the different reflectance curves.

For the dry *Flavocetraria nivalis* we first note that there is a minimal difference ($\hat{r} = 1.00, rms = 0.185$) between the EGO RF estimates acquired with FOV = 15°, and $\theta_s = \{55°, 60°\}$. The RF estimates acquired with FOV = 6° and $\theta_s = 60°$ are approximately 3% higher for ($450 < \lambda < 680$) nm, than the FOV = 15° RF estimates. The Kautokeino field RF estimates follow the EGO FOV = 15° RF estimates in the visible, but are 2.5% lower in the NIR ($\lambda > 700$ nm). The Isfjord Radio RF estimates are 6.5% lower than the Kautokeino and EGO RF estimates for $450 < \lambda < 700$ and 15 % lower in the NIR.

The standard deviation of the Finnmark *Flavocetraria nivalis* spectral RF estimates were $\hat{s} < 0.02$ for $\lambda < 450$ nm, $0.02 < \hat{s} < 0.028$ for 450 nm $< \lambda <$680 nm and $\hat{s} < 0.043$ for $\lambda > 680$ nm. For the wet *Flavocetraria nivalis* the standard deviation was 0.007, 0.022 and 0.041, respectively, for the same wavelength intervals. From this we conclude that the EGO RF estimates are within the 95% confidence interval of the field RF estimates of the same species. The standard deviation of the Svalbard RF estimates were $\hat{s} < 0.02$, for $\lambda < 680$ nm and $\hat{s} < 0.08$ for $\lambda > 680$ nm, for both the wet and the dry targets. This results indicates that the spectral signatures of the Svalbard *Flavocetraria nivalis* are significantly lower than the Kautokeino and EGO estimates. This is a reasonable result, since Svalbard has a much colder and dryer environment than most of

the mainland of Norway. Plants on Svalbard take up less water, since they risk frequent freezing, even in the summertime. As shown, a dryer vegetation will give a lower reflectance in the NIR. Gauslaa [35] argues that in cold areas a higher infrared absorption will increase leaf temperatures and possibly enhance the survival capability. In the visible, the plants may be adjusted to a lower irradiation, and the pigments may therefore absorb more.

The wet *Cladina stellaris* measured in the field (Figure 6.8) had a significantly higher RF than the EGO *Cladina stellaris* RF estimate. The correlation and rms were estimated to $\hat{r} = 0.99$ and $rms = 6.5$. The standard deviation of the field RF estimates was $\hat{s} < 0.013$ for $\lambda < 450$ nm, $0.013 < \hat{s} < 0.021$ for $450 < \lambda < 680$ nm and $\hat{s} < 0.028$ for $\lambda > 680$ nm.

For the dry *Cladina stellaris* measured in the EGO with a FOV = 6° and FOV = 15°, the correlation factor was estimated to $\hat{r} = 1.00$ and the $rms = 2.41$. The dry *Cladina stellaris* measured in Kautokeino follows the FOV = 15° EGO RF estimates for $\lambda < 680$ nm ($rms = 0.99$), whereas for $\lambda > 680$ nm the field RF estimates were approximately 10% lower than the EGO estimates, which gave an $rms = 10.48$ for that wavelength interval. The standard deviation of the dry field RF estimates was $\hat{s} < 0.01$ for all wavelengths.

The *Cladina stellaris* measured in the EGO was collected in Østerdalen in southern Norway. The lichens in Østerdalen cover the floor of a pine forest. The field measurements in Kautokeino were done in an open landscape of moss, lichens and shrubs. The field area in Kautokeino was grazed and tramped by reindeer, and the lichen cover was only 2 cm deep, whereas the samples used in the EGO were up to 15 cm deep. The *Racomitrium lanuginosum* (see Figure 6.9) measured at Isfjord Radio exhibits a slightly different spectral shape than the EGO measurements of moss collected in Tromsø. The moss measured in the field appeared fresher and less grey than the moss measured in the EGO. There may well be a physiological difference between the moss at mainland Norway and Svalbard. The moss used for the EGO campaign was kept in a phytochamber with correct light, temperature and humidity conditions in the periods between measurements. However, the moss might have suffered from severe stress during the packing and transport. The stress might have damaged or altered its physiological state, like pigments and chlorophyll content.

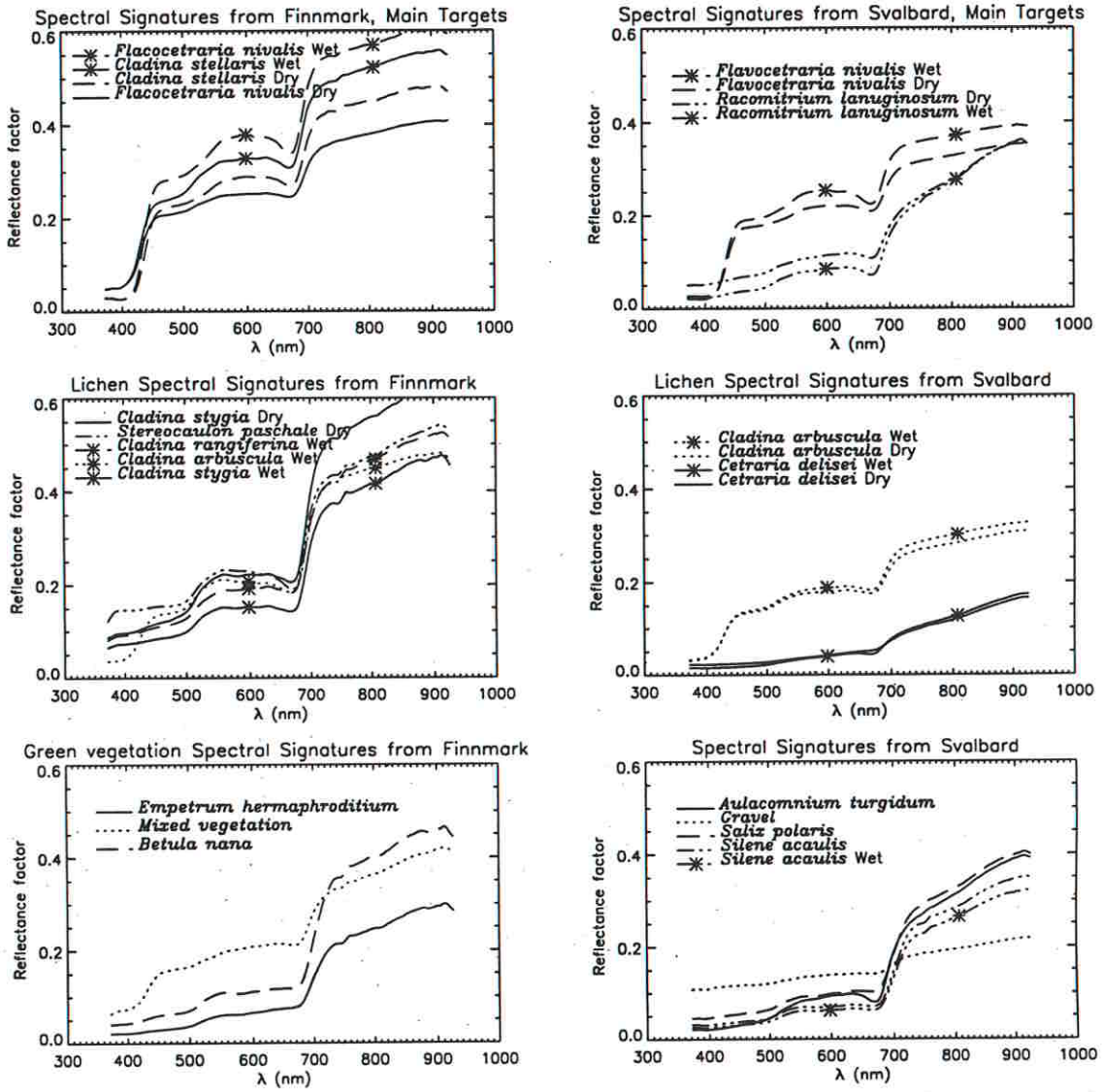

Figure 6.7: SE590 Spectral signatures acquired during a field campaign in Kautokeino, Finnmark, and on Isfjord Radio, Svalbard, July 1996.

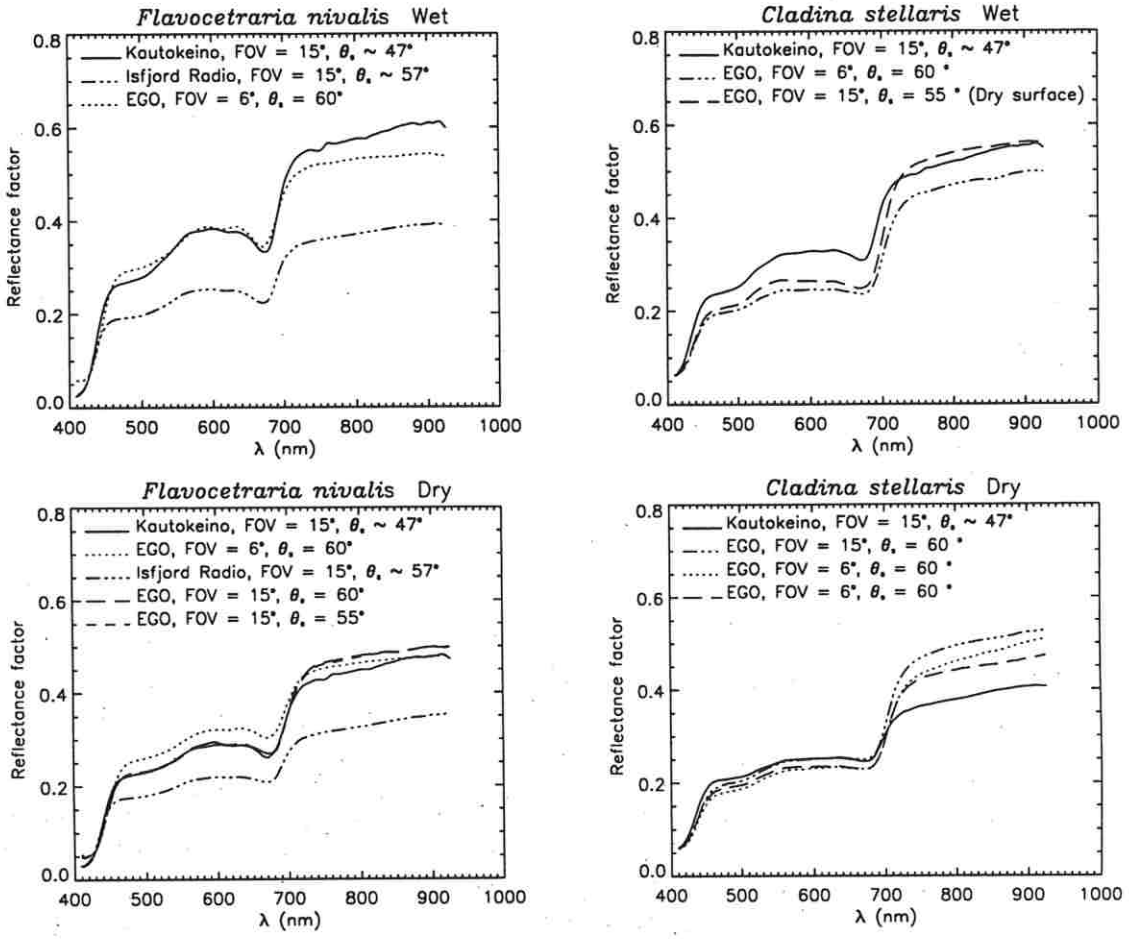

Figure 6.8: SE590 Spectral signatures acquired during the field campaign in Kautokeino, Finnmark, and on Isfjord Radio, Svalbard, July 1996, as well as the nadir RF estimates acquired from the EGO data. EGO data from Experiments 9, 10, 12, 19, 22, 23, 26, 38, 39, 40 and 41 (see Appendix B).

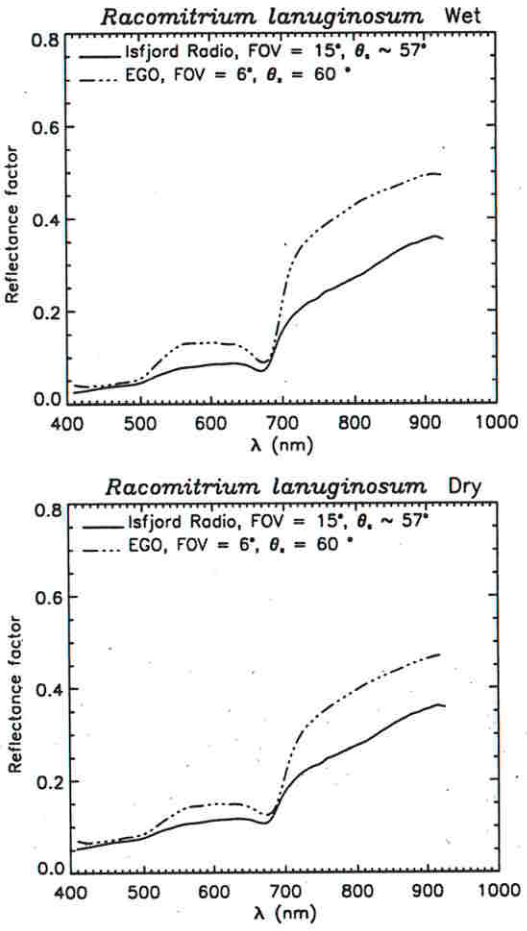

Figure 6.9: SE590 Spectral signatures acquired during the field campaign at Isfjord Radio, Svalbard and the nadir RF estimates acquired from the EGO data. EGO data from Experiments 28, 34 and 35 (see Appendix B).

Chapter 7

Measured and Modelled BRF Distributions of the Targets

In this chapter we present the estimated target BRF's obtained from our experimental data. We use the resulting BRF estimates to invert a parametrical [30] and a physical [105] BRF model. Furthermore, we evaluate the accuracy of the model parameters and use them to simulate the BRF's of the target. The simulated BRF's are in turn used to evaluate the ability of the models to reconstruct the BRF's. The target data we have used in this chapter are from Experiments 23 to 28 in Appendix B. We estimated the BRF's presented in this chapter by means of Eq. (4.1) with intensity drift corrected by means of Eq. (5.4).

To evaluate the performance of a model (the model's ability to predict a measurement), the model should be tested on different experimental data than those used for the inversion. The reason for this is that we are not primarily interested in how well the model can represent the inversion data, but how well it can predict and represent the complete BRF of a target. The data used for inversion will hereafter be called "inversion data" whereas the data used for testing and validation will be named "test data". Such a procedure is commonly referred to as cross-validation in the literature [10, 88].

As the evaluation criterion for the BRF models, we have selected the rms, which is estimated as

$$rms = \sqrt{\frac{\sum_{i=1}^{I}(\hat{\rho}_{t_i} - \hat{\rho}_{s_i})^2}{I}} \tag{7.1}$$

where $\hat{\rho}_t$ is the RF estimated based on EGO measurements, $\hat{\rho}_s$ is the resulting RF after inversion of the model, and I is the total number of reflectance factors used in the inversion. Another useful evaluation criterion is the correlation $\hat{r}(\hat{\rho}_{t_i}, \hat{\rho}_{s_i})$ defined in Eq. (2.30). The third evaluation criterion used in this chapter is the normalized root mean square error estimated as

$$rmsn = 100\frac{rms}{\bar{\rho}} \tag{7.2}$$

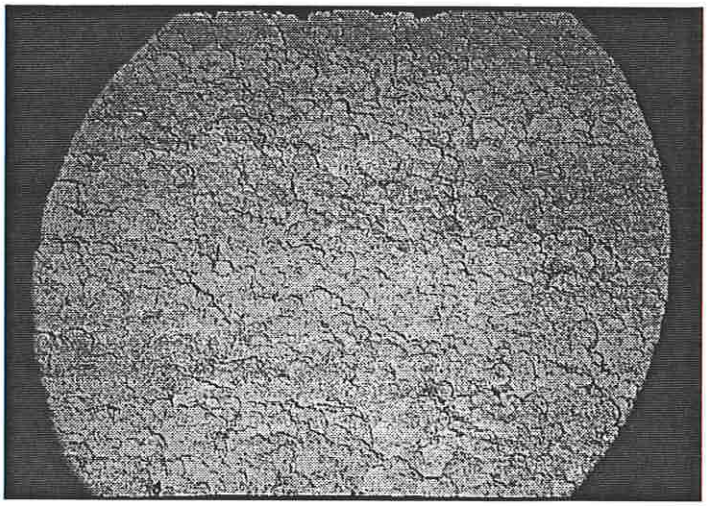

Figure 7.1: Back scattering of *Cladina stellaris*, source zenith angle $\theta_s = 60°$, photographed at relative azimuth angle $\phi = 0°$

where $\bar{\rho}$ is the average RF.

7.1 Experimental estimates of BRF distributions

The lichens represent a strongly backscattering medium. They are porous, and sparsely packed with voids between the randomly oriented scattering elements. The moss is densely packed, and has little internal shadowing. Figures 7.1, 7.2 and 7.3 shows the *Cladina stellaris* target photographed with an illumination zenith angle of 60° in the EGO system. The photograph shown in Figure 7.1 is taken in the backscattering direction, whereas the photographs shown in Figures 7.2 and 7.3 are taken in the forward scattering direction and in the cross plane, respectively.

In Figures 7.4 to 7.6 we show the estimated BRF distributions of the main targets. The estimates are based on experimental EGO data, for source angles $\theta_s = \{30°, 60°\}$, for the three different wavelengths $\lambda = \{441, 670, 861\}$ nm. The minimum, maximum, average and standard deviation for the RF's are given in Table 7.1, and commented below in the remaining of this section.

For $\lambda = 441$ nm (Figure 7.4) and $\theta_s = 30°$, all the investigated targets scatter fairly isotropically, with the exception of a small hot spot for the lichens. The peak value of the hot spot (the max RF value for the lichens in Table 7.1) lies 0.1 above the average BRF value. For $\theta_s = 60°$ the lichens have a hot spot in the back scattering direction. The peak RF values for the *Flavocetraria nivalis* is 0.3 above the average BRF value, and for the *Cladina stellaris* it is 0.4 above.

For $\lambda = \{559, 670\}$ nm (Figure 7.5) and $\theta_s = 30°$, both lichen BRF distributions have a hot spot and a hollow depression in the forward scattering direction.

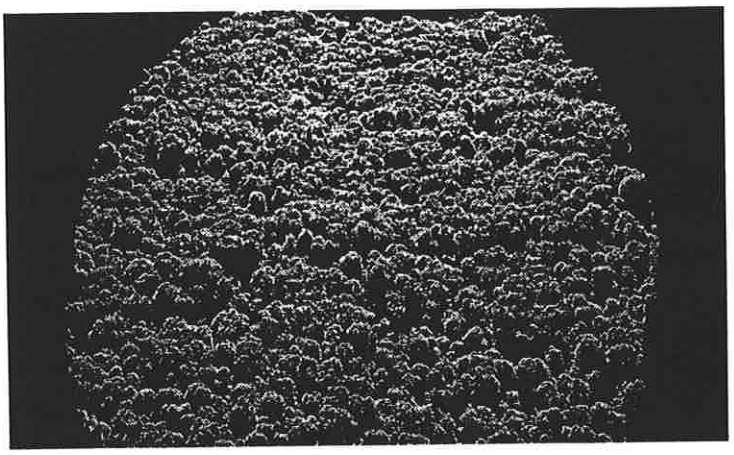

Figure 7.2: Forward scattering of *Cladina stellaris*, source zenith angle $\theta_s = 60°$, photographed at relative azimuth angle $\phi = 180°$

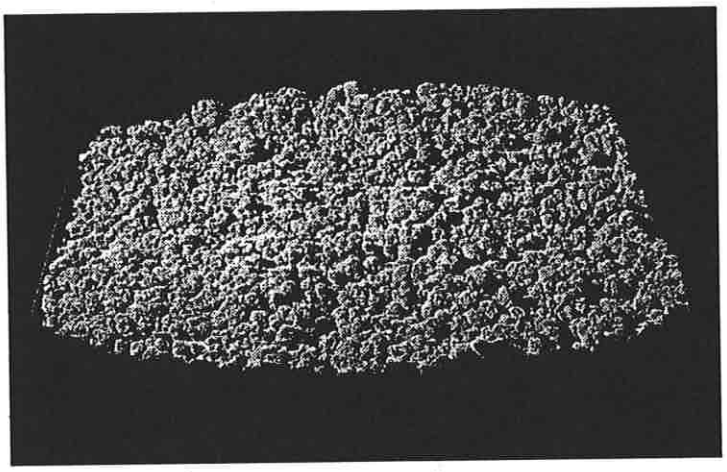

Figure 7.3: Cross plane of *Cladina stellaris*, source zenith angle $\theta_s = 60°$, photographed at relative azimuth angle $\phi = 90°$

The difference between the maximum value and the average BRF value is here 0.21 for the *Flavocetraria nivalis* and 0.17 for the *Cladina stellaris*. The BRF distribution of the moss is fairly flat for $\theta_s = 30°$, with the exception of a small specular peak in the forward scattering direction, and a small hot spot. The difference between the average and the maximum value is here 0.09. For source zenith $\theta_s = 60°$ the BRF distributions of the two lichens display a prominent hot spot effect. The peak values are now 0.67 and 0.52 higher than the average BRF value for the *Flavocetraria nivalis* and the *Cladina stellaris* respectively. The lichens also exhibit a depression in the forward scattering direction. The moss BRF distribution has a hot spot region, but this sector has a much lower reflectance level than that of the lichens. The level of the hot spot is only 0.15 higher than the average value.

Table 7.1: The minimum, maximum and average spectral RF values for the main targets.

Target	$\theta_s = 30°$ $min(\hat{\rho})$	$max(\hat{\rho})$	$\overline{\hat{\rho}}$	$s(\hat{\rho})$	$\theta_s = 60°$ $min(\hat{\rho})$	$max(\hat{\rho})$	$\overline{\hat{\rho}}$	$s(\hat{\rho})$
Flavocetraria nivalis								
441 nm	0.06	0.22	0.13	0.04	0.03	0.46	0.14	0.08
559 nm	0.19	0.53	0.32	0.08	0.10	1.01	0.34	0.16
670 nm	0.19	0.52	0.31	0.08	0.10	1.00	0.33	0.16
861 nm	0.35	0.77	0.50	0.10	0.18	1.39	0.54	0.20
Cladina stellaris								
441 nm	0.07	0.25	0.15	0.04	0.03	0.57	0.15	0.09
559 nm	0.14	0.41	0.25	0.06	0.06	0.82	0.26	0.13
670 nm	0.16	0.42	0.25	0.06	0.07	0.78	0.26	0.13
861 nm	0.33	0.76	0.48	0.09	0.16	1.26	0.53	0.19
Racomitrium lanuginosum								
441 nm	0.05	0.12	0.07	0.01	0.06	0.17	0.08	0.02
559 nm	0.11	0.22	0.13	0.02	0.10	0.33	0.16	0.04
670 nm	0.09	0.20	0.12	0.02	0.09	0.31	0.15	0.04
861 nm	0.37	0.62	0.42	0.05	0.21	0.91	0.46	0.09

For the NIR wavelength, $\lambda = 861$ nm (Figure 7.6) the BRF distributions for all three targets show hot spots for both $\theta_s = 30°$ and 60°. The hot spots are wider than in the visible range, due to the multiple scattering within the targets at this wavelength. The RF for the *Flavocetraria nivalis* BRF distribution reaches a maximum of 1.39 in the back scattering direction, which is 0.85 higher than the average BRF value, and 1.21 higher than the minimum value. The maximum value for the *Cladina stellaris* is here 0.73 higher than the average. The *Racomitrium lanuginosum* hot spot is 0.45 higher than the average BRF value.

To summarize the above description, both lichen species exhibit very strong direction dependent reflection properties. For $\lambda = 440$ nm, the *Cladina stellaris* has a more pronounced hot spot than the *Flavocetraria nivalis*. The opposite is the case for the other investigated wavelengths. The moss showed very weak angular dependent reflection properties for the visible wavelengths, but at the NIR wavelength, it had a very pronounced back-scattering component.

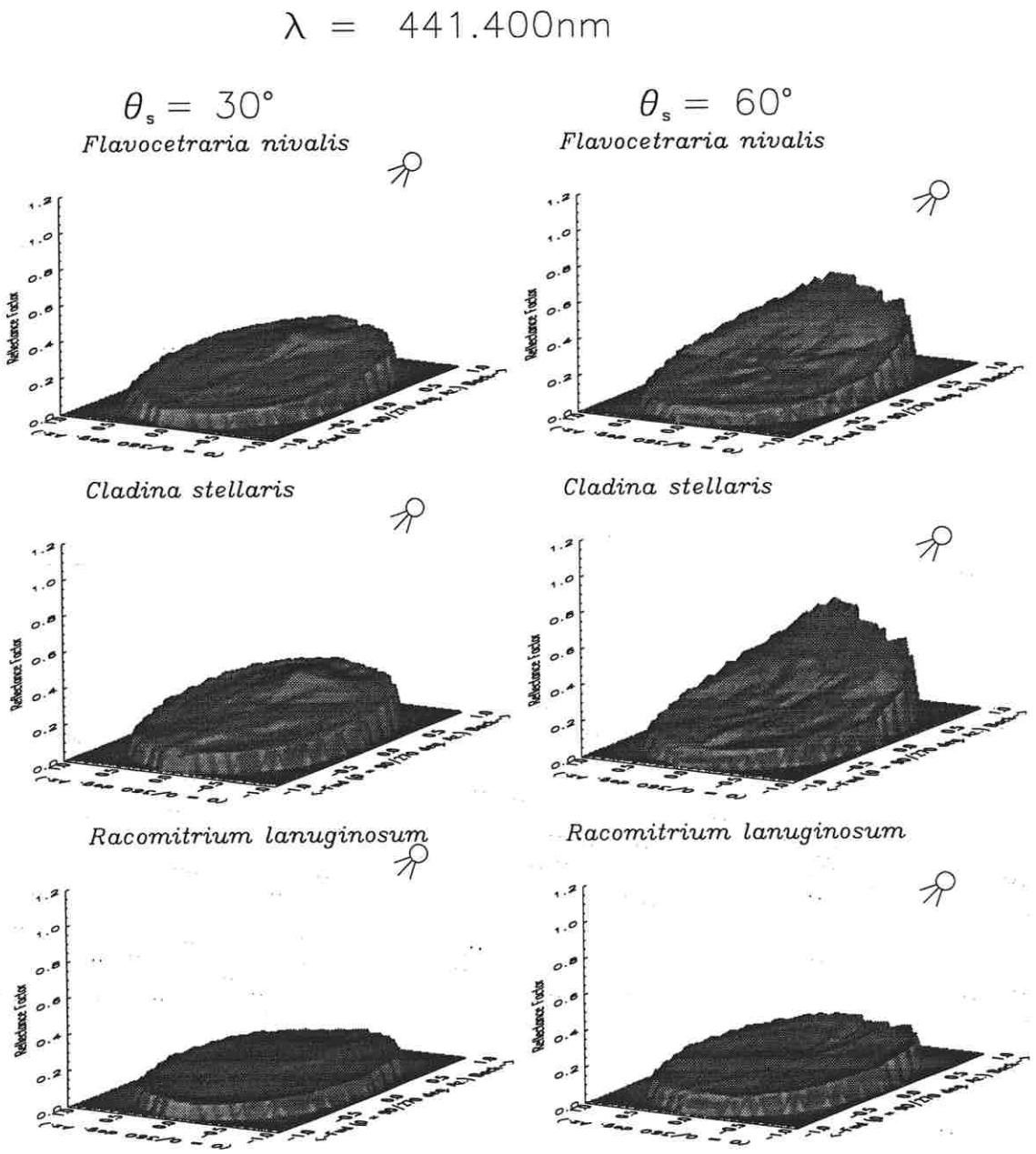

Figure 7.4: BRF plots of the main targets at 441 nm. The left hand column is for source zenith angle $\theta_s = 30°$, and the right hand column is for $\theta_s = 60°$.

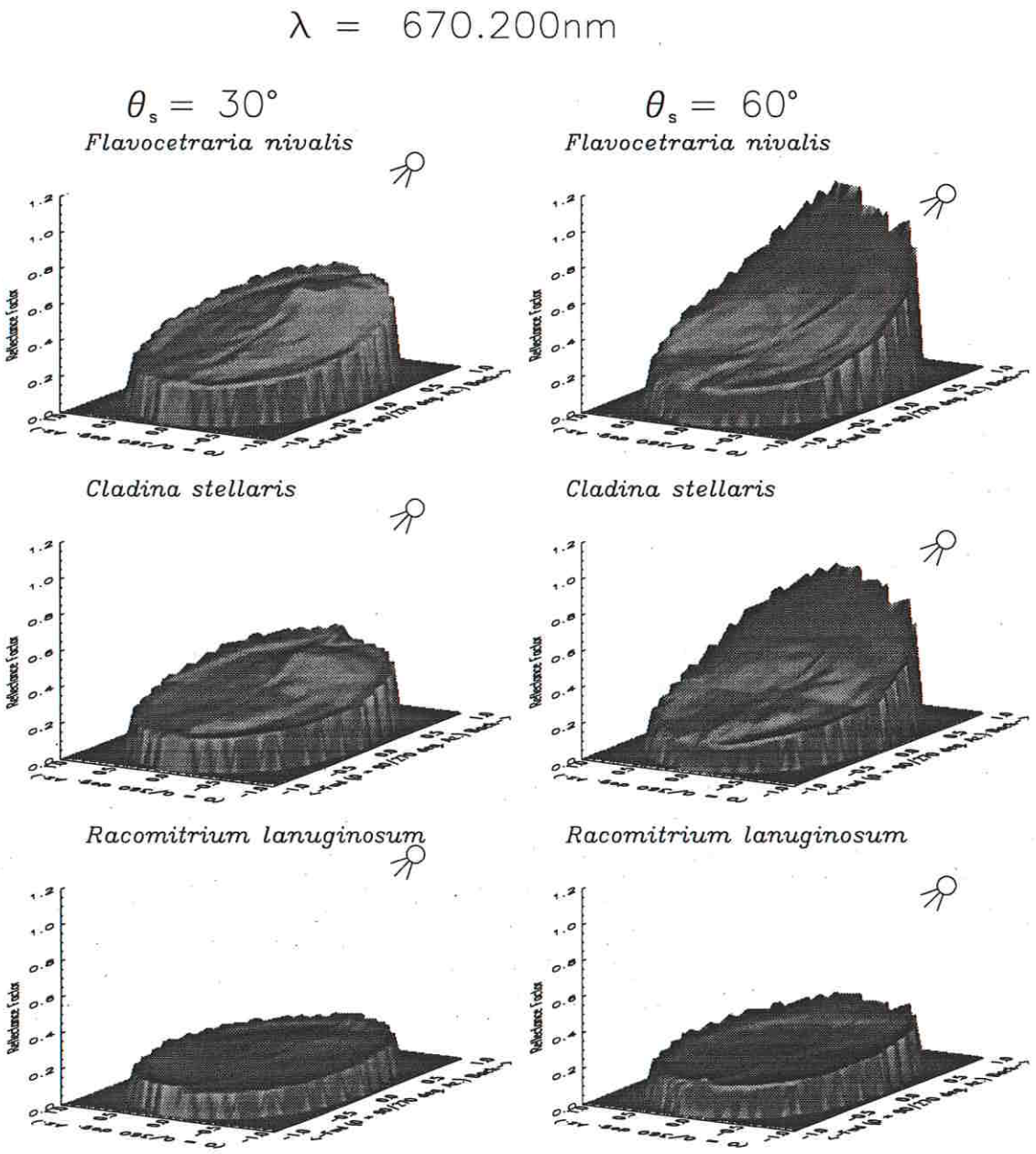

Figure 7.5: BRF plots of the main targets at 670 nm. The left hand column is for source zenith angle $\theta_s = 30°$, and the right hand column is for $\theta_s = 60°$.

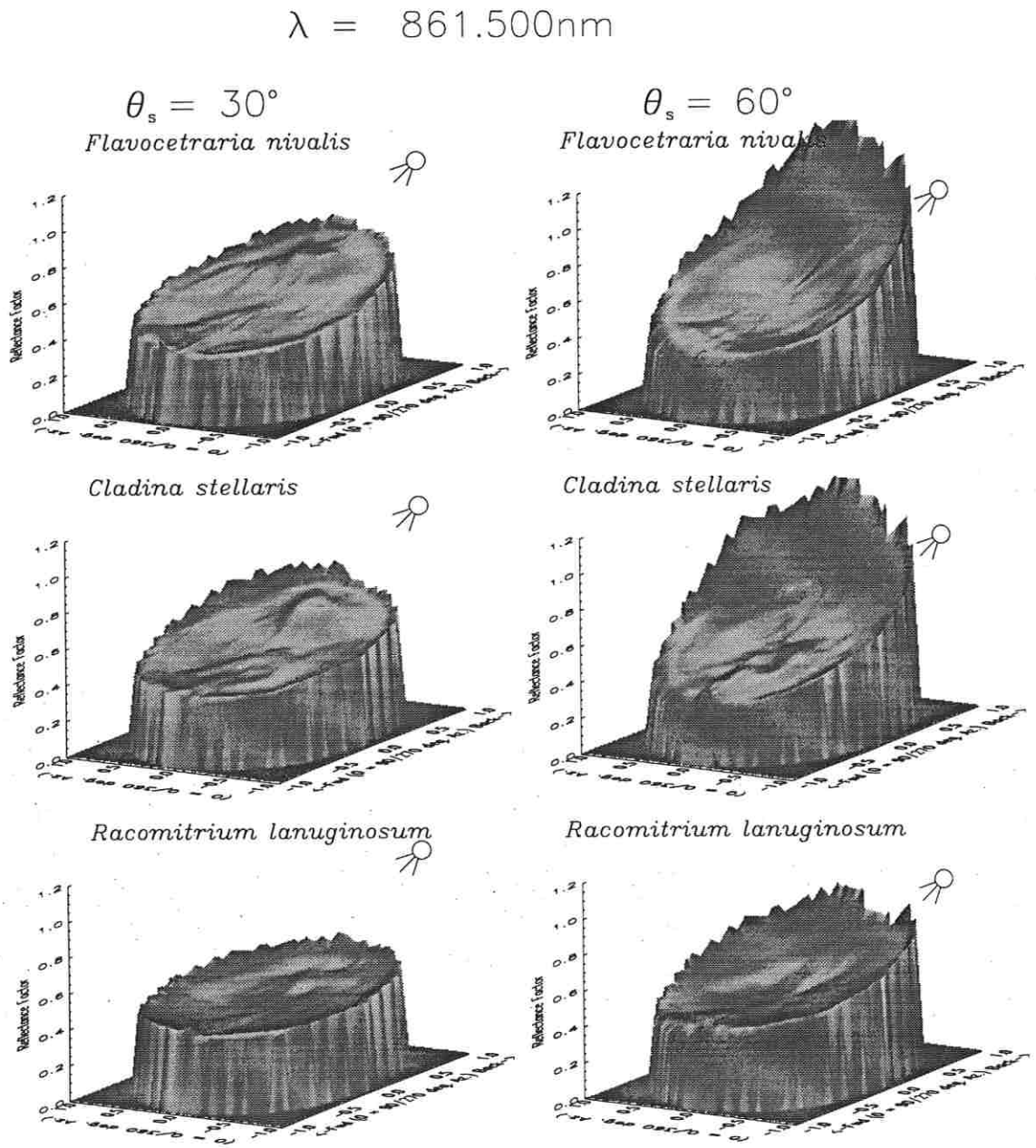

Figure 7.6: BRF plots of the main targets at 861 nm. The left hand column is for source zenith angle $\theta_s = 30°$, and the right hand column is for $\theta_s = 60°$.

7.2 A parametric BRF model of the data

To model the BRF of the main targets we chose to use the parametric bidirectional reflectance model reviewed in section 2.4. The EMRPV1 [30, 29] model is a parametric model whose true value of the parameters are unknown. The parameters are estimated based on a finite number of available samples. However, the parameter estimates are random variables and vary around the expected values. In this section we describe the statistical properties of the estimated model parameters. Next, we investigate how the output of the EMRPV1 model is influenced by random variations of the parameters. We then evaluate the capability of the model to predict the BRF's of the investigated targets.

7.2.1 Evaluation of the EMRPV1 model

The model performance was evaluated as a function of the number of BRF estimates used for each inversion[1]. This was done in order to determine the necessary number of inversion data samples needed in order to estimate the EMRPV1 model parameters. We used the cross-validation inversion procedure described in detail in Section 2.6.1. The samples used for inversion were first selected randomly from the RF's estimated for a particular target, the remaining RF's were used as test data. The cross-validation inversion procedure was repeated for evenly sampled data.

The resulting normalized *rms* error, $\overline{rmsn}$ is plotted against the number of inversion samples in Figure 7.7. The figure presents the $\overline{rmsn}$ for the inversion and test errors, and their $\alpha = 0.025$ confidence intervals. The number of samples in the test set is $I_{test} = I - I_{inversion}$, where I is the total number of available samples, and $I_{inversion}$ is the number of samples in the inversion set. The evaluation statistics are summarized in Table A.5 in Appendix A. The performance statistics were estimated based on separate inversions for each of the three targets, for each of the four test wavelengths. This was repeated five times for each of the selected number of inversion samples. Thus, each point in the plot shown in Figure 7.7 and each line in Table A.5 is based on 60 inversions. Since the number of inversions is large, by virtue of the central limit theorem (i.e [8]) the $\overline{rmsn}$ can be treated as a normal variable. Based on the confidence intervals presented in Figure 7.7 and Table A.5 we conclude that:

- When 125 or more randomly or evenly selected samples are used for the inversion, with 95% confidence the *rmsn* from the inversion and test are equal.
- The test equilibrium normalized *rms* error, $\overline{rmsn}$ is found to be approximately 6.4%.

[1] We used the EMRPV1 inversion code developed by Engelsen *et al.* [30, 29]

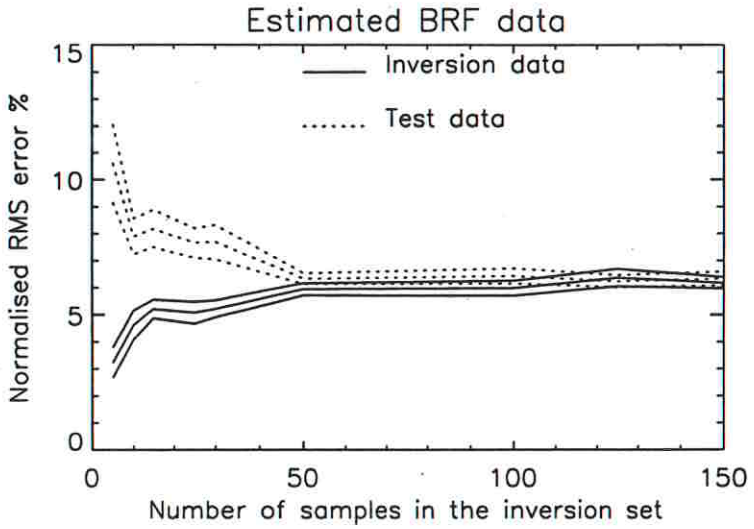

Figure 7.7: The average $\overline{rmsn}$ inversion error and its $\alpha = 0.025$ confidence interval, as a function of the number of samples used for inversion. Each point in the plot is the sample estimate of 60 inversions of evenly drawn experimental data.

In order to evaluate the number of samples that are necessary for the inversion of the EMRPV1 model on noise free data, we used the parameters resulting from the EMRPV1 inversions to simulate a new data set. The randomly selected samples from the simulated data sets for all three targets, and the four test wavelengths were then used to invert the EMRPV1 model using the same procedure as above. The results are listed in Table A.6 in Appendix A. The procedure was repeated for evenly sampled data. Figure 7.8 shows the resulting $\overline{rmsn}$ for the inversion and test errors as functions of the number of samples used for inversion, as well as their 95% confidence intervals. The results show that:

- When 25 or more randomly drawn samples, or 30 or more evenly drawn samples are used for the inversion, with 95% confidence the $rmsn$ from the inversion and test are equal.
- When 30 or more randomly or more evenly drawn samples are used for the inversion, the test $\overline{rmsn}$ stabilizes to approximately 0.06%. This can be regarded as an estimate of the modelling error.

7.2.2 Inversion of the EMRPV1 model

We used the EMRPV1 model to model our BRF data from the EGO experiments. In the above analysis we found that 125 or more randomly selected samples from the BRF estimates based on the measurement should be used to invert the

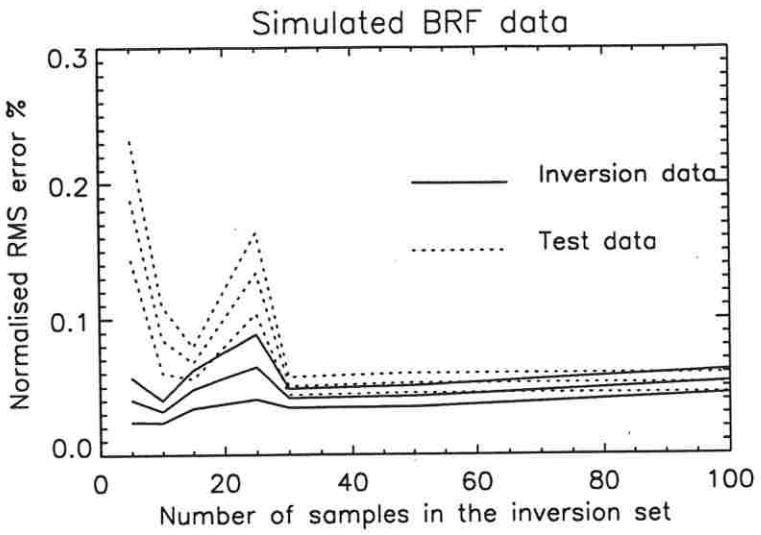

Figure 7.8: The average $\overline{rmsn}$ inversion error and its $\alpha = 0.025$ confidence interval, as a function of the number of samples used for inversion. Each point in the plot is the sample estimate of 60 inversions of evenly drawn simulated data.

data. We decided to use 150 randomly selected samples for the inversion. To estimate the model parameters and model statistics, 250 inversions were carried out for each target and wavelength, following the bootstrap procedure outlined in Section 2.6.1. The large number of inversions were carried out to ensure that the estimates of the parameters could be approximated by normal distributions. The resulting parameter estimates for the three targets and the four selected wavelengths, are listed in Table 7.2. By estimating the confidence intervals for each of the model parameters for each target and wavelength, we found that all of the parameters are separable at the $\alpha = 0.025$ confidence level.

The inversion and test errors and correlation are shown in Table 7.3. The correlation coefficient ($\hat{r}$) between the inversion (or test) data and the corresponding EMRPV1 model results was $0.97 < \hat{r} < 0.99$ for the lichen targets. For the moss, the correlation was $0.90 < \hat{r} < 0.95$. The slightly worse result for the *Racomitrium lanuginosum* can be explained by the specular peak and other local bumps in the BRF. Table A.7 in Appendix A, shows the parameter estimates and rms errors from inversion of the EMRPV1 model on all available data. As expected, the estimated parameters are very close to the average parameter estimates resulting from the bootstrap procedure, presented in Table 7.2. In fact, the maximum difference between the bootstrap estimate and the estimates based on on inversion on all available parameters is less than 0.0032 for all four parameters.

In Figure 7.9 to 7.11 we show the BRF's of the main targets as modelled by the EMRPV1 model, for $\lambda = 670$ nm. The modelled BRF is plotted together with the EGO based BRF, as well as the error between the EGO BRF and

Table 7.2: The estimated EMRPV1 model parameters.

Target	wavelength	$\hat{\bar{\rho}}_0$ $s(\rho_0)$	$\hat{b}$ $s(b)$	$\hat{k}$ $s(k)$	$\hat{\bar{\rho}}$ $s(\bar{\rho})$
C. stellaris	441	0.1786 0.0026	-0.6966 0.0162	0.6239 0.0141	0.1528 0.0046
F. nivalis	441	0.1620 0.0026	-0.7864 0.0166	0.5585 0.0117	0.1315 0.0044
R. lanuginosum	441	0.0493 0.0006	-0.1043 0.0130	0.5205 0.0125	0.0729 0.0013
C. stellaris	553	0.2809 0.0038	-0.6031 0.0148	0.6235 0.0115	0.2494 0.0072
F. nivalis	553	0.3900 0.0046	-0.6480 0.0119	0.6120 0.0086	0.3236 0.0081
R. lanuginosum	553	0.0957 0.0010	-0.0789 0.0111	0.5720 0.0112	0.1397 0.0022
C. stellaris	670	0.2814 0.0037	-0.5918 0.0145	0.6179 0.0109	0.2516 0.0061
F. nivalis	670	0.3834 0.0045	-0.6334 0.0124	0.6119 0.0090	0.3244 0.0089
R. lanuginosum	670	0.0898 0.0011	-0.0885 0.0128	0.5504 0.0121	0.1312 0.0024
C. stellaris	861	0.5252 0.0068	-0.3990 0.0134	0.6576 0.0095	0.4977 0.0096
F. nivalis	861	0.5707 0.0065	-0.4571 0.0109	0.6402 0.0074	0.5122 0.0102
R. lanuginosum	861	0.3466 0.0036	-0.0823 0.0103	0.7257 0.0093	0.4351 0.0046

EMRPV1 BRF. In general, the EMRPV1 model predicted a higher and more pronounced hot spot than what we measured for the lichens, for $\theta_s = \{10°, 30°\}$. For $\theta_s = 60°$ the predicted hot spot fits well for *Flavocetraria nivalis* (Figure 7.9), but is predicted to be too narrow for the *Cladina stellaris* (Figure 7.10). For the moss, the EMRPV1 model does not capture the specular peak and other local bumps (Figure 7.11).

In Figure 7.12 and 7.13 we show the RF estimates based on the EGO measurements, and the RF predicted by the EMRPV1 model for the *Cladina stellaris* and *Racomitrium lanuginosum* targets, at $\lambda = 670$ nm in the principal plane. For the *Cladina stellaris*, the EMRPV1 model shows an excellent fit for $\theta_s = \{30°, 60°\}$ (Figure 7.12). For $\theta_s = 10°$, we might suspect that the EMRPV1 model predicts a small hot spot, which is not present in the data material (Figure 7.12). However

Table 7.3: The inversion and test errors for the EMRPV1 model. The correlation ($\hat{r}$) is between the data used for inversion and inversion results

Target	wavelength	$\overline{rms}$	$s(rms)$	$\hat{r}$	$s(\hat{r})$	$\overline{rmsn}$ %	$s(\overline{rmsn})$ %
C. stellaris	441	0.0112	0.0011	0.9820	0.0038	7.30	0.69
test	441	0.0117	0.0008	0.9809	0.0021	7.64	0.68
F. nivalis	441	0.0102	0.0007	0.9836	0.0034	7.80	0.52
test	441	0.0106	0.0007	0.9830	0.0016	8.09	0.70
R. lanuginosum	441	0.0048	0.0004	0.9535	0.0099	6.58	0.48
test	441	0.0050	0.0002	0.9533	0.0029	6.83	0.37
C. stellaris	553	0.0149	0.0013	0.9836	0.0040	6.00	0.53
test	553	0.0155	0.0009	0.9838	0.0016	6.22	0.51
F. nivalis	553	0.0184	0.0015	0.9863	0.0031	5.70	0.49
test	553	0.0191	0.0010	0.9862	0.0013	5.91	0.39
R. lanuginosum	553	0.0091	0.0007	0.9436	0.0136	6.49	0.48
test	553	0.0094	0.0003	0.9438	0.0042	6.70	0.25
C. stellaris	670	0.0144	0.0011	0.9847	0.0037	5.73	0.48
test	670	0.0150	0.0008	0.9843	0.0017	5.99	0.41
F. nivalis	670	0.0180	0.0013	0.9868	0.0029	5.55	0.43
test	670	0.0186	0.0009	0.9861	0.0012	5.74	0.38
R. lanuginosum	670	0.0085	0.0007	0.9493	0.0121	6.45	0.47
test	670	0.0088	0.0003	0.9491	0.0037	6.71	0.31
C. stellaris	861	0.0265	0.0020	0.9737	0.0060	5.33	0.42
test	861	0.0276	0.0009	0.9736	0.0018	5.55	0.25
F. nivalis	861	0.0234	0.0016	0.9836	0.0038	4.56	0.31
test	861	0.0243	0.0007	0.9838	0.0011	4.75	0.20
R. lanuginosum	861	0.0235	0.0017	0.9094	0.0230	5.41	0.39
test	861	0.0239	0.0006	0.9123	0.0061	5.50	0.17

since the BRF measurements for $\theta_s = 10°$ are sparse, we are not confident about the true shape of the BRF for this case. The *Racomitrium lanuginosum* predictions (Figure 7.13) lacks a tight fit in the backscattering direction. We also clearly see that the EMRPV1 model is unable to model the specular component in the forward directions.

To conclude: the EMRPV1 model gives stable and reliable inversion results when sufficient data is used for the inversion. It is well suited to model BRF distributions with pronounced hot spots.

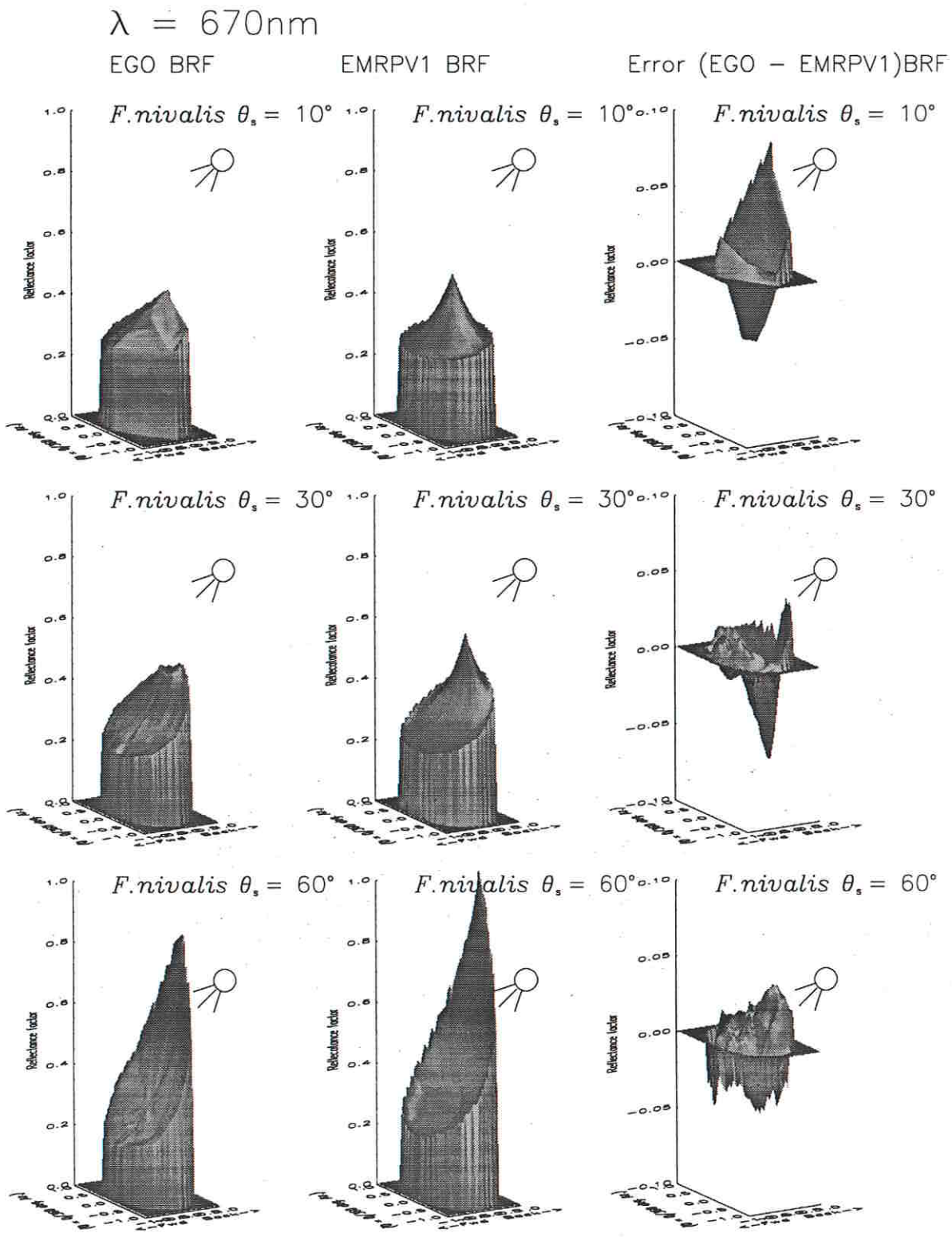

Figure 7.9: The BRF estimated based on EGO data and the predicted EMRPV1 BRF's for *Flavocetraria nivalis*.

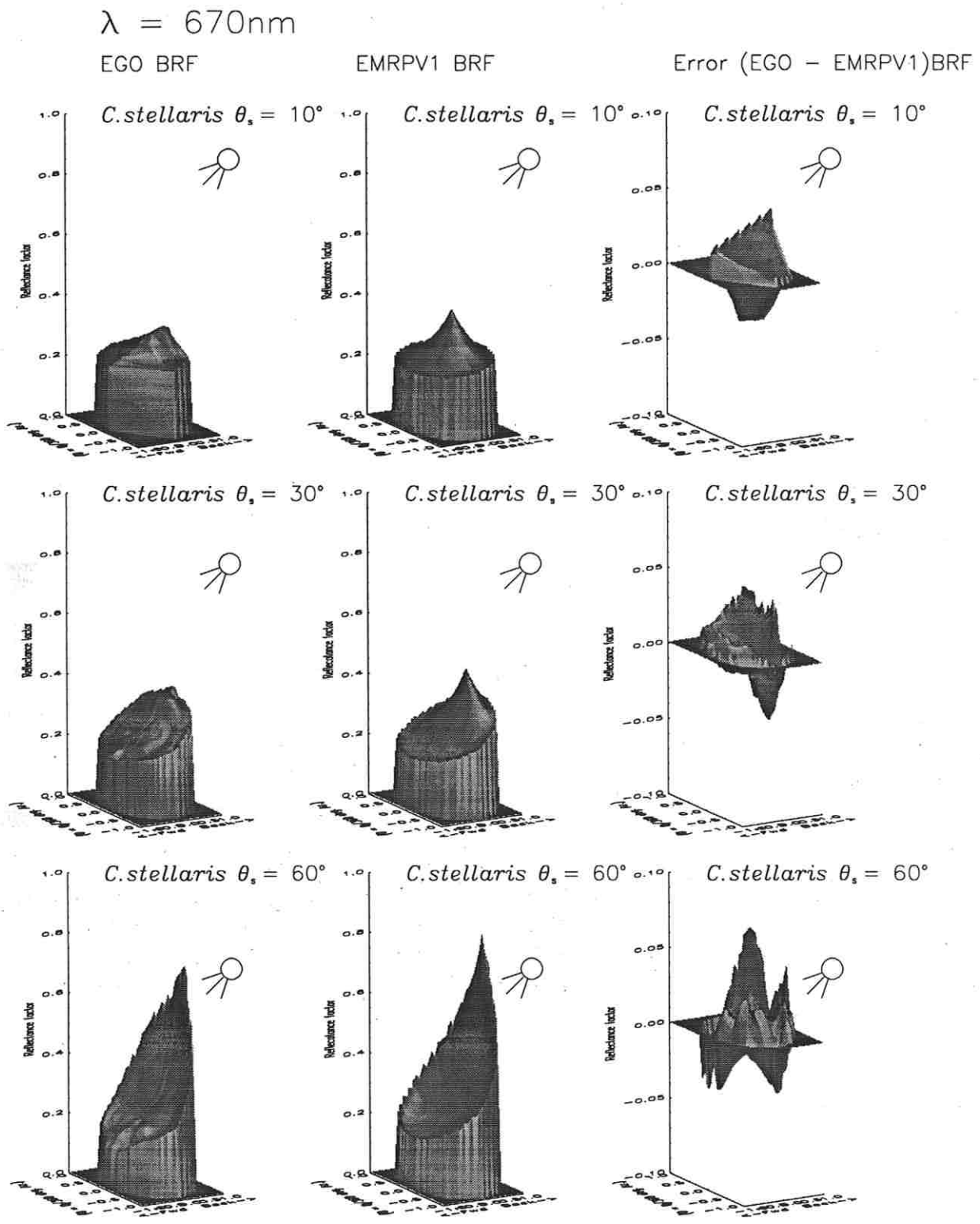

Figure 7.10: The BRF estimated based on EGO data and the predicted EMRPV1 BRF's for *Cladina stellaris*.

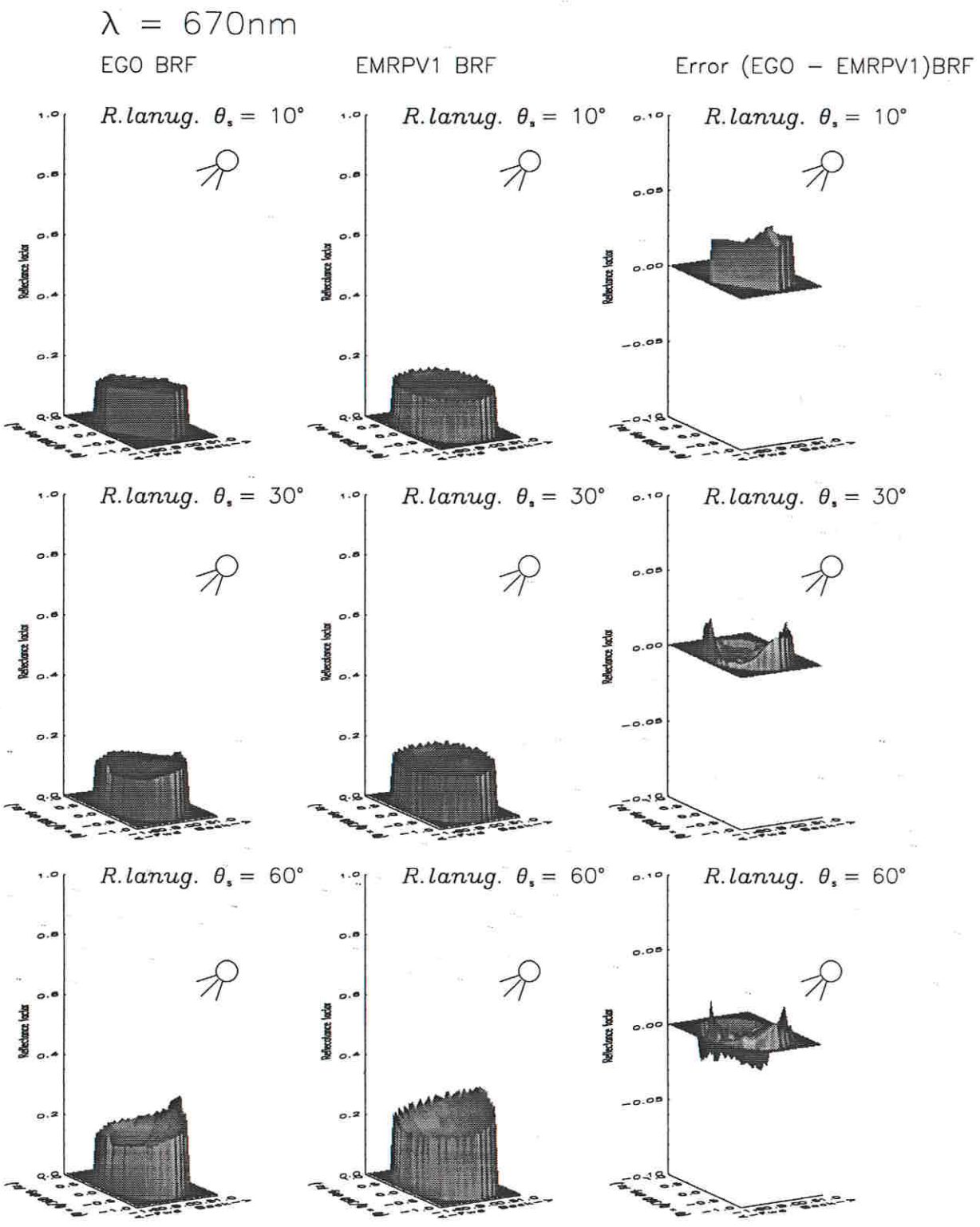

Figure 7.11: The BRF estimated based on EGO data and the predicted EMRPV1 BRF's for *Cladina stellaris*.

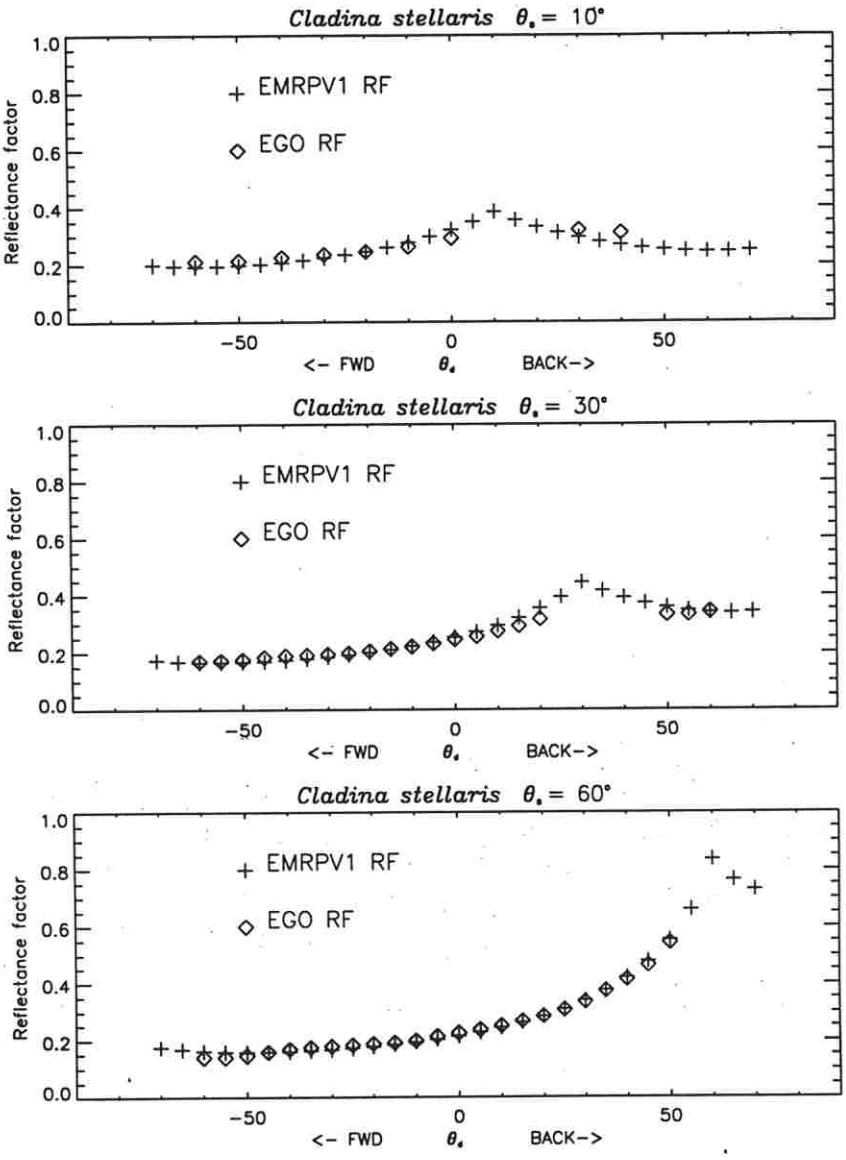

Figure 7.12: The RF estimated based on the EGO measurement, and the RF predicted by the EMRPV1 model. The principal plane for *Cladina stellaris*, for $\lambda = 670$ nm.

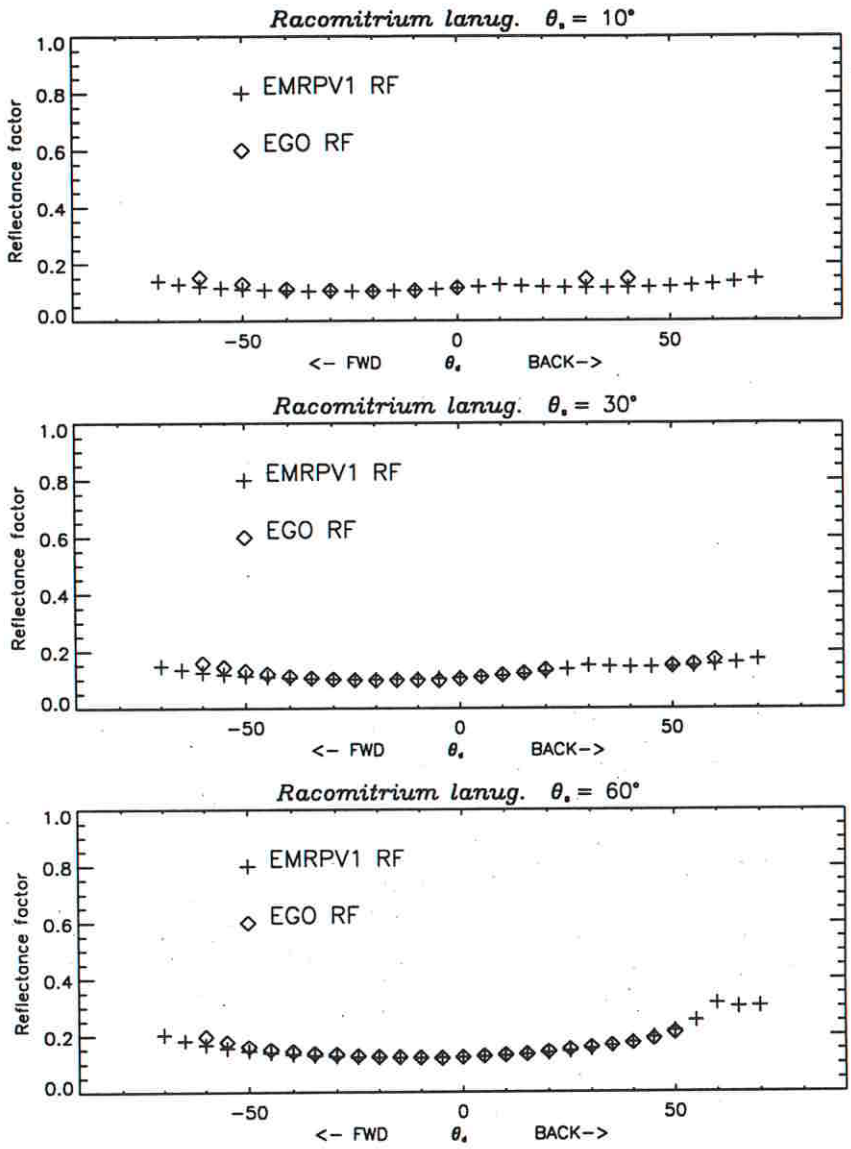

Figure 7.13: The RF estimated based on the EGO measurement, and the RF predicted by the EMRPV1 model. The principal plane for *Racomitrium lanuginosum*, for $\lambda = 670$ nm.

7.3 A physical BRF model of the data

In this chapter we will describe modelling results using the physical model reviewed in section 2.5. The model was developed by Verstraete, Pinty and Dickinson [105, 147], and is in the following referred to as the VPD model. As discussed in Section 2.5, the model has four physical parameters: ω, the average single scattering albedo; χ_l, a leaf orientation distribution parameter; Θ, an asymmetry factor; and $2\tau\Lambda$, a hot spot shape parameter. We chose this particular model because it includes parameters related both to the optical properties and the structure of the canopy. The VPD model is based on the assumptions that the canopy is semi-infinite and horizontally homogenous. Based on the biophysical descriptions of the targets given in Chapter 3, we assume that these assumptions are fulfilled.

7.3.1 Inversion of the VPD model

The inversion procedure consists of finding the parameters that minimize the total squared error between the predicted ($\hat{\rho}_s$)and the measured RF ($\hat{\rho}_t$).

$$\epsilon^2 = \sum_{i=1}^{I} (\hat{\rho}_{t_i} - \hat{\rho}_{s_i})^2 \tag{7.3}$$

The minimalization of ϵ^2 was done numerically by Powell's method as described in Numerical Recipes for C [107]. The advantage of this method is that it does not require estimates of the derivatives of the function to be minimized.

The parameters were initialized to random values within the legal ranges of the parameters. If an inversion converged with one or more parameter outside the legal range, the result was discarded, and the inversion procedure was restarted with a new set of randomly selected initial values.

To determine the necessary number of samples to use for each inversion, 180 inversions (3 targets $\times$ 4 wavelengths $\times$ 15 inversions) were done for $\theta_s = 30°$ and $\theta_s = 60°$, for a pre-selected number of randomly drawn samples. As can be seen from Figure 7.14 and Table A.8 in Appendix A, the inversion and test *rmsn* are equal for $I_{inversion} \geq 50$ for $\theta_s = 30°$, and the inversion and test *rmsn* are equal for $I_{inversion} \geq 175$ for $\theta_s = 60°$. For $\theta_s = 30°$, the test $\overline{rmsn} = 4.0\%$, and for $\theta_s = 60°$ the test $\overline{rmsn} = 5.3\%$. The same procedure was repeated for evenly drawn samples, with practically the same results (Table A.9 in Appendix A). Based on these observations, we decided to perform the inversion of the VPD model with 175 randomly drawn samples.

For each of the three targets and four wavelengths for $\theta_s = 30°$ and for $\theta_s = 60°$, we carried out 250 inversions, using the bootstrap procedure described in Section 2.6. The estimated parameters formed pronounced clusters or groups of solutions. Figure 7.15 shows the parameter clusters for *Cladina stellaris* for

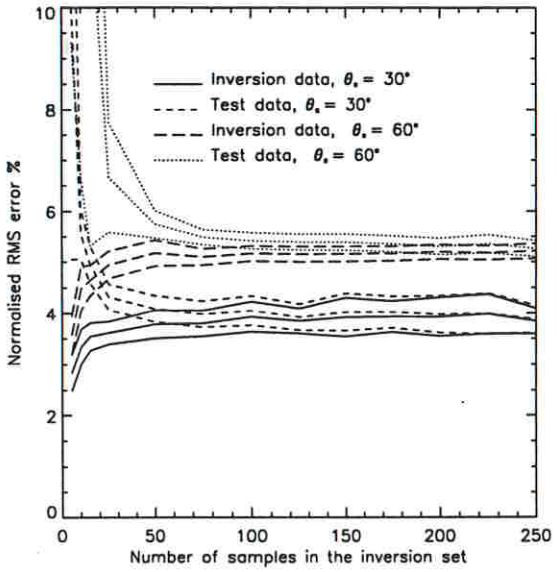

Figure 7.14: The average $\overline{rmsn}$ inversion and test errors and their $\alpha = 0.025$ confidence interval plotted against the number of samples used for inversion. Each point in the plot is sample estimate of 180 inversions of the VPD model.

$\lambda = 670$ nm and $\theta_s = 30°$. We see that the parameters form three clusters, one of which contains the resulting parameters from 80% of the inversions. This main cluster has a lower variance for $\hat{\Theta}$, $\hat{\omega}$, $2\hat{r}\Lambda$ and $\hat{\chi}_l$ than the other two clusters. The $rmsn$ is also lower for the main cluster than for the other two. The resulting parameters for the $\theta_s = 60°$ case are shown in Figure 7.16. The three clusters contain 38%, 36% and 25% of the data, respectively, and are not as well-separated as in the $\theta_s = 30°$ case. The cluster with the lowest variance and lowest $rmse$ was chosen as the main solution.

The parameters were clustered with an isodata algorithm [25]. We found that the parameters from the inversions typically grouped in two to seven clusters. For each target, wavelength, and source zenith angle, we chose the parameters forming the the most tightly packed cluster as the best parametric estimate. A tightly packed cluster is a cluster with many members and low variance. The other possible solutions or clusters were viewed as local minima or attractors in the error surface that was minimized during the inversion. The problem of lack of uniqueness of the set of parameters that fit the data has been noted by others, e.g. [24, 104]. Dominique and Hapke [24] showed that several phase curves, deducing different physical properties, could be fitted equally well to observations of astroide surfaces, when observations over a limited range of phase angles were available. They also note that unless the observations are such that $\theta_s - \theta_d < 2°, \phi_s = \phi_d = 0$, it is nearly impossible to establish the extent of the hot spot effect. A close sampling in the hot spot region is at the present not possible

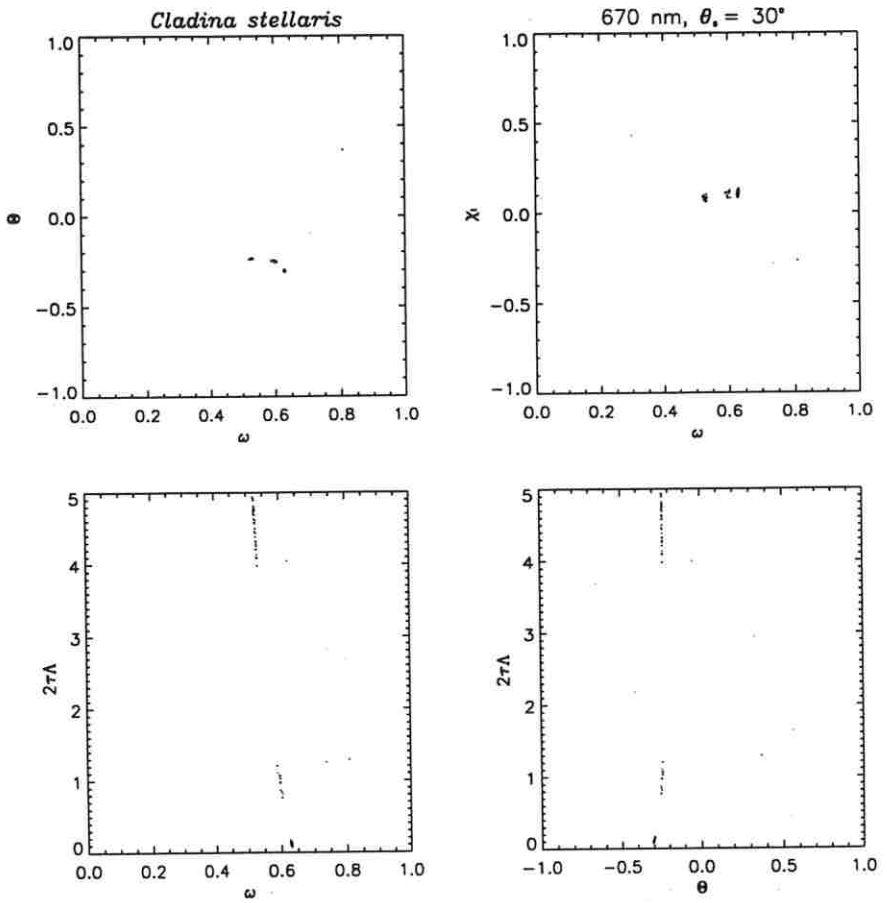

Figure 7.15: The parameter clusters for *Cladina stellaris*, for $\lambda = 670$ nm and $\theta_s = 30°$.

in the EGO experimental facility.

We inverted the VPD model on simulated data formed by the best parametric values for each target. Figure 7.17 shows that a higher probability of a convergence to the "correct solution" is achieved by including more samples to the inversion data. When 175 randomly drawn noise-free samples where used for the inversion, 90% and 75% of the inversions converged to the correct solution for $\theta_s = 30°$ and $\theta_s = 60°$, respectively. For the experimental data, we found that 77% and 50% of the solutions were included in the main parameter clusters, for $\theta_s = 30°$ and $\theta_s = 60°$, respectively.

7.3.2 Inversion results of the VPD model

Table 7.4 and 7.5 summarize the parameter estimates resulting from the inversion procedure described in the previous subsection. The parameter estimates given in Table 7.4 and 7.5 are discussed in detail in this section. The value of $100I/250$ indicates the percentage of the inversion parameters that fall within the main

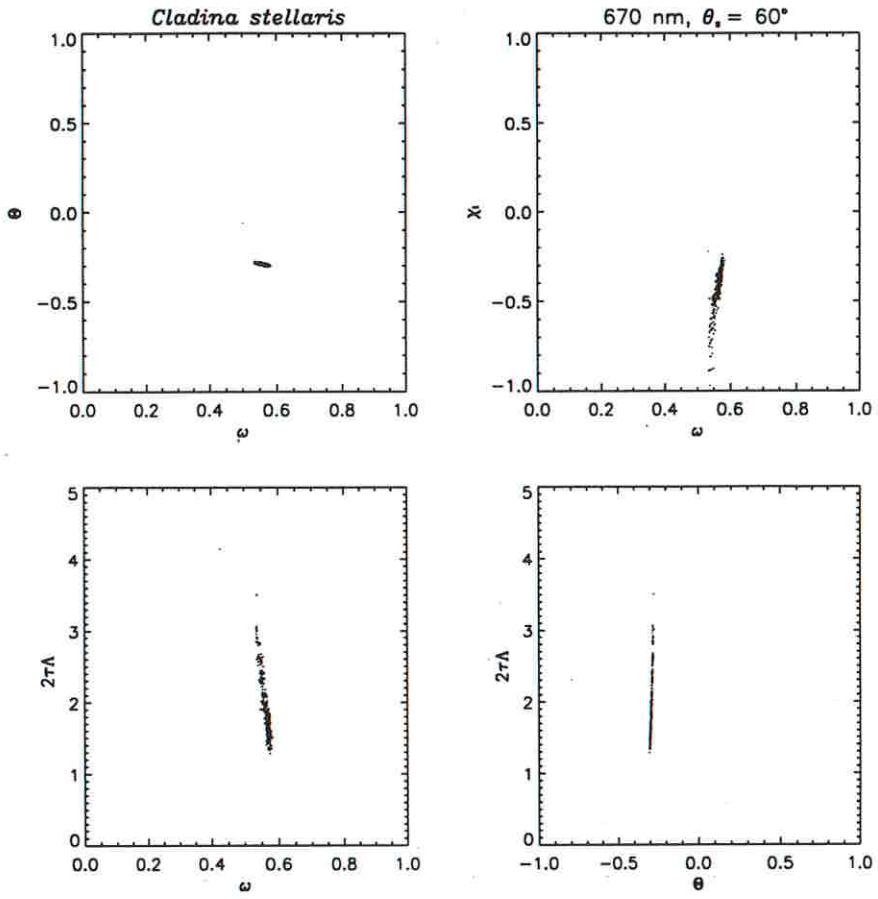

Figure 7.16: The parameter clusters for *Cladina stellaris*, for $\lambda = 670$ nm and $\theta_s = 60°$.

parametric cluster. The values and statistics in the tables are based on the values in the clusters that were chosen as the best solution.

The estimated asymmetry factor $\hat{\Theta}$ of the Henyey-Greenstein function is negative for both the lichen species ($-0.35 < \hat{\Theta} < -0.27$). This is reasonable since the lichens are backscattering canopies. For the moss, $\hat{\Theta}$ is close to zero ($-0.07 < \hat{\Theta} < -0.04$) for the visible wavelengths, and slightly negative in the NIR ($-0.13 < \hat{\Theta} < -0.10$). This indicates that the moss is quasi-isotropic in the visible, and slightly backscattering in the NIR.

The estimated parameters representing the single scattering albedo $\hat{\omega}$, appears to be reasonable. For the lichens, $\hat{\omega}$ increase from $0.34 < \hat{\omega} < 0.43$ for $\lambda = 441$ nm, to $0.55 < \hat{\omega} < 0.72$ for $\lambda = \{553, 670\}$ nm. For the moss, $0.25 < \hat{\omega} < 0.31$ for $\lambda = 441$ nm and $0.42 < \hat{\omega} < 0.49$ for $\lambda = \{553, 670\}$ nm. In the NIR, $0.85 < \hat{\omega} < 0.89$ for all three targets.

The $\hat{\chi}_l$ parameter represents the average orientation of the leaves, or "scattering particles". By visual inspection the *Flavocetraria nivalis* is dominated by erect thallus, which should result in a negative $\hat{\chi}_l$ value. This is indeed the case

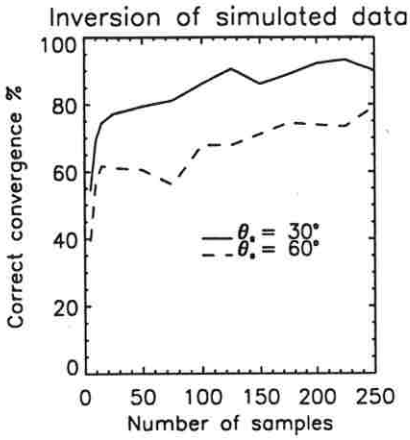

Figure 7.17: The percentage of inversions that converged to the correct solution for simulated data.

for $\theta_s = 60°$, for which our inversions gave $\hat{\chi}_l \approx -0.9$ in the visible, and $\hat{\chi}_l \approx -0.2$ in the NIR. For $\theta_s = 30°$, we found $\hat{\chi}_l \approx 0.2$, which indicates a predominance of horizontally oriented leaves. The thallus of *Cladina stellaris* forms tightly packed, small circular bulbs, which gives the clear impression of a spherical canopy, where all leaf angles are equally probable. The inversions gave $-0.4 < \hat{\chi}_l < -0.3$ for $\theta_s = 60°$, which indicates vertically oriented leaves, and $0.04 < \hat{\chi}_l < 0.14$ for $\theta_s = 30°$ which matches the impression of a uniform distribution of the leaf orientation. The moss consists of thousands of tiny erect green leafs, and each leaf has a small white tip with a random orientation. The inversion results gave $\hat{\chi}_l \approx 0.3$ for the visible wavelengths, and $\hat{\chi}_l \approx 0.2$, in the NIR, for $\theta_s = 30°$. For $\theta_s = 60°$, we found $-0.06 < \hat{\chi}_l < 0.12$.

Pinty *et al.* [105] found that when inverting BRF data from a soybean canopy, the χ_l parameter matched very well the values estimated based on independent leaf angle distribution measurements at visible wavelengths, but that the match was considerable poorer in the NIR. They did not report any significant difference in values retrieved at different solar zenith angles. According to Pinty *et al.*, a possible explanation for the parameter difference between visible and NIR wavelengths is due to that the term $H(x)$ which models multiple scattering is based on an assumption of isotropic scatterers. They argue that if this is not the case, then the inversion procedure might introduce values of χ_l that compensate for this modelling error. In the case of the lichens, with their high albedos, we have a significant degree of multiple scattering, especially in the pronounced hot spot regions observed for high solar zenith angles. The moss has a much lower albedo, and hence a much less pronounced hot spot, so in this case we do not expect to encounter this particular problem.

The $2r\Lambda$ parameter controls the width of the hot spot. Pinty *et al.* [105] argues that since this parameter depends only on the morphology of the canopy, the

parameter should be spectrally independent for a given illumination angle. They did however find some variability between the visible and the NIR. Our results also show a spectral dependency for this parameter. At the 99% confidence level, the only inversion results that are statistically equal for this parameter are for *Flavocetraria nivalis* $\lambda = 553$ nm and $\lambda = 670$ nm, *Cladina stellaris* for $\lambda = 670$ nm and $\lambda = 861$ nm for $\theta = 30°$, and for *Cladina stellaris* $\lambda = 441$ nm and $\lambda = 670$ nm, and for *Racomitrium lanuginosum* for $\lambda = 553$ nm and $\lambda = 670$ nm for $\theta_s = 60°$. However, for the lichens at $\theta_s = 30°$, the spectral difference is small, $(max(2r\Lambda) - min(2r\Lambda)) \leq 0.2$. For the moss the spectral difference is larger, especially between the visible and NIR ($(max(2r\Lambda) - min(2r\Lambda)) \leq 1.5$). For $\theta_s = 60°$, the spectral variation is much larger, the worst case is for *Flavocetraria nivalis* where $1.0 \leq 2r\Lambda \leq 4.03$. The variation is mostly due to the bad convergence properties of this particular parameter.

Figure 7.18 to 7.20 shows the BRF's of the main targets as modelled by the VPD model, for $\lambda = 670$ nm. The modelled BRF is plotted together with the BRF estimated based on the EGO measurements, as well as the error between the EGO BRF and VPD BRF. For $\theta_s = 30°$, the VPD model predicts a sharp narrow hot spot for the lichen targets. Since we lack measurements in the central part of the hot spot, we do not have information about the correct shape. However, from the visual inspection of the targets (e.g. Figure 7.1) we conceptually imagine a wide hot spot, not a narrow and sharp hot spot component. For $\theta_s = 60°$, we see a systematic error in that the model predicts a much narrower hot spot than what is actually measured. For the moss, most of the error is due to the specular peak and other local bumps in the data set.

Tables A.10 and A.11 in Appendix A, shows the estimated VPD model parameters, based on statistics from 15 inversions of each target, wavelength and source zenith angle, inverted on all available data. Again, the estimated parameters formed clusters of solutions. These coincided with the clusters found using the bootstrap method.

7.3.3 Inverting the model keeping one parameter fixed

To evaluate the significance or modelling power of each of the four parameters, we investigated the number of inversions that converged to the correct parametric solution, when one parameter was kept fixed at the correct value.

We used simulated data for this investigation. For each fixed parameter, we performed a total of 20 inversions of the VPD model, for each data set. The experiment was repeated using 10, 25, 50, 100, 175 and 225 samples of the data in the training set. In Section 7.3.1 we found that when 175 randomly selected noise-free samples were used for inversion, 90% of the inversions converged to the correct solution for $\theta_s = 30°$, and 75% converged for $\theta_s = 60°$.

We found that 97% of the inversions converged to the correct parametric solution, when either Θ or ω was kept constant, regardless of the number of

Table 7.4: Inversion results for the VPD model, for $\theta_s = 30°$.

Target wavelength	$100 * I/250$	$\bar{\Theta}$ $s(\Theta)$	$\bar{\omega}$ $s(\omega)$	$\bar{\chi}$ $s(\chi)$	$\overline{2r\Lambda}$ $s(\overline{2r\Lambda})$	$\overline{rmsn}$ $s(\overline{rmsn})$
F. nivalis		-0.3226	0.3772	0.1649	0.1272	4.4535
441	91.6%	0.0489	0.0182	0.0562	0.1729	1.7416
F. nivalis		-0.3566	0.7197	0.1687	0.0200	2.8341
553	92.0%	0.0022	0.0009	0.0069	0.0098	0.1606
F. nivalis		-0.3523	0.7182	0.1567	0.0217	2.8406
670	95.2%	0.0023	0.0009	0.0071	0.0108	0.1392
F. nivalis		-0.3285	0.8882	0.1803	0.0481	2.7264
861	96.8%	0.0032	0.0008	0.0058	0.0125	0.1675
C. stellaris		-0.2998	0.4371	0.0442	0.2018	4.4612
441	40.0%	0.0049	0.0025	0.0135	0.0496	0.2701
C. stellaris		-0.3066	0.6238	0.1057	0.1263	2.9964
553	74.4%	0.0034	0.0014	0.0086	0.0230	0.1614
C. stellaris		-0.3025	0.6294	0.1092	0.1160	2.7753
670	80.0%	0.0028	0.0011	0.0095	0.0159	0.1875
C. stellaris		-0.2875	0.8819	0.1418	0.1128	2.4969
861	92.8%	0.0034	0.0007	0.0059	0.0193	0.1578
R. lanuginosum		-0.0664	0.2492	0.3242	1.0907	6.0148
441	68.4%	0.0048	0.0027	0.0266	0.0734	0.3581
R. lanuginosum		-0.0465	0.4332	0.2627	1.5669	5.6717
553	42.8%	0.0048	0.0070	0.0254	0.2834	0.3202
R. lanuginosum		-0.0553	0.4164	0.2825	1.1832	5.9397
670	57.6%	0.0053	0.0036	0.0262	0.0472	0.3547
R. lanuginosum		-0.1333	0.8795	0.1586	0.1116	2.7106
861	96.8%	0.0051	0.0008	0.0054	0.0243	0.1215

samples used for the inversion. This indicates that these two parameters are very important for the model. When Θ or ω has attained their values, the rest of the parameters quickly fall within the corresponding cluster of solutions.

For a constant value of $2r\Lambda$, the performance improved from 93% to 98% when 100 or more samples were used for training. The same result was achieved for a fixed χ_l for the $\theta_s = 60°$ data. When χ_l was kept constant, approximately 79% of the lichen data for $\theta_s = 30°$ converged to a correct parametric solution. The result improved to 88% when 175 or more data samples were used for inversion. This indicates that the parameters χ_l and $2r\Lambda$ are the least significant parameters in the model, since the result is comparable to the result of inverting the model for all four parameters.

To conclude: the VPD model was capable of representing the BRF's of the selected canopies. However, the model convergence was not unique, since it

Table 7.5: Inversion results for the VPD model, for $\theta_s = 60°$

Target wavelength	$100 * I/250$	$\bar{\Theta}$ $s(\Theta)$	$\bar{\omega}$ $s(\omega)$	$\bar{\chi}$ $s(\chi)$	$\overline{2r\Lambda}$ $s(2r\Lambda)$	$\overline{rmsn}$ $s(\overline{rmsn})$
F. nivalis		-0.3230	0.3425	-0.9235	1.0052	5.6612
441	62.0%	0.0052	0.0046	0.0981	0.1723	0.3455
F. nivalis		-0.3062	0.6286	-0.8683	3.1379	4.3192
553	71.6%	0.0041	0.0052	0.1070	0.4352	0.2682
F. nivalis		-0.2973	0.6186	-0.8734	4.0337	4.1946
670	53.6%	0.0028	0.0052	0.1070	0.4691	0.2316
F. nivalis		-0.2884	0.8504	-0.2023	2.9718	4.3392
861	50.4%	0.0042	0.0042	0.0269	0.3619	0.2675
C. stellaris		-0.3091	0.3823	-0.3317	1.5279	7.7542
441	27.6%	0.0038	0.0035	0.0738	0.0450	0.4313
C. stellaris		-0.2946	0.5552	-0.3768	2.0480	5.8168
553	38.0%	0.0031	0.0059	0.0963	0.1438	0.3573
C. stellaris		-0.2980	0.5712	-0.3862	1.5478	5.5952
670	36.0%	0.0025	0.0042	0.0602	0.0970	0.3126
C. stellaris		-0.2733	0.8447	-0.2822	2.3861	4.9552
861	53.6%	0.0051	0.0041	0.0330	0.3427	0.4457
R. lanuginosum		-0.0702	0.3103	0.1240	0.7843	5.7327
441	39.6%	0.0944	0.0360	0.0386	0.1491	0.5924
R. lanuginosum		-0.0628	0.4867	0.0702	1.1879	5.7134
553	88.4%	0.0059	0.0101	0.0479	0.2918	0.2963
R. lanuginosum		-0.0636	0.4721	0.1176	1.1333	5.6289
670	71.2%	0.0049	0.0068	0.0371	0.1756	0.3748
R. lanuginosum		-0.1005	0.8571	-0.0699	1.7140	4.4141
861	72.4%	0.0041	0.0035	0.0211	0.1862	0.1907

converges to different sets of parameters, even for data generated by the model itself. The BRF's resulting from the different parameter sets are almost identical. The parameter representing the asymmetry factor of the phase function, and the parameter representing the single scattering albedo are the most important parameters in the model. These two parameters converge to reasonable values. The parameters representing the leaf orientation and the leaf density, are less important for the model. The physical interpretation of these parameters were doubtful.

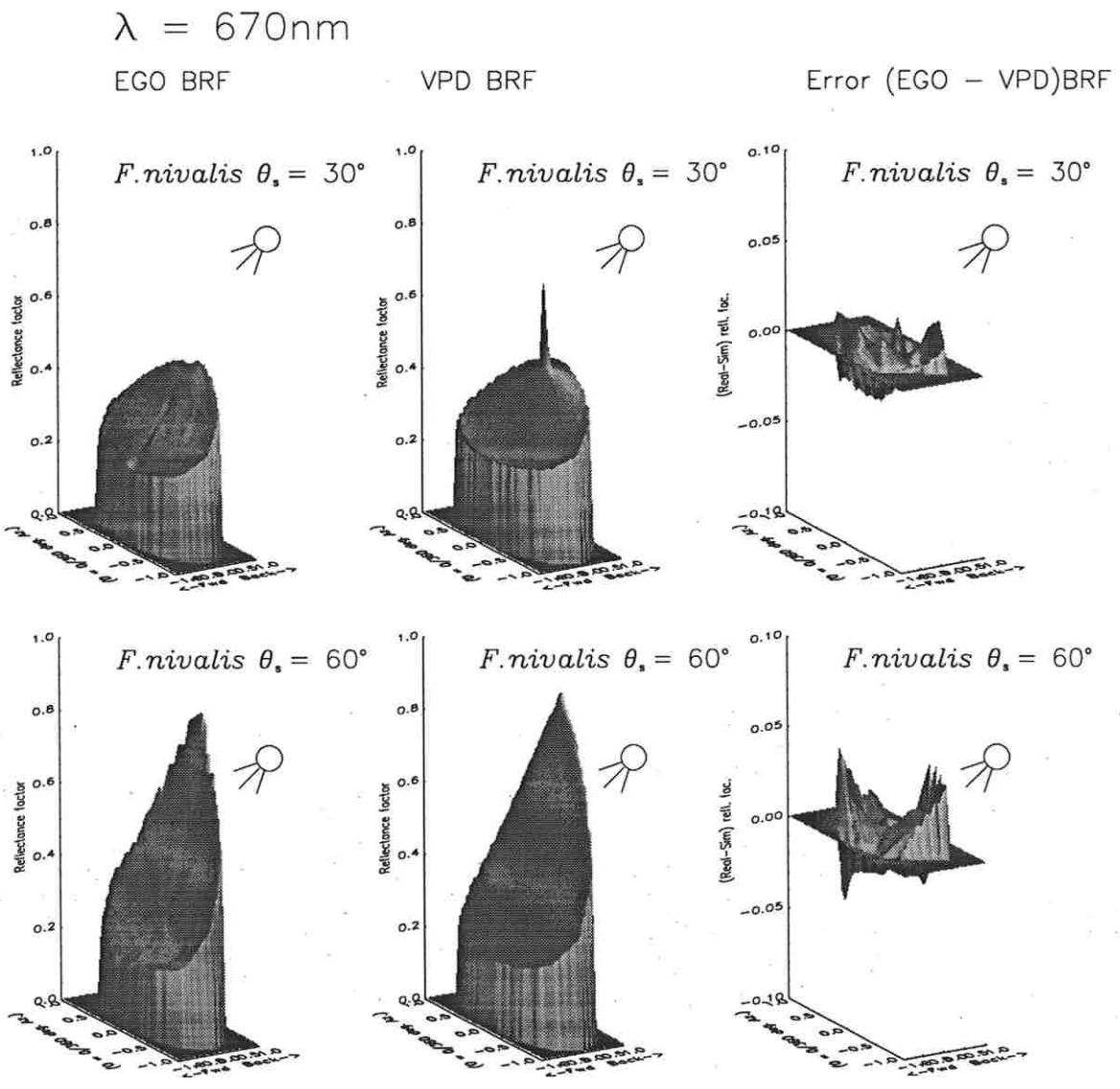

Figure 7.18: The BRF estimated based on EGO data and the predicted VPD BRF's for *Flavocetraria nivalis*.

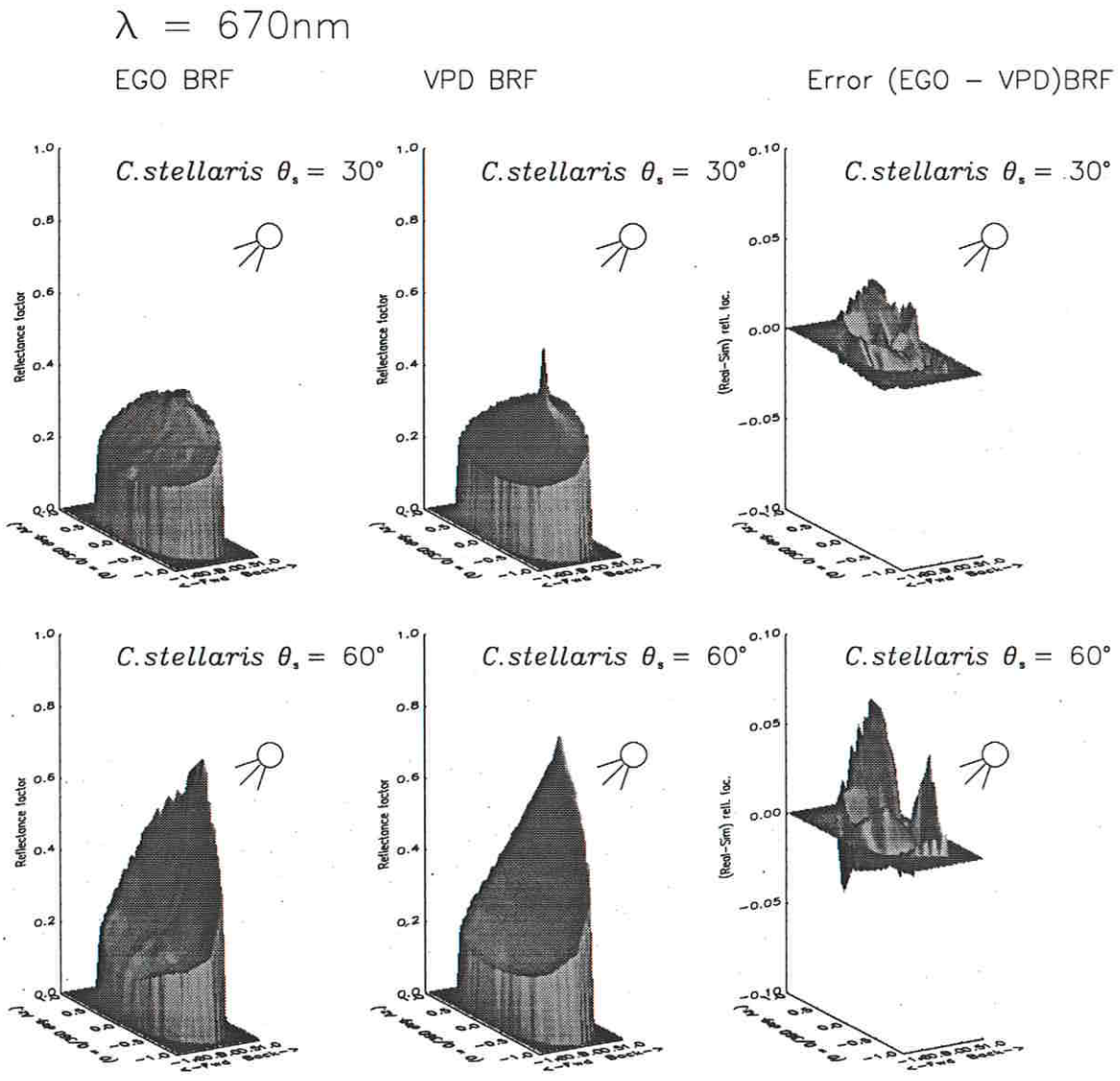

Figure 7.19: The BRF estimated based on EGO data and the predicted VPD BRF's for *Cladina stellaris*.

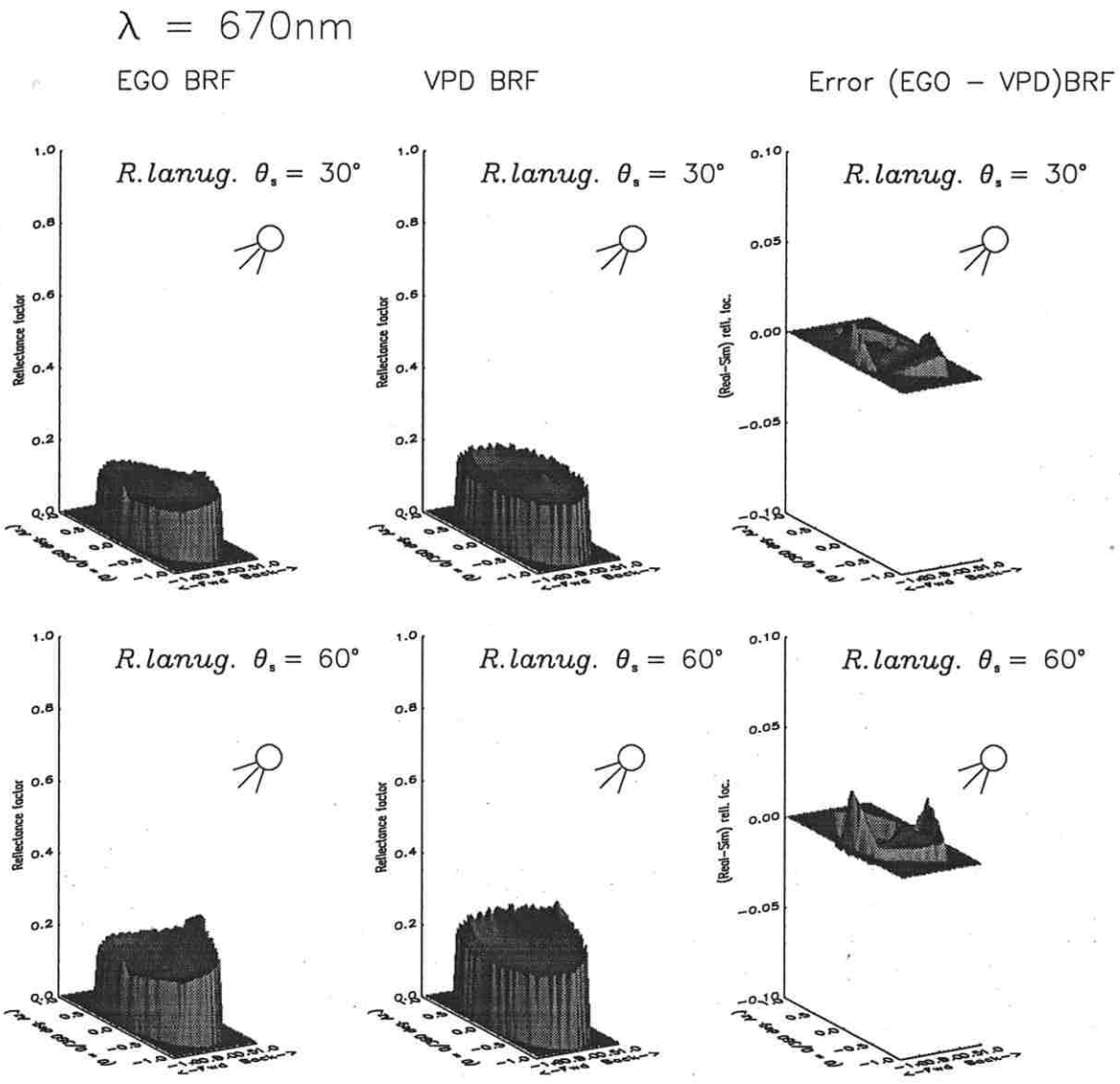

Figure 7.20: The BRF estimated based on EGO data and the predicted VPD BRF's for *Cladina stellaris*.

Chapter 8

Detection of Lichen Surfaces in Landsat TM Data

A main motivation for studying surface BRF's is the prospect to use the results to improve the reliability of surface remote sensing from space platforms. However, remote sensing in the visible and near infrared is strongly affected by the presence of the atmosphere. In this chapter we couple the modelled surface BRF's from the previous chapter, with an atmospheric radiative transfer model, in order to simulate the satellite signature. The results can in turn be used to produce a tool for surface target identification [29, 42], based on high-quality laboratory measurements.

In the case study presented here we simulate the top-of-atmosphere lichen BRF, and test it on real Landsat-5 Thematic Mapper data.

8.1 Estimation of the top of the atmosphere BRF

To simulate Landsat-5 TM data, we used the well known Second Simulation of the Satellite Signal in the Solar Spectrum (6S) model [143, 144]. The 6S-code is constructed to simulate the signal reflecting from a plane horizontal surface, in the wavelength range $250 \leq \lambda \leq 4000$ nm, assuming a cloud-free atmosphere as observed by a satellite. The 6S-code accounts for the main atmospheric effects, gaseous absorption by water vapor, carbon dioxide, oxygen and ozone, and scattering by molecules and aerosols. In the 6S library several BRF models are implemented, including the VPD [147, 105] and Rahman's model [112, 111]. The user can also define a grid of BRF values for a specific source zenith angle. We modified the Rahman model in the 6S simulation package, to match the EMRPV1 model as discussed in Section 2.4. In the 6S model, the contribution of a non-Lambertian target surface to the signal at the top of the atmosphere is given

as the sum

$$\hat{\rho}_{TOA} = a\rho_{t_1}(\theta_s, \theta_d, \phi) + b\rho_{t_2}(\theta_s, \theta_d, \phi) + c\rho_{t_3}(\theta_s, \theta_d, \phi) + d\rho_{t_4}(\theta_s, \theta_d, \phi) \quad (8.1)$$

where $a\rho_{t_1}(\theta_s, \theta_d, \phi)$ is the contribution of the photons transmitted directly from the Sun to the target and directly reflected back to the sensor, $b\rho_{t_2}(\theta_s, \theta_d, \phi)$ is the contribution from the photons scattered by the atmosphere and reflected by the target, and directly transmitted to the sensor, $c\rho_{t_3}(\theta_s, \theta_d, \phi)$ is the contribution from photons directly transmitted to the target, but scattered by the atmosphere on their way to the sensor,and $d\rho_{t_4}(\theta_s, \theta_d, \phi)$ is the contribution from the photons having at least two interactions with the atmosphere and one with the target [143, 144].

The 6S library contains geometric conditions for some of the most frequently used Earth observation satellites (e.g. Meteosat, NOAA, SPOT and Landsat), for user specified date and location (Lat/Long) or user specified view and illumination geometry. The user can select atmospheric conditions, aerosol model (type) and atmospheric correction mode, in terms of pre-defined or user specified conditions. These attributes makes the 6S code a user friendly and flexible tool. We will not go in detail into the model or numerics of the 6S, since we used the simulation package made available by the 6S group [143, 144].

If we assume a Lambertian Earth-atmosphere system, each pixel in a satellite scene can be converted to an above-the-atmosphere-reflectance by [23]

$$\rho = \pi L / \mu_s E_s \quad (8.2)$$

where $L = D\alpha + \beta$ is the satellite measured radiance, D is the digital count output of the satellite, α and β are the sensors gains and offsets respectively, E_s is the irradiance at the top of the atmosphere and $\mu_s = \cos(\theta_s)$. To convert the TM satellite scene to an above-the-atmosphere-reflectance, we used the gains, offsets and irradiance estimates provided with the particular TM scene. Recent publications on radiometric calibration of Landsat data can be found in e.g. [23, 90, 134].

The bidirectional scattering properties of the lichen, corresponding to TM bands 1,2,3 and 4 were estimated by (e.g. [23])

$$\hat{\rho}_{TMc}(\theta_s, \theta_d, \phi) = \frac{\sum_{i=0}^{n-1} \hat{\rho}(\lambda_i; \theta_s, \theta_d, \phi) S_c(\lambda_i)}{\sum_{i=1}^{n-1} S_c(\lambda_i)} \quad (8.3)$$

where λ_0 and λ_{n-1} are the upper and lower wavelength of TM c-band, $\hat{\rho}(\lambda_i; \theta_s, \theta_d, \phi)$ is the RF estimate based on the EGO measurements, and $S_c(\lambda)$ is the spectral response function of the TM c-band. The $S_c(\lambda)$ was re-sampled by linear interpolation to match our SE590 RF estimates. The resulting BRF's were used to invert the EMRPV1 model as described in Sections 2.4 and 7.2. Ideally, the BRF estimates should first be coupled with the atmosphere, and then filtered by

the spectral response function of the satellite. To save computational time, the broad-band BRF for each TM band was calculated before the BRF was used as input to the 6S model.

8.2 Results

We selected a Landsat-5 TM scene from August 25, 1996, Path = 195, Row = 11, covering the central part of Finnmark, Norway. The TM scene covers the Kautokeino kommune, where we conducted our field measurements in June 1996, as described in Section 6.3. The Kautokeino area serves as an important grazing field for domesticated reindeer herds. The area is rich on lichens and mosses. The *Cladina stellaris* and the *Flavocetraria nivalis* are found in large areas. The *Racomitrium lanuginosum* moss is a coastal species, and was therefore not present in any areas of the scene. The TM scene was georeferenced by a nearest neighbor resampling technique [63], in order not to distort the pixel values. The TM scene was classified by Johansen and Karlsen [63] by a procedure which includes both un-supervised and supervised classification. The classified image had sixteen ground reference classes, where lichens are present in seven. The classes of interest in this study were [63]:

TM-Class 9 Brush wood heaths with some lichens

TM-Class 10 Heather heaths, some lichens in oligothropic areas

TM-Class 11 Wind exposed heaths

TM-Class 12 Lichen brush wood forest, open forest with ground layer dominated by *Cladina stellaris*, *Flavocetraria nivalis* and *Cladina rangeferina, arbuscula* and *stygia.*

TM-Class 13 Lichen ridges dominated by *Cladina stellaris*, *Cladina rangeferina, arbuscula, stygia* and *Flavocetraria nivalis.* The thickness of the lichen layer depends on the grazing pressure.

TM-Class 14 Worn heathery moor, sparsely vegetated and eroded areas.

The TM scene is from a rather flat area, and therefore we did not take topographic effects into account. For each pixel in the satellite scene we estimated the weighted distance between the predicted $\hat{\rho}_{TOA}$ and the reflectance factor pixel values in the satellite scene $\hat{\rho}_{TM}$ by

$$D(\hat{\rho}_{TM}, \hat{\rho}_{TOA}) = \sqrt{\sum_{c=1}^{4} \frac{(\hat{\rho}_{TMc} - \hat{\rho}_{TOA})^2}{\bar{\rho}_{TMc}}} \tag{8.4}$$

where $\bar{\rho}_{TMc}$ is the average reflectance factor of the TM c-band.

First we calculated the histograms of the distance images D. Next we classifed the D images into 10 classes, such that the 10% of the D pixels with the lowest values were classified to Class D-1 the next 10% of the pixels to Class D-2 etc. Subsequently we calculated the class-statistics of the classified D image, with respect to the classified TM image. For the *Flavocetraria nivalis* we found:

- Class D-1: 18% of the pixels belong to TM-Class 12, 51% belong to TM-Class 13 and 20% belong to TM-Class 14.
- Class D-2: 34% of the pixels belong to TM-Class 12, 15% belong to TM-Class 13, and 21% belong to TM-Class 14.

TM-Class 12 was the dominating class also for class D-3 with 34%, D-4 with 29% and D-5 with 20%. The areas where we conducted our field measurements discussed in Section 6.3 were classified as this particular class.

The *Cladina stellaris* is one of the most dominating lichens in the area, and its signature matched most of the classes for exposed areas quite well:

- Class D-1: 15% of the pixels belong to TM-Class 11, 30% belong to TM-Class 12, 8% belong to TM-Class 13, and 15% belong to TM-Class 14.
- Class D-2: 12% of the pixels belong to TM-Class 9, 31% belong to TM-Class 12, 10% belong to TM-Class 13, and 15% belong to TM-Class 14

Figure 8.1 shows the classified D image for the *Flavocetraria nivalis*. The image is colour coded as follows: white is Class D-1, yellow is Class D-2, green colours are Classes D-3 to D-5, grey to black are Classes D-6 to D-10.

In the lower right quadrant of the image in Figure 8.1, we see the Finnish/Norwegian border. Along this border there is a fence preventing the Finnish and Norwegian reindeer herds from crossing the border. The reindeer pressure on the Norwegian side is lower than on the Finnish side [60, 61, 62]. Therefore we clearly see a larger abundance of lichens on the Norwegian side.

The results of this chapter demonstrates that lichen covered areas can be detected in TM images based on laboratory BRF measurements.

Figure 8.1: The classified distance image based on the predicted *Flavocetraria nivalis* top-of-the-atmosphere reflectance factor.

Chapter 9

Conclusions

In this thesis, we have carefully investigated the spectral and bidirectional scattering properties of *Cladina stellaris* and *Flavocetraria nivalis* lichen canopies and *Racomitrium lanuginosum* moss canopies for visible and near-infrared wavelengths. Our results are primarily based on bidirectional spectral measurements made in the EGO facility. An important part of this thesis is devoted to the characterization of the precision of the EGO measurements. We used these characteristics to suggest ways to improve the quality of data, and to reduce measurement errors. We documented an intensity drift in the 1000 W collimated lamp of up to 3.5% during a single day of measurements, for the wavelength $\lambda = 670$ nm. We found clear indications that the variations in the irradiation was caused by variations in the voltage supply to the lamp. By correcting for the low-frequency variations in the irradiation, we could reduce the intensity drift to less than 2.1%. We found that the lamp spot was slightly left-right asymmetrical, and that the center of field-of-view of a detector could vary up to 9.3 cm, depending on the detector position. We found that these effects worsened for detector zenith angles $|\theta_d| > 60^o$. Our analysis shows that for measurements at these extreme angles, experimental errors as large as 14% in the raw data can be expected. We therefore excluded measurements acquired at positions $|\theta_d| > 60^o$ from our analysis. Since the inhomogeneity of the lamp spot, and the displacement of the center of field of view are the same for both target and reference panels, the effects of this is reduced when estimating reflectance factors. However, we used a GORE–TEX^{TM} reference panel that had a strong specular component for large source zenith angles. We therefore had to correct for this effect as well. After invoking all our suggested corrections, we conclude that the precision of the experimental BRF estimates are within 2% of their mean value.

We carried out experiments to establish the spectral signatures of the selected targets in both dry and moist states. We found that the spectral signatures of the dry *Flavocetraria nivalis* and *Cladina stellaris* have much higher RF's than what is typical of green vegetation. The *Racomitrium lanuginosum* had a spectral RF similar to those typical of dry or stressed green leaves. Our results indicate a

higher RF for the wet lichens, compared to the dry, in both visible and NIR wavelength bands. A possible explanation for the increased spectral reflectance of the moistened lichens in the visible region, is that the physical swelling of the lichens resulted in a denser canopy and therefore less internal shadowing. A second explanation is linked to biophysical properties of the pigments of the lichens. The moss changes from a greyish colour to dark green when it is moistened. Therefore, the moist moss exhibit lower RF's than the dry for visible wavelengths. For NIR wavelengths, the moist moss had higher RF's.

We also compared our laboratory spectral signatures with those of field measurements at sites in Norway and on Svalbard. We found an excellent agreement between the RF estimates of the targets from field measurements and the nadir RF estimates acquired in the EGO.

We have presented experimental BRF's of the *Cladina stellaris*, *Flavocetraria nivalis* and *Racomitrium lanuginosum* canopies from the EGO facility. Both lichen targets investigated have a significant hot spot for both visible and NIR wavelengths. The moss shows a quasi-isotropic reflectance pattern for visible wavelengths, but has a significant hot spot in the NIR.

We modelled the data by means of the parametrical EMRPV1 [29, 30] model, and the physical VPD model [105, 147]. We found that the EMRPV1 model was flexible and reliable because the inversion results were valid for a large range of source zenith angles. Furthermore, we found that the model was numerically stable because it consistently converged to the same parametric solution, as long as a sufficient number of measurements were used for the inversion. The VPD model was less flexible because we had to perform an inversion for each source zenith angle. The lack of stability also led to a convergence to different parametric solutions, depending on the specific set of measurements that were included in the data set, and on the initialization of the inversion. The VPD model parameters representing the single scattering albedo and the asymmetry factor of the phase function converged to reasonable values, whereas the interpretability of the parameters representing the leaf orientation and the leaf density were doubtful. Both models required large number of BRF samples for the inversion error to reach an acceptable low level. We used the bootstrap method in order to achieve confidence intervals for the model parameters.

We used the EMRPV1 modelled BRF's for the lichen canopies with the 6S model in order to simulate the Landsat TM top-of-the-atmosphere reflectance factors. We demonstrated that top-of-the-atmosphere reflectance factors could be succsessfully used to detect areas with a high percentage of lichen cover in a Landsat TM scene.

Bibliography

[1] S. P. AHMAD AND D. W. DEERING, *"A Simple Analytical Function for Bidirectional Reflectance"*, J. Geophys. Res. 97 (1992), pp. 18867–18886.

[2] V. AHMADJIAN, *"The Lichen Symbiosis"*, Wiley, 1993.

[3] G. ASRAR, ed., *"Theory and applications of optical remote sensing"*, Wiley, 1989.

[4] G. ASRAR, R. B. MYNENI, AND E. T. KANEMASU, *"Estimation of Plant-Canopy Attributes from Spectral Reflectance Measurements"*, in Theory and Applications of Optical Remote Sensing, G. Asrar, ed., Wiley, New York, 1989, ch. 7, pp. 252–296.

[5] J. W. BATES AND A. M. FARMER, eds., *"Bryophytes and Lichens in a Changing environment"*, Oxford University Press, 1992.

[6] M. E. BAUER, C. S: T. DAUGHTRY, L. L. BIEHL, E. T. KANEMASU, AND F. G. HALL, *"Field Spectroscopy of Agricultural Crops"*, IEEE Trans. Geosci. Remote Sens., GE-24 (1986), pp. 65–75.

[7] B.HAPKE, *"Are planetary regolith particle back scattering? Response to paper by M. Mishchenko"*, J. Quant. Spectrosc. Radiat. Transfer, 55 (1996), pp. 837–848.

[8] G. J. BHATTACHARYYA AND R. A. JOHNSON, *"Statistical Concepts and Methods "*, Wiley, 1977.

[9] F. BOOCHS, G. KUPFER, K. DOCKTER, AND W. ÜHBAUCH, *"Shape of the red edge as vitality indicator for plants"*, Int. Journ. Remote Sens., 11 (1990), pp. 1741–1753.

[10] T. W. BRAKKE, W. P. WERGIN, E. F. ERBE, AND J. M. HARDEN, *"Seasonal Variations in the Structure and Red Reflectance of Leaves from Yellow Poplar, Red Oak, and Red Maple "*, Remote Sens. Environ., 43 (1993), pp. 115–130.

[11] C. BUSCHMANN AND E. NAGAL, *"Reflection Spectra of Terrestrial Vegetation as Influenced by Pigment-Protein Complex and the Internal Optics of the Leaf Tissue"*, in IGARSS'91, Helsinki, Finland, June 1991, IEEE, pp. 1909–1912.

[12] C. BUSCHMANN, E. NAGAL, S. RANG, AND F. STOBER, *"Interpretation of Reflectance Spectra of Terrestrial Vegetation Based on Spectral Plant Test Systems"*, in IGARSS'90, Washington DC, May 20–24 1990, IEEE, pp. 1927–1930.

[13] G. A. CARTER, *"Primary and Secondary Effects of Water Content on the Spectral reflectance of Leaves"*, Am. J. Botany, 78 (1991), pp. 916–924.

[14] ——, *"Responses of Leaf Spectral Reflectance to Plant stress"*, Am. J. Botany, 80 (1993), pp. 239–243.

[15] S. CHANDRASEKHAR, *"Radiative Transfer"*, Dover, 1960.

[16] J. CHEN, *"Kubelka-Munk equations in vector-matrix forms and the solution for bidirectional vegetation canopy reflectance"*, Appl. Opt., 24 (1985), pp. 376–382.

[17] J. D. COX, P. BECKETT, AND G. COURTIN, *"Factors Affecting Spectral Response from Lichens*, in Proc. 8th Thematic Conference on Geological Remote Sensing", Denver, Colorado, 1991, pp. 1125–1137.

[18] A. CRACKNELL AND L. HAYES, *"Introduction to remote sensing"*, Taylor & Francis Ltd, London, UK, 1991.

[19] D. W. DEERING, *"Field Measurements of Bidirectional reflectance"*, in Theory and Applications of Optical Remote Sensing, G. Asrar, ed., Wiley, New York, 1989, ch. 2, pp. 14–65.

[20] D. W. DEERING, S. AHMAD, T. ECK, AND B. BANERJEE, *"Temporal Attributes of the Bidirectional Reflectance for Three Boreal Forest Canopies"*, in Proc. IGARSS'95, Firenze, Italy, July 1995, pp. 1239–1241.

[21] D. W. DEERING, E. A. MIDDLETON, AND J. R. IRONS, *"Prairie Grassland Bidirectional Reflectance Measured by Different Instruments at the FIFE Site"*, J. Geophys. Res. 97 (1997), pp. 18887–18903.

[22] D. DENNISON AND T. C. VOGELMANN, *"The Phycomyces lens: measurements of the sporangiophore intensity profile using a fiber optic microbe"*, Planta, 179 (1989), pp. 1–10.

[23] M. DINGUIRARD AND P. N. SLATER, *"Optical sensor calibration "*, in Physical Measurements and Signatures in Remote Sensing, G. Guyot and T. Phulpin, eds., vol. 1 of Seventh international Symposium on Physical Measurements and Signatures in Remote Sensing, Courchevel, France, April 1997, ISPRS, Balkema Publ. NL, pp. 9–17.

[24] D. DOMINIQUE AND B. HAPKE, *"Fitting Theoretical Photometric Functions to Asteroids Phase Curves"*, ICARUS, 78 (1989), pp. 330–336.

[25] R. O. DUDA AND P. HART, *"Pattern Classification and Scene Analysis"*, Wiley, New York, 1973.

[26] B. EFRON, *"The Jackknife, the Bootstrap and Other Resampling Plans"*, SIAM, 1982.

[27] B. EFRON AND R. T. TIBSHIRANI, *"An Introduction to the Bootstrap"*, Chapman & Hall, New York, 1993.

[28] A. ELVEBAKK, *"Tundra Diversity and Ecological Characteristics of Svalbard"*, in "Ecosystems of the World 3", F. E. Wielgolaski, ed., Elsevier, Amsterdam, 1997, pp. 347–359.

[29] O. ENGELSEN, *"An investigation of the coupled surface-atmosphere radiative transfer problem of remote sensing in the visible near-infrared spectral bands and its inversion"*, PhD thesis, University of Tromsø, Tromsø, Norway, February 1997.

[30] O. ENGELSEN, B. PINTY, M. M. VERSTRAETE, AND J. V. MARTONCHIK, *"Parametric Bidirectional Reflectance Factor Models: Evaluation, Improvements and Applications"*, Tech. Rep. EUR 16426 EN, Joint Research Centre (JRC) European Commission, Ispra,(VA) Italy, 1996.

[31] B. FREEDMAN AND C. HUTCHINSON, *"Long-term effects of smelter pollution at Sudbury, Ontario, on forest community composition"*, Can. Journ. Remote Sens., 58 (1980).

[32] E. FREMSTAD AND R. ELVEN, eds., *"Enheter for vegetasjonskartlegging i Norge"*, Økoforsk/NINA Utred., Trondheim, Norway, 1987, ch. A1, pp. A–2, A–3.

[33] J. GASTELLU-ETCHEGORRY, F. ZAGOLSKI, AND J. ROMIER, *"A Simple Reflectancd Model for Homogeneous Multilayer Canopies"*, Remote Sens. Environ., 57 (1996), pp. 22–38.

[34] D. M. GATES, H. J. KEEGAN, J. C. SCHLETER, AND V. R. WEIDNER, *"Spectral Properties of Plants"*, Appl. Opt., 4 (1965), pp. 1–65.

[35] Y. GAUSLAA, *"Heat resistance and energy budget in different Scandinavian plants"*, Holarctic Ecology, 7 (1984), pp. 1–78.

[36] Y. GAUSLAA, C. KOPPERLUND, AND K. A. SOLHAUG, *"Optimal Quantum of Photosystem II and Chlorophyll Degradation of Lobaria pulmonaria in Relation to pH*"*, Lichenologist, 23 (1996), pp. 267–278.

[37] F. F. GERARD AND P. J. NORTH, *"Analyzing the Effect of Structural Variability and Canopy Gaps on Forest BRDF Using a Geometric-Optical Model"*, Remote Sens. Environ., 62 (1997), pp. 46–62.

[38] N. GOBRON, B. PINTY, M. M. VERSTRAETE, AND Y. GOVAERTS, *"A semi-Discrete Model for the Scattering of Light by Vegetation"*, J. Geophys. Res. 102 (1997), pp. 9431–9446.

[39] N. S. GOEL, *"Models of Vegetation Canopy Reflectance and Their Use in Estimation of Biophysical Parameters from Reflectance Data"*, Remote Sens. Rev. 4 (1988), pp. 1–221.

[40] ——, *"Inversion of Canopy reflectance models for estimation of biophysical parameters from reflectance data"*, in Theory and Applications of Optical Remote Sensing, G. Asrar, ed., Wiley, New York, 1989, ch. 6, pp. 205–251.

[41] N. S. GOEL AND T. GRIER, *"Estimation of Canopy Parameters of Row Planted Vegetation Canopies Using Reflectance Data for Only Four View Directions"*, Remote Sens. Environ., 21 (1987), pp. 37–51.

[42] Y. GOVAERTS, O.ENGELSEN, B. PINTY, AND M. VERSTRAETE, *"Identification of a particular tropical forest environment on the basis of simulated NOAA-AVHRR reflectance factors"*, in Physical Measurements and Signatures in Remote Sensing, G. Guyot and T. Phulpin, eds., vol. 2 of Seventh international Symposium on Physical Measurements and Signatures in Remote Sensing, Courchevel, France, April 1997, ISPRS, Balkema Publ. NL, pp. 727–734.

[43] Y. M. GOVAERTS, *"A model of light scattering in three-dimensional plant canopies: A Monte Carlo ray tracing approach"*, Tech. Rep. EUR 16394 EN, Joint Research Centre (JRC) European Commission, Ispra, Italy, 1996.

[44] Y. M. GOVAERTS, S. JACQUEMOUND, M. M. VERSTRAETE, AND S. L. USTIN, *"Three-dimensional radiation transfer modeling in a dicotyledon leaf"*, Appl. Opt., 35 (1996), pp. 6585–6598.

[45] Y. M. GOVAERTS AND M. M. VERSTRAETE, *"Raytran: A Mote Carlo Ray-Tracing Model to Compute Light Scattering in Three-Dimensional Heterogeneous Media"*, IEEE Trans. Geosci. Remote Sens., 36 (1998), pp. 493–505.

[46] M. E. HALE, *"The Biology of Lichens"*, Edward Arnold, 2 ed., 1974.

[47] B. HAPKE, *"Theory of reflectance and emittance spectroscopy"*, University Press, Cambridge, 1993.

[48] B. HAPKE, D. DIMUCCI, R. NELSON, AND W. SMYTHE, *"The Cause of the Hot Spot in Vegetation Canopies and Soils: Shadow-Hiding Versus Coherent Backscatter"*, Remote Sens. Environ., 58 (1996).

[49] R. HECT-NIELSEN, *"Neurocomputing"*, Addison-Wesley, 1990.

[50] J. HERTZ, A. KROGH, AND R. PALMER, *"Introduction to the Theory of Neural Computation"*, Addison-Wesley, Redwood City, California, 1991.

[51] R. M. HOFF, *"Biological and Physical Considerations in applying Computer-aided analysis Techniques to Remote Sensing Data"*, in "Remote Sensing: The Quantitative Approach", P. H. Swain and S. Davis, eds., McGraw-Hill, New York, 1978, ch. 5, pp. 227–289.

[52] K. A. HØGDA, H. TØMMERVIK, AND I. SOLHEIM, *"Use of multitemporal Landsat image data for mapping the effects from air pollution in the Kirkenes-Pechenga area in the period 1973-1994"*, Tech. Rep. IT2039/1-95, NORUT IT, Tromsø, Norway, 1995.

[53] B. HOSGOOD, S. JACQUEMOUD, G. ANDREOLI, J. VERDEBOUT, G. PEDRINI, AND G. SCHMUCK, *"Leaf Optical Properties Experiment93 (LOPEX93)"*, Tech. Rep. EUR16095EN, Joint Research Centre (JRC) European Commission, Ispra (VA), Italy, 1994.

[54] B. HU, W. LUCHT, X. LI, AND A. H. STRAHLER, *"Validation of Kernel-Driven Semiempirical Models for Surface Bidirectional Reflectance Distribution Functions of Land Surfaces"*, Remote Sens. Environ., 62 (1997), pp. 201–214.

[55] D. R. HUSH AND B. HORNE, *"Progress in Supervised Neural Networks What's new since Lippmann?"*, IEEE Signal Processing Magazine, (1993), pp. 8–39.

[56] J. IAQUINTA AND J. L. PRIVETTE, *"Inversion of a physically Based Bidirectional Reflectance model of Vegetation"*, IEEE Trans. Geosci. Remote Sens., 35 (1997), pp. 687–698.

[57] R. D. JACKSON, T. R. CLARKE, AND M. S. MORAN, *"Bidirectional Calibration of 16 $BaSO_4$ Reference Reflectance Panels"*, Remote Sens. Environ., 40 (1992), pp. 231–239.

[58] S. JACQUEMOUD, F. BARET, B. ANDRIEU, F. DANSON, AND K. JAGGARD, *"Extraction of Vegetation Biophysical Parameters by Inversion of the PROSPECT+SAIL Models on Sugar Beet Canopy Reflectance Data. Application to TM and AVIRIS Sensors"*, Remote Sens. Environ., 52 (1995), pp. 163–172.

[59] J.IAQUINTA AND B. PINTY, *"Radiation field in a multilayered geophysical medium: Ice-water-aerosol-vegetation-soil (IWAVES) model"*, J. Geophys. Res. 102 (1997), pp. 13627–13642.

[60] B. JOHANSEN AND H. TØMMERVIK, *"Mapping Winter Grazing Areas for Reindeer in Finnmark County, Northern Norway, Using Landsat 5-TM Data"*, in IGARSS-90, Washington DC, 1990.

[61] ——, *"Finnmarksvidda Vegetasjonskartlegging -vegetasjonstyper, lavbeiter og endringer i lavdekket innen reinbeitedistrikt 30 og 31, Finnmarksvidda."*, Tech. Rep. 2020/1, FORUT AS, Tromsø, Norway, 1992.

[62] B. E. JOHANSEN, M.-E. JOHANSEN, AND S. R. KARLSEN, *"Vegetasjons - og beitekartlegging i Finnmark og Nord-Troms"*, Tech. Rep. IT2026/1, NORUT IT, Tromsø, Norway, 1995.

[63] B. E. JOHANSEN AND S. R. KARLSEN, *"Endringer i lavdekket på Finnmarksvidda 1987–1996 basert på Landsat 5/TM data"*, Tech. Rep. IT475/1, NORUT IT, Tromsø, Norway, 1998.

[64] I. KÄRNEFELT, *"The brown fruticose species of Cetraria"*, Opera Botanica, (1979).

[65] I. KÄRNEFELT, J. E. MATTSON, AND A. THELL, *"Evolution and phylogeny of cetrarioid lichens"*, Pl. Syst. Evol., 183 (1992), pp. 113–160.

[66] I. KÄRNEFELT, A. THELL, T. RANDLAN, AND A. SAAG, *"The genus Flavocetraria K"arnefelt & Thell (Parmeliaceae, Ascomycotina) and its affinites"*, Acta. Bot. Fennica., 150 (1994), pp. 79–86.

[67] T. KAVLI, *"ASMOD-An algorithm for Adaptive Spline Modelling of Observation Data"*, Int. J. of Control, 58 (1993), pp. 947 – 967.

[68] S. M. KAY, *"Fundamentals of Statistical Signal Processing"*, Prentice Hall, Englewood Cliffs, New Jersey, 1993.

[69] K. A. KERSHAW, *"Physiological ecology of lichens"*, Cambridge University Press, Cambridge, UK, 1985.

[70] D. S. KIMES, *"Dynamics of directional reflectance factor distributions for vegetation canopies"*, Appl. Opt., 22 (1983), pp. 1364–1372.

[71] D. S. KIMES, *"Modeling the directional reflectance from complete homogeneous vegetation canopies with various leaf-orientation distributions"*, J. Opt. Soc. Am. A1 (1994), pp. 725–737.

[72] D. S. KIMES AND J. A. KIRCHNER, *"Irradiance Measurement Errors Due to the Assumption of a Lambertian Reference Panel "*, Remote Sens. Environ., 12 (1982), pp. 141–149.

[73] D. S. KIMES, W. W. NEWCOMB, R. F. NELSON, AND J. B. SCHUTT, *"Directional Reflectance Distribution of a Hardwood and Pine Forest Canopy"*, IEEE Trans. Geosci. Remote Sens., GE–24 (1986), pp. 281–293.

[74] K. T. KRIBEL, *"Measured spectral bidirectional reflection properties of four vegetation surfaces"*, Appl. Opt., 17 (1978), pp. 253–259.

[75] K. T. KRIEBEL, *'"The Spectral Reflectance of a Vegetated Surface, Part 1: Method and Application"*, Beiträge zur Physik der Atmosphäre, 47 (1974), pp. 14–44. in German.

[76] A. KUUSK, *"The Hot Spot Effect in Plant Canopy Reflectance"*, in "Photon Vegetation Interactions, Applications in Optical Remote Sensing and Plant Ecology", R. B. Myneni and J. Ross, eds., Springer-Verlag, 1991, ch. 5, pp. 140–159.

[77] ——, *"A Multispectral Canopy Reflectance Model"*, Remote Sens. Environ., 50 (1994), pp. 75–82.

[78] ——, *"A fast, invertible Canopy Reflectance Model"*, Remote Sens. Environ., 51 (1995), pp. 342–350.

[79] M.-M. KYTÖVITA AND P. CRITTENDEN, *"Effects of simulated acid rain on nitrogenase activity (acetylene reduction) in the lichen Stereocaulon paschale (L.) Hoffm., with special reference to nutrition aspects"*, New Phytol., 128 (1994), pp. 263–271.

[80] J. LENOBLE, *"Atmospheric Radiative Transfer"*, A. Deepak Publishing, 1993.

[81] S. LIANG AND A. H. STRAHLER, *"An Analytic BRDF Model of Canopy Radiative Transfer and its Inversion"*, IEEE Trans. Geosci. Remote Sens., 31 (1993), pp. 1081–1092.

[82] S. LIANG, A. H. STRAHLER, Q. ZHU, AND X. JIN, *"Comparison of radiative transfer models of vegetation canopies and laboratory measurements"*. Manuscript, correspondence: A. Strahler, Center for Remote Sensing, Boston University, MA, USA, 1995.

[83] T. M. LILLESAND AND R. KIEFER, *"Remote Sensing and Image Interpretation"*, Wiley, 1994.

[84] K.-N. LIOU, *"An introduction to Atmospheric Radiation"*, Academic Press, New York, 1980.

[85] R. P. LIPPMANN, *"An introduction to Computing with Neural Nets"*, IEEE ASSP magazine, 4 (1987), pp. 4–24.

[86] R. E. LONGTON, *"Biology of polar bryophytes and lichens"*, Cambridge University Press, Great Britain, 1988.

[87] F. MACINTOSH AND S. JOHN, *"Coherent Backscattering of light in the presence of time-reversal, noninvariant and parity-violating media"*, Phys. Rev. B., 37 (1988), pp. 1884–1897.

[88] H. MARTENS AND T. NÆS, *"Multivariate Calibration"*, Wiley, 1989.

[89] T. C. MEREDITH, *"Spectralradiometry and Caribou Range Classification"*, Rangifer, Special Issue, 1 (1986), pp. 191–194.

[90] A. M. MIKA, *"Three Decades of Landsat Instruments"*, Photogramm. Eng. & Remote Sens. 63 (1997), pp. 839–852.

[91] M. MINNAERT, *"The reciprocity principle in lunar photometry"*, Astrophys. J., 93 (1941).

[92] M.-. I. MISHCHENKO, *"Enhanced backscattering of polarized light from discrete random media:calculations in exactly the backscattering direction"*, J. Opt. Soc. Am. 9 (1992), pp. 978–982.

[93] MOSS, *"Mose produkter"*, Norske Moseprodukter A/S, N-2482 Storsjøen, Norway, 1996.

[94] T. MULHERN, *"Spectral Contrasts of Subarctic Vegetation: Basis for Mapping Lichens with Satellite Data"*, PhD thesis, Geography Department of University of Maryland, College Park, MD,USA, 1995.

[95] R. B. MYNENI AND G. ASRAR, *"Radiative transfer in three-dimensional atmosphere-vegetation media"*, J. Quant. Spectrosc. Radiat. Transfer, 49 (1993), pp. 585–598.

[96] R. B. MYNENI, S. MAGGION, J. IAQUINTA, J. L. PRIVETTI, N. GORDON, B. PINTY, D. KIMES, M. VERSTRAETE, AND D. WILLIAMS, *"Optical Remote Sensing and Vegetation: Modelling, Caveats and Algorithms"*, Remote Sens. Environ., 51 (1995), pp. 169–188.

[97] R. B. MYNENI AND J. ROSS, eds., *"Photon Vegetation Interactions, Applications in Optical Remote Sensing and Plant Ecology"*, Springer-Verlag, 1991.

[98] R. B. MYNENI, J. ROSS, AND G. ASRAR, *"A Review on the Theory of Photon Transport in Leaf Canopies"*, Agricultural and Forest Meteorology, 45 (1989), pp. 1–153.

[99] F. E. NICODEMUS, J. C. RICHMOND, J. HSIA, W. VENABLE, I. GINSBERG, AND T. LIMPERIS, *"Geometrical considerations for Reflectance Nomenclature"*, National Bureau of Standards Report, 160 (1977), pp. 1–52.

[100] T. NILSON AND A. KUUSK, *"A Reflectance Model for the Homogenious Plant Canopy and Its Inversion"*, Remote Sens. Environ., 27 (1989), pp. 157–167.

[101] J. PEÑUELAS, J. A. GAMON, K. L. GRIFFIN, AND C. B. FIELD, *"Assessing Community Type, Plant Biomass, pigment Composition and Photosynthetic Efficiency of Aquatic Vegetation form Spectral Reflectance"*, Remote Sens. Environ., 46 (1993), pp. 110–118.

[102] D. E. PETZOLD AND S. GOWARD, *"Reflectance Spectra of Subarctic Lichens"*, Remote Sens. Environ., 24 (1988), pp. 481–492.

[103] B. PINTY AND D. RAMOND, *"A Simple Bidirectional Reflectance Model for Terrestrial Surfaces"*, J. Geophys. Res. 91 (1986), pp. 7803–7808.

[104] B. PINTY AND M. VERSTRAETE, *"Extracting Information on Surface Properties From Bidirectional Reflectance Measurements"*, J. Geophys. Res. 96 (1991), pp. 2865–2878.

[105] B. PINTY, M. VERSTRAETE, AND R. DICKINSON, *"A physical Model of the Bidirectional Reflectance of Vegetation Canopies 2. Inversion and Validation"*, J. Geophys. Res. 95 (1990), pp. 11767–11775.

[106] P. M. PRENTER, *Splines and Variational Methods*, Wiley, 1989.

[107] W. H. PRESS, S. A. TEUKOLSKY, W. T. VETTERLING, AND B. P. FLANNERY, *"Numerical Recipes in C. The Art of Scientific Computing "*, Cambridge University Press, Second Edition ed., 1992.

[108] J. C. PRICE, *"How Unique are Spectral Signatures?"*, Remote Sens. Environ., 49 (1994), pp. 181–186.

[109] J. L. PRIVETTE, R. G. MYNENI, W. J. EMERY, AND B. PINTY, *"Inversion of soil bidirectional reflectance model for use with vegetation reflectance models"*, J. Geophys. Res. 100 (1995), pp. 22497–25508.

[110] M. C. F. PROCTOR, *"Structure and Eco-physiological Adaptation in Bryophytes"*, in Bryophyte Systematics, G. C. S. Clarke and J. G. Duckett, eds., vol. 14 of The Systematic Association Special Volume, Academic Press, 1979, ch. 20, pp. 479–509.

[111] H. RAHMAN, B. PINTY, AND M. M. VERSTRAETE, *"Coupled Surface Reflectance (CSAR) Model. 2. Semiempirical Surface Model Usable With NOAA Advanced Very High Resolution Radiometer Data"*, J. Geophys. Res. 98 (1993), pp. 20791–20801.

[112] H. RAHMAN, M. M. VERSTRAETE, AND B. PINTY, *"Coupled Surface Reflectance (CSAR) Model. 1. Model Description and Inversion on Synthetic Data"*, J. Geophys. Res. 98 (1993), pp. 20779–20789.

[113] K. J. RANSON, C. S. T. DAUGHTRY, L. L. BIEHL, AND M. E. BAUER, *"Sun-View Angle Effects on Reflectance Factors on Corn Canopies"*, Remote Sens. Environ., 18 (1985), pp. 147–161.

[114] W. REES, *"Physical Principles of Remote Sensing"*, Cambridge University Press, Cambridge, 1990.

[115] D. H. S. RICHARDSON, *"Pollution monitoring with lichens"*, Richmond Publishing Co. Ltd., Slough, England, 1992.

[116] E. M. ROLLIN AND D. R. EMERY, *" Reference panel anisotropy and the significance of diffuse radiation"*, in Physical Measurements and Signatures in Remote Sensing, G. Guyot and T. Phulpin, eds., vol. 1 of Seventh international Symposium on Physical Measurements and Signatures in Remote Sensing, Courchevel, France, April 1997, ISPRS, Balkema Publ. NL, pp. 143–148.

[117] J. ROSS AND A. MARSHAK, *"Monte Carlo Methods"*, in "Photon Vegetation Interactions, Applications in Optical Remote Sensing and Plant Ecology", R. B. Myneni and J. Ross, eds., Springer-Verlag, 1991, ch. 14, pp. 441–464.

[118] J.-L. ROUJEAN, *A tractable physical model of shortwave radiation interception by vegetation canopies*, J. Geophys. Res. 101 (1996), pp. 9523–9532.

[119] J.-L. ROUJEAN, M. LEROY, AND P. L. DESCHAMPS, *"A Bidirectional Model of the Earth's Surface for the Correction of Remote Sensing Data"*, J. Geophys. Res. 97 (1992), pp. 20455–20468.

[120] S. SANDMEIER, C. MÜLLER, B. HOSGOOD, AND G. ANDREOLI, *"Sensitivity studies of bidirectional reflectance data using the EGO/JRC Goniometer facility "*, in Physical Measurements and Signatures in Remote Sensing, G. Guyot and T. Phulpin, eds., vol. 1 of Seventh international Symposium on Physical Measurements and Signatures in Remote Sensing, Courchevel, France, April 1997, ISPRS, Balkema Publ. NL, pp. 357–364.

[121] ——, *"Sensitivity Analysis and Quality Assessment of Laboratory BRDF Data"*, Remote Sens. Environ., 64 (1998), pp. 176–191.

[122] S. SANDMEIER, W. SANDMEIER, K. I.-ITTEN, M. E. SCHAEPMAN, AND T. W. KELLENBERG, *"The Swiss Field-Goniometer System (FIGOS)"*, in Proc. IGARSS'95, Firenze, Italy, July 1995, pp. 2078–2080.

[123] SE590, *"Spectron Engineering Inc., operating manual"*, Spectron Engineering, Inc., 255 Yuma Court, Denver, Colorado 80223, USA, 1984.

[124] P. J. SELLERS, *"Vegetation-Canopy Spectral reflection and Biophysical Processes"*, in Theory and Applications of Optical Remote Sensing, G. Asrar, ed., Wiley, New York, 1989, ch. 8, pp. 297–335.

[125] P. N. SLATER, *"Remote Sensing: Optics and Optical Systems"*, Addison-Wesley, Reading, MA, USA, 1980.

[126] I. SOLHEIM, B. HOSGOOD, G. ANDREOLI, AND J. PIIRONEN, *"Calibration and Characterization of Data from the European Goniometric Facility (EGO)"*, Tech. Rep. EUR 17268 EN, Joint Research Centre (JRC) European Commission, Ispra (VA), Italy, 1996.

[127] I. SOLHEIM, H. TØMMERVIK, AND K. A. HØGDA, *"A Time Study of the Vegetation in Monchegorsk, Russia"*, Tech. Rep. IT2039/2-95, NORUT IT, Tromsø, Norway, 1995.

[128] SPECTRALON, *"Spectralon reference panels"*, Labsphere, Inc., P.O. Box 70, North Sutton, NH 03260, USA, 1997.

[129] A. H. STRAHLER, W. WANNER, Q. ZHU, AND X. JIN, *"Bidirectional Reflectance Modeling of Data from Vegetation Obtained in the Chanchun Solar Simulation Laboratory "*, in Proc. IGARSS'95, Firenze, Italy, July 1995, pp. 1965–1967.

[130] J. SUPRONOWICZ, G. EDWARDS, K. P. B. THOMSON, AND A. VIAU, *"Spectral reflectance of forest understorey in various types of forests within the BOREAS Northern Study Area in Manitoba"*, submitted to Can. Journ. Remote Sens., (1997).

[131] P. H. SWAIN AND S. DAVIS, eds., *"Remote Sensing: The Quantitative Approach"*, McGraw-Hill, New York, 1978.

[132] A. TARANTOLA, *"Inverse Problem Theory"*, Elsevier, 1987.

[133] B. TEGLER AND K. KERSHAW, *"Studies on lichen-dominated systems. XXIII. The control of seasonal rates of net photosynthesis by moisture, light and temperature in Cladonia rangiferina"*, Can. Journ. Remote Sens., 58 (1980).

[134] K. THOME, J. BARKER, P. SLATER, AND S. BIGGER, *"Radiometric Calibration of Landsat"*, Photogramm. Eng. & Remote Sens. 63 (1997), pp. 853–858.

[135] H. TØMMERVIK, B. JOHANSEN, AND A. EIRA, *"Mapping the air pollution impact on the reindeer pastures in the area of Kirkenes, Northern Norway, using satellite remote sensing methods"*, Tech. Rep., NORUT IT, Tromsø, Norway, 1989.

[136] H. TØMMERVIK, B. JOHANSEN, AND I. LAUKNES, *"Use of Airborn casi Spatial Mode Data for Mapping of Sub-Arctic Mountain Heaths in Pasvik, Northern Norway"*, Can. Journ. Remote Sens., 23 (1997), pp. 104–116.

[137] H. TØMMERVIK, B. JOHANSEN, AND J. PEDERSEN, *"Monitoring the effects of air pollution on terrestrial ecosystems in Varanger (Norway) and Nikel-Pechenga (Russia) using remote sensing"*, The Science of the Total Environment, 160/161 (1995), pp. 753–767.

[138] H. TØMMERVIK, M. E. JOHANSEN, J. P. PEDERSEN, AND T. GUNERIUSSEN, *Integration of Remote Sensed and In-Situ Data in an Analysis of the Air Pollution Effects on Terrestrial Ecosystems in the Border Areas Between Norway and Russia*, Environmental Monitoring and Assessment, 49 (1998), pp. 51–85.

[139] S. VÄISÄNEN, *"Effects of air pollution by metal, chemical and fertilizer plants on forest vegetation at Kokkola. W. Finland"*, Ann. Bot. Fennici, 23 (1986), pp. 305–315.

[140] J. VAN DIGGELEN, *"Photometric Properties of Lunar Crater Floors"*, Recherches Astronomiques de l'observatoire d'utrecht XVI, 2, Astronomical observatory, Utrecht, Sternwarte, Utrecht, 1960.

[141] M. VERBRUGGHE AND J. CIERNIEWSKI, *"Effect of Sun and View Geometries on Cotton Bidirectional Reflectance Model"*, Remote Sens. Environ., 54 (1995), pp. 189–197.

[142] W. VERHOEF, *"Light Scattering by Leaf Layers with Application to Canopy Reflectance Modeling:The Sail Model"*, Remote Sens. Environ., 16 (1984), pp. 125–141.

[143] E. VERMOTE, D. TANRÉ, J. L. DEUZE, M. HERMAN, AND J. J. MORCRETTE, *"Second Simulation of the Satellite Signal in the Solar Spectrum (6S): User's Guide"*, Dept. of Geography, Univ. of Maryland, C/O NASA-Goddard Space Flight Center - Code 923, Greenbelt, MD 20771, USA, 2 ed., 1997.

[144] E. F. VERMOTE, D. TANRÉ, J. L. DEUZÉ, M. HERMAN, AND J.-J. MORCRETTE, *"Second Simulation of the Satellite Signal in the Solar Spectrum, 6S:An Overview"*, IEEE Trans. Geosci. Remote Sens., 35 (1997), pp. 675–686.

[145] M. M. VERSTRAETE, *"Radiation Transfer in Plant Canopies: Transmission of Direct Solar Radiation and the Role of Leaf Orientation"*, J. Geophys. Res. 92 (1987), pp. 10985–10995.

[146] ——, *"Retrieving Canopy Properties from Remote sensing Measurements"*, in Imaging Spectrometry - a Tool for Environmental Observations, J. Hill and J. Megier, eds., EEC, EAEC, Brussels and Luxembourg, 1994, pp. 109–123.

[147] M. M. VERSTRAETE, B. PINTY, AND R. DICKINSON, *"A physical Model of the Bidirectional Reflectance of Vegetation Canopies 1. Theory"*, J. Geophys. Res. 95 (1990), pp. 11755–11765.

[148] T. C. VOGELMANN, *"Plant Tissue Optics"*, Annu. Rev. Plant Physiol. Plant Mol. Biol., 44 (1993), pp. 231–251.

[149] T. C. VOGELMANN, J. F. BORNMAN, AND D. J. YATES, *"Focusing of light by leaf epidermal cells"*, Physiologia Plantarum, 98 (1996).

[150] E. A. WALTER-SHEA AND L. L. BIEHL, *"Measuring Vegetation Spectral Properties"*, Remote Sens. Rev. 5 (1990), pp. 179–205.

[151] E. A. WALTER-SHEA, B. L. BLAD, C. J. HAYS, AND M. A. MESARCH, *"Biophysical Properties Affecting Vegetative Canopy Reflectance and Absorbed Photosynthetically Active Radiation at the FIFE Site"*, J. Geophys. Res. 97 (1992), pp. 18925–18934.

[152] E. A. WALTER-SHEA, C. J. HAYS, AND M. A. MESARCH, *"An Improved Goniometer System for Calibrating Field Reference-Reflectance Panels"*, Remote Sens. Environ., 43 (1993), pp. 131–138.

[153] E. A. WALTER-SHEA AND J. M. NORMAN, *"Leaf Optical Properties"*, in "Photon Vegetation Interactions, Applications in Optical Remote Sensing and Plant Ecology", R. B. Myneni and J. Ross, eds., Springer-Verlag, 1991, ch. 8, pp. 229–252.

[154] C. L. WALTHALL, J. M. WELLES, G. CAMPBELL, AND B. L. BLAD, *"Simple equation to approximate the bidirectional reflectance from vegetation canopies and bare soil surfaces"*, Appl. Opt., 24 (1985), pp. 383–387.

[155] W. WANNER, X. LI, AND A. STRAHLER, *"On the derivation of kernel-driven models of bidirectional reflectance"*, J. Geophys. Res. 100 (1995), pp. 21077–21089.

[156] WEBSTER'S, *"Webster's Encyclopedic Unabridged Dictionary of the English Language"*, Gramercy Books, Random House, New York, 1989.

[157] V. R. WEIDNER AND J. J. HSIA, *"Reflection properties of pressed polythetrafluoroethylene powder"*, J. Opt. Soc. Am. 71 (1981), pp. 856–861.

[158] Y.KNYAZIKHIN AND A. MARSHAK, *"Fundamental Equations of Radiative Transfer in Leaf Canopies, and Iterative Methods for Their Solutions"*, in "Photon Vegetation Interactions, Applications in Optical Remote Sensing and Plant Ecology", R. B. Myneni and J. Ross, eds., Springer-Verlag, 1991, ch. 2, pp. 9–43.

[159] A. M. ZOUBIR AND B. BOASHASH, *"The Bootstrap and its Applications in Signal Processing"*, IEEE Signal Processing Magazine, 15 (1998), pp. 56–76.

[160] J. M. ZURADA, *"Introduction to Artificial Neural Systems"*, West, 1992.

Appendix A

Tables

In this appendix we have collected the tables that are discussed in the text. These tables form the basis for several of the figures in this thesis.

A.1 Tables for Chapter 5

If not otherwise is stated, the data in this section is for wavelength $\lambda = 670.200$ nm.

Table A.1: Comparison of SE590 data logged from the left and the right EGO hemisphere. Data from Experiment 52 and 54.

θ_s	ϕ_d	$\hat{r}_{\phi_d,\phi_d+180}$	$(Y_{\phi_d} - Y_{\phi_d+180})$	MAX$(\hat{s}_{half}(y_{\phi_d}, y_{\phi_d+180}))$
10°	0° and 180°	0.99	3.12%	4.43%
30°	150° and 330°	0.99	4.04%	8.17%
30°	120° and 300°	0.97	2.29%	4.75%
30°	90° and 270°	0.93	2.09%	4.31%
30°	60° and 240°	0.99	2.13%	5.95%
30°	30° and 210°	0.99	3.60%	8.14%
30°	0° and 180°	0.85	2.73%	3.77%
60°	0° and 180°	1.00	5.52%	4.63%
60°	90° and 270°	0.67	2.56%	3.18%

Table A.2: Detector zenith test, $\bar{d}$ is the Eucledian distance from the vertical position.

ϕ_d	level	$\bar{d}[cm]$	s_d
0°	1 cm	1.16	0.53
0°	0 cm	1.55	1.13
135°	1 cm	1.99	1.28
135°	0 cm	2.18	2.02
45°	0 cm	1.63	1.05
45°	2 cm	1.51	0.77
45°	1 cm	1.28	0.56
90°	0 cm	2.42	1.84
90°	0 cm	2.34	1.78
90°	0 cm	2.04	1.33
90°	-1 cm	3.02	2.65
90°	1 cm	2.05	1.17
90°	2 cm	2.03	0.97

Table A.3: Detector azimuth test, $\bar{d}$ is the Eucledian distance from the mechanical center point.

θ_d	ϕ_d	$\bar{d}[cm]$	s_d
0°	$\{0, 15, \ldots, 180\}$	1.20	0.31
45°	$\{0, 15, \ldots, 180, 210, \ldots, 345\}$	1.92	0.30
$-45°$	$\{0, 15, \ldots, 180\}$	2.17	0.42
$-70°$	$\{345, 330, \ldots, 210, 165, \ldots, 0\}$	2.99	0.71

Table A.4: The improvement of measurement precision, before and after time-drift correction for the data from Experiment 49

θ_d	95% disp. before	95% disp after	Y_{mid} before	Y_{mid} after
-50	3.2%	1.8%	7711	7712
-45	3.3%	1.8%	7892	7892
-40	3.5%	1.6%	8044	8044
-35	3.2%	1.6%	8131	8131
-30	3.4%	1.7%	8209	8209
-25	3.5%	1.8%	8278	8278
-20	3.5%	1.5%	8314	8314
-15	3.2%	1.4%	8315	8315
-10	3.3%	1.1%	8323	8323
-5	3.4%	1.1%	8307	8306
0	3.2%	0.0%	8247	8247
5	3.3%	0.9%	8112	8112
10	3.1%	1.4%	8066	8066
15	3.1%	1.5%	7997	7996
20	3.0%	1.6%	7931	7931
25	2.8%	1.6%	7876	7877
30	2.8%	1.8%	7834	7834
35	2.8%	2.3%	7831	7832
40	2.5%	2.1%	7807	7808
45	2.6%	2.2%	7774	7774
50	3.0%	2.6%	7698	7704

A.2 Tables for Chapter 7

Table A.5: The average $\overline{rsmn}$ inversion and test errors and their $\alpha = 0.025$ confidence interval. The $\mu_{inversion}$ and μ_{test} are the mean values of the inversion and test $\overline{rmsn}$. EMRPV1 model, randomly drawn samples

Inversion I	$\overline{rmsn}$	$\hat{s}(rmsn)$	Test I	$\overline{rmsn}$	$\hat{s}(rmsn)$	$\alpha = 0.025$ conf. int $\mu_{inversion} - \mu_{test}$
5.	2.652	1.509	652.	13.329	14.617	(6.959 ,14.396)
10.	4.332	1.787	647.	8.114	2.709	(2.961 , 4.603)
15.	5.156	1.624	642.	7.445	2.630	(1.506 , 3.071)
25.	5.191	1.178	632.	6.756	1.344	(1.112 , 2.017)
30.	5.730	1.380	627.	6.650	1.398	(0.423 , 1.417)
50.	5.585	0.953	607.	6.564	1.138	(0.604 , 1.355)
100.	5.954	0.945	557.	6.394	1.141	(0.065 , 0.814)
125.	6.135	0.986	532.	6.269	0.977	(-0.218 , 0.485)
150.	6.056	1.023	507.	6.406	1.154	(-0.040 , 0.740)
175.	6.098	0.939	482.	6.336	0.943	(-0.099 , 0.575)
200.	6.128	0.933	457.	6.334	0.974	(-0.135 , 0.547)
225.	6.221	0.919	432.	6.278	0.996	(-0.286 , 0.400)
300.	6.110	0.979	357.	6.275	0.869	(-0.166 , 0.497)
400.	6.155	0.958	257.	6.224	0.962	(-0.275 , 0.412)
600.	6.150	0.917	57.	6.237	1.045	(-0.264 , 0.439)
650.	6.142	0.894	7.	6.220	1.089	(-0.278 , 0.435)

Table A.6: The average $\overline{rsmn}$ inversion and test error and their $\alpha = 0.025$ confidence interval based on randomly drawn simulated data. The $\mu_{inversion}$ and μ_{test} are the mean values of the inversion and test $\overline{rmsn}$. EMRPV1 model

Inversion I	$\overline{rmsn}$	$\hat{s}(rmsn)$	Test I	$\overline{rmsn}$	$\hat{s}(rmsn)$	$\alpha = 0.025$ conf. int. for $\mu_{inversion} - \mu_{test}$
5.	0.035	0.040	1165.	0.235	0.296	(0.125 , 0.276)
10.	0.063	0.078	1160.	0.124	0.100	(0.029 , 0.093)
15.	0.075	0.064	1155.	0.122	0.098	(0.018 , 0.077)
25.	0.061	0.067	1145.	0.084	0.075	(-0.002 , 0.048)
30.	0.082	0.112	1140.	0.084	0.066	(-0.031 , 0.035)
50.	0.060	0.052	1120.	0.068	0.047	(-0.010 , 0.025)
100.	0.056	0.044	1070.	0.062	0.040	(-0.010 , 0.021)
125.	0.060	0.041	1045.	0.061	0.039	(-0.013 , 0.016)
150.	0.057	0.038	1020.	0.057	0.034	(-0.014 , 0.012)
175.	0.057	0.041	995.	0.061	0.042	(-0.012 , 0.018)
200.	0.057	0.040	970.	0.057	0.036	(-0.014 , 0.014)
225.	0.059	0.037	945.	0.061	0.038	(-0.012 , 0.015)
300.	0.061	0.038	870.	0.060	0.035	(-0.014 , 0.012)
400.	0.061	0.042	770.	0.061	0.037	(-0.014 , 0.014)
600.	0.059	0.038	570.	0.060	0.036	(-0.013 , 0.014)
650.	0.057	0.032	520.	0.059	0.032	(-0.010 , 0.013)

Table A.7: Inverson results of EMRPV1 model, based on all available data.

Target	wavelength	rms	$\hat{r}$	$rms/\bar{\rho}$, %	$\hat{\rho}_0$	$\hat{b}$	$\hat{k}$	$\hat{\bar{\rho}}$
C.stellaris	441 nm	0.0114	0.98	7.5%	0.1790	-0.6998	0.6232	0.1522
F.nivalis	441 nm	0.0104	0.98	7.9%	0.1619	-0.7875	0.5582	0.1310
R.lanug.	441 nm	0.0049	0.95	6.7%	0.0492	-0.1033	0.5213	0.0729
C.stellaris	553 nm	0.0152	0.98	6.1%	0.2813	-0.6049	0.6243	0.2490
F.nivalis	553 nm	0.0187	0.99	5.8%	0.3897	-0.6470	0.6124	0.3243
R.lanug.	553 nm	0.0092	0.94	6.6%	0.0957	-0.0792	0.5710	0.1397
C.stellaris	670 nm	0.0147	0.98	5.8%	0.2813	-0.5917	0.6176	0.2517
F.nivalis	670 nm	0.0183	0.99	5.7%	0.3834	-0.6338	0.6128	0.3226
R.lanug.	670 nm	0.0086	0.95	6.6%	0.0898	-0.0878	0.5504	0.1312
C.stellaris	861 nm	0.0269	0.97	5.4%	0.5256	-0.4001	0.6573	0.4976
F.nivalis	861 nm	0.0238	0.98	4.6%	0.5715	-0.4583	0.6396	0.5134
R.lanug.	861 nm	0.0236	0.91	5.4%	0.3465	-0.0821	0.7252	0.4352

Table A.8: The average $\overline{rmsn}$ inversion and test error and their $\alpha = 0.025$ confidence intervals. The $\mu_{inversion}$ and μ_{test} are the mean values of the inversion and test $\overline{rmsn}$, using the VPD model, randomly sampled data.

$\theta_s = 30°$						
Inversion I	$\overline{rmsn}$	$\hat{s}(rmsn)$	Test I	$\overline{rmsn}$	$\hat{s}(rmsn)$	$\alpha = 0.025$ conf. int $\mu_{inversion} - \mu_{test}$
5.	2.835	5.851	305.	10.010	1150.823	(2.207, 12.144)
10.	3.345	5.409	300.	5.547	11.388	(1.604, 2.801)
15.	3.545	3.353	295.	4.943	6.064	(0.949, 1.846)
25.	3.617	2.288	285.	4.319	2.941	(0.367, 1.036)
50.	3.783	3.557	260.	4.086	3.096	(-0.074, 0.680)
75.	3.801	2.992	235.	3.983	3.055	(-0.177, 0.542)
100.	3.933	4.090	210.	4.052	3.877	(-0.293, 0.532)
125.	3.850	2.822	185.	3.925	3.062	(-0.279, 0.430)
150.	3.923	6.763	160.	4.023	6.273	(-0.427, 0.628)
175.	3.933	4.345	135.	4.022	4.492	(-0.345, 0.523)
200.	3.931	6.746	110.	3.979	6.084	(-0.476, 0.571)
225.	3.984	7.107	85.	3.990	7.510	(-0.553, 0.564)
250.	3.845	2.885	60.	3.881	3.382	(-0.330, 0.401)
$\theta_s = 60°$						
5.	3.576	6.262	305.	18.939	4340.830	(5.730, 24.994)
10.	4.482	8.618	300.	14.078	2577.434	(2.167, 17.025)
15.	4.644	4.120	295.	12.059	2130.038	(0.666, 14.164)
25.	4.945	3.348	285.	6.664	54.553	(0.607, 2.830)
50.	5.175	3.037	260.	5.744	3.458	(0.197, 0.941)
75.	5.099	1.214	235.	5.492	1.040	(0.173, 0.612)
100.	5.168	1.025	210.	5.416	1.154	(0.032, 0.463)
125.	5.153	1.046	185.	5.393	1.141	(0.023, 0.456)
150.	5.159	1.016	160.	5.389	1.188	(0.012, 0.446)
175.	5.166	0.955	135.	5.358	1.153	(-0.021, 0.404)
200.	5.200	0.953	110.	5.304	1.215	(-0.111, 0.320)
225.	5.181	0.888	85.	5.355	1.474	(-0.051, 0.399)
250.	5.215	0.990	60.	5.260	1.120	(-0.167, 0.257)

Table A.9: The average $\overline{rmsn}$ inversion and test error and their $\alpha = 0.025$ confidence interval. The $\mu_{inversion}$ and μ_{test} are the mean values of the inversion and test $\overline{rmsn}$, using the VPD model, and evenly sampled data.

$\theta_s = 30°$						
Inversion I	$\overline{rmsn}$	$\hat{s}(rmsn)$	Test I	$\overline{rmsn}$	$\hat{s}(rmsn)$	$\alpha = 0.025$ conf. int $\mu_{inversion} - \mu_{test}$
5.	2.880	7.858	305.	6.357	63.329	(2.245 , 4.710)
10.	3.540	4.899	300.	6.426	270.048	(0.463 ,5.308)
15.	3.718	3.878	295.	4.580	9.269	(0.332 , 1.391)
25.	3.179	6.144	285.	5.231	12.809	(1.416 ,2.688)
50.	3.922	4.809	260.	3.976	4.311	(-0.388 , 0.495)
75.	3.866	3.216	235.	3.903	3.154	(-0.331 , 0.406)
100.	3.657	1.574	210.	3.921	1.833	(-0.005 , 0.534)
125.	4.021	2.617	185.	3.720	2.273	(-0.624 , 0.022)
150.	3.811	1.736	160.	3.765	1.777	(-0.320 , 0.228)
175.	4.059	4.140	135.	3.656	3.079	(-0.795 , -0.010)
200.	3.862	1.823	110.	3.612	1.615	(-0.521 , 0.021)
225.	3.810	1.723	85.	3.658	1.891	(-0.429 , 0.127)
250.	3.858	2.977	60.	3.769	2.750	(-0.439 , 0.260)
$\theta_s = 60°$						
5.	3.174	6.815	305.	7.684	18.582	(3.774 , 5.246)
10.	4.681	5.338	300.	6.421	9.311	(1.181 , 2.299)
15.	4.882	4.731	295.	6.156	6.568	(0.783 , 1.765)
25.	4.426	2.889	285.	6.691	5.639	(1.838 , 2.691)
50.	5.387	8.821	260.	5.824	9.707	(-0.192 , 1.065)
75.	5.707	13.201	235.	6.057	23.045	(-0.530 ,1.229)
100.	5.242	1.180	210.	5.305	0.986	(-0.152 , 0.278)
125.	5.283	1.061	185.	5.212	0.958	(-0.279 , 0.137)
150.	4.925	1.048	160.	5.505	0.974	(0.372 , 0.787)
175.	5.114	1.093	135.	5.353	0.847	(0.036 , 0.443)
200.	5.087	0.864	110.	5.494	1.129	(0.200 , 0.613)
225.	5.547	1.145	85.	4.419	0.668	(-1.325 , -0.932)
250.	5.489	1.045	60.	4.125	0.845	(-1.566 , -1.164)

Table A.10: Inversion results for the VPD model, invrted using all data, $\theta_s = 30°$

Target wavelength	$\hat{\Theta}$ $s(\Theta)$	$\hat{\omega}$ $s(\omega)$	$\hat{\chi}$ $s(\chi)$	$\hat{2r\Lambda}$ $s(2r\Lambda)$	$\overline{rmsn}$ $s(\overline{rmsn})$
F. nivalis	-0.3238	0.3752	0.1687	0.1423	4.2787
441	0.0118	0.0072	0.0037	0.1731	0.1455
F. nivalis	-0.3568	0.7198	0.1690	0.0183	2.7863
553	0.0001	0.0000	0.0001	0.0004	0.0000
F. nivalis	-0.3522	0.7183	0.1577	0.0215	2.8031
670	0.0000	0.0000	0.0000	0.0002	0.0000
F. nivalis	-0.3285	0.8882	0.1809	0.0488	2.6711
861	0.0001	0.0000	0.0001	0.0005	0.0000
C. stellaris	-0.2739	0.4162	0.0350	0.8178	4.3863
441	0.0188	0.0196	0.0073	0.6584	0.0549
C. stellaris	-0.2981	0.6101	0.1030	0.7147	2.9399
553	0.0233	0.0361	0.0077	1.5582	0.0114
C. stellaris	-0.2992	0.6274	0.1089	0.1638	2.7578
670	0.0126	0.0070	0.0012	0.1798	0.1341
C. stellaris	-0.2876	0.8819	0.1415	0.1122	2.4719
861	0.0002	0.0000	0.0002	0.0010	0.0000
R. lanuginosum	-0.0662	0.2482	0.3198	1.1284	5.9297
441	0.0003	0.0004	0.0015	0.0174	0.0002
R. lanuginosum	-0.0486	0.4361	0.2632	1.4309	5.5858
553	0.0024	0.0075	0.0023	0.3143	0.0078
R. lanuginosum	-0.0574	0.4175	0.2887	1.1158	5.9027
670	0.0018	0.0021	0.0010	0.0771	0.0038
R. lanuginosum	-0.1335	0.8795	0.1579	0.1089	2.6703
861	0.0001	0.0000	0.0002	0.0006	0.0000

Table A.11: Inversion results for the VPD modell, inverted using all data, $\theta_s = 60°$

Target wavelength	$\hat{\Theta}$ $s(\Theta)$	$\hat{\omega}$ $s(\omega)$	$\hat{\chi}$ $s(\chi)$	$2\hat{r}\Lambda$ $s(2r\Lambda)$	$\overline{rmsn}$ $s(\overline{rmsn})$
F. nivalis	-0.3190	0.3406	-0.8914	1.1523	5.5209
441	0.0049	0.0058	0.1312	0.2056	0.0323
F. nivalis	-0.3030	0.6228	-0.9314	3.5607	4.2100
553	0.0003	0.0004	0.0477	0.0548	0.0019
F. nivalis	-0.3002	0.6235	-0.9055	3.4796	4.0870
670	0.0002	0.0006	0.0772	0.0248	0.0049
F. nivalis	-0.2812	0.8430	-0.2136	3.8166	4.1964
861	0.0045	0.0038	0.0025	0.4754	0.0340
C. stellaris	-0.3078	0.3783	-0.3928	1.6054	7.6614
441	0.0004	0.0020	0.0413	0.0372	0.0073
C. stellaris	-0.2975	0.5602	-0.3496	1.8046	5.7460
553	0.0004	0.0004	0.0100	0.0232	0.0018
stell	-0.2928	0.5649	-0.4045	1.8484	5.2909
671	0.0002	0.0008	0.0067	0.0284	0.0008
C. stellaris	-0.2669	0.8398	-0.2931	2.8585	4.7038
861	0.0003	0.0004	0.0022	0.0321	0.0002
R. lanuginosum	-0.0608	0.3039	0.1151	1.0043	5.5347
441	0.0087	0.0160	0.0549	0.9479	0.0023
R. lanuginosum	-0.0600	0.4819	0.0517	1.3149	5.6185
553	0.0013	0.0026	0.0085	0.0963	0.0009
R. lanuginosum	-0.0599	0.4628	0.0792	1.4069	5.6892
670	0.0033	0.0082	0.0208	0.3504	0.0153
R. lanuginosum	-0.1014	0.8584	-0.0651	1.6214	4.3398
861	0.0002	0.0003	0.0012	0.0150	0.0001

Appendix B

Experimental Data

In this appendix we provide a summary of all the experiments performed during the NORUT IT EGO campaign, 1996. The experiments can be divided into initial, long and supplementary experiments. A short description of each set of experiments is given below.

B.1 Contents and method

Each experiment is summarized by a table where we give some key numbers on the variability of the data sets. The average distance between the first ($\mathbf{y_i}, i = 1$) and the last ($\mathbf{y}_j, j = I$) measurement is estimated for each data set $\mathbf{Y} = (\mathbf{y}_0, \mathbf{y}_1, .., \mathbf{y}_{I-1})$, where I is the total number of measurements. If the first and the last data measurement does not have the same ϕ, θ_d and θ_s position, the difference is estimated based on the first and the last NADIR measurements in the experiment. The average difference is estimated as:

$$D(\mathbf{y}_i, \mathbf{y}_j) = \frac{200}{L} \sum_{l=1}^{L} \frac{y_i^{\lambda(l)} - y_j^{\lambda(l)}}{(y_i^{\lambda(l)} + y_j^{\lambda(l)})} \tag{B.1}$$

where $\lambda(1) = 409.9$ nm and $\lambda(L) = 991.0$ nm, are the smallest and the largest wavelengths applied in the avereging.

The root mean square error between the first ($\mathbf{y_i}, i = 1$) and the last ($\mathbf{y}_j, j = I$) measurement was estimated by

$$rms(\mathbf{y}_i, \mathbf{y}_j) = \sqrt{\frac{\sum_{l=1}^{L} (y_i^{\lambda(l)} - y_j^{\lambda(l)})^2}{L}} \tag{B.2}$$

The temperature and the humidity listed in the tables, refere to the average temperature and relative humidity recorded inside or on-top-of the target canopies (se Section 4.1 for further details) during the experiments.

In Section B.5 we have included tables giving an overview of the field measurements ackired during the field campaign in 1996.

B.2 Initial measurements

Experiment 1 *test02*

Target: White Spectralon. Reference panel (some data lost)
$FOV = 1^o$, $\theta_s = -55^o$
$\theta_d = \{60^o \text{ to } -60^o \text{ step } 5^o\}$, $\phi = \{0^o, 45^o, 90^o, 135°\}$

Experiment 2 *stela03*

Target: *Cladina stellaris.* Wet, The first ten measurements from nadir, the target was rotated or moved between each measurement.
$FOV = 1°$, $\theta_s = -55°$
$\theta_d = \{60° \text{ to } -60° \text{ step } 5°\}$, $\phi = \{0°, 45°, 90°, 135°\}$

Date	I	time	temp/humidity	I_{nadir}
15/Jul/96	130	1 h 28 min	$22.91°C$ / 98.46%rH	15
ϕ	θ_d	$D(\mathbf{y}_0, \mathbf{y}_{19})$	$rms(\mathbf{y}_0, \mathbf{y}_{19})$	
0°	0°	-3.15%	49.73	

Table B.1: General information on stela03

Experiment 3 *stela04*

Target: *Cladina stellaris.* Wet, same position as stela03
$FOV = 1°$,$\theta_s = -55°$
$\theta_d = \{60° \text{ to } -60° \text{ step } 5°\}$, $\phi = \{0°, 45°, 90°, 135°\}$

Date	I	time	temp/humidity	I_{nadir}
16/Jul/96	122	0 h 54 min	$20.02°C$ / 98.94%rH	8
ϕ	θ_d	$D(\mathbf{y}_1, \mathbf{y}_{121})$	$rms(\mathbf{y}_1, \mathbf{y}_{121})$	
0°	0°	1.41%	20.50	

Table B.2: General information on stela04

Experiment 4 *stela05*

Target: *Cladina stellaris.* Wet, rotated 90° compared to stela04
$FOV = 1°$, $\theta_s = -55°$
$\theta_d = \{60° \text{ to } -60° \text{ step } 5°\}$, $\phi = \{0°, 45°, 90°, 135°\}$

Experiment 5 *halon-g7*

Target: Gray Spectralon. Reference panel
Field of view: 1°, $\theta_s = -55°$
$\theta_d = \{60° \text{ to } -60° \text{ step } 5°\}$, $\phi = \{0°, 45°, 90°, 135°\}$

Date	I	time	temp/humidity	I_{nadir}
16/Jul/96	121	0 h 50 min	21.82°C / 98.88%rH	7
ϕ	θ_d	$D(\mathbf{y}_0, \mathbf{y}_{120})$	$rms(\mathbf{y}_0, \mathbf{y}_{120})$	
0°	0°	1.60%	22.35	

Table B.3: General information on stela05

Date	I	time	temp/humidity	I_{nadir}
16/Jul/96	121	0 h 51 min		7
ϕ	θ_d	$D(\mathbf{y}_0, \mathbf{y}_{120})$	$rms(\mathbf{y}_0, \mathbf{y}_{120})$	
0°	0°	-0.13%	4.80	

Table B.4: General information on halon-g7

Experiment 6 *niva08*

Target: *Flavocetraria nivalis.* Dry on top, wet underneath
$FOV = 1°$, $\theta_s = -55°$
$\theta_d = \{60°$ to $-60°$ step $5°\}$, $\phi = \{0°, 45°, 90°, 135°\}$

Date	I	time	temp/humidity	I_{nadir}
17/Jul/96	121	0 h 50 min	28.12°C / 60.86%rH	7
ϕ	θ_d	$D(\mathbf{y}_0, \mathbf{y}_{120})$	$rms(\mathbf{y}_0, \mathbf{y}_{120})$	
0°	0°	-0.92%	12.22	

Table B.5: General information on niva08

Experiment 7 *niva09*

Target: *Flavocetraria nivalis.* Dry on top, wet underneath, rotated 180° , compared to niva08. The last 5 measurements are from nadir, target shifted around.
$FOV = 1°$, $\theta_s = -55°$
$\theta_d = \{60°$ to $-60°$ step $5°\}$, $\phi = \{0°, 45°, 90°, 135°\}$

Experiment 8 *niva10*

Target: *Flavocetraria nivalis.* Dry on top, wet underneath, rotated 90° from niva09 start position.
$FOV = 1°$, $\theta_s = -55°$
$\theta_d = \{60°$ to $-60°$ step $5°\}$, $\phi = \{0°, 45°, 90°, 135°\}$

Experiment 9 *niva11*

Target: *Flavocetraria nivalis.* Dry, same position as niva10
$FOV = 15°$, $\theta_s = -55°$
$\theta_d = \{60°$ to $-60°$ step $5°\}$, $\phi = \{0°, 45°, 90°, 135°\}$

Date	I	time	temp/humidity	I_{nadir}
17/Jul/96	126	1 h 6 min	$27.61°C$ / 62.40%rH	12
ϕ	θ_d	$D(\mathbf{y}_0, \mathbf{y}_{125})$	$rms(\mathbf{y}_0, \mathbf{y}_{125})$	
0°	0°	-1.29%	17.03	

Table B.6: General information on niva09

Date	I	time	temp/humidity	I_{nadir}
17/Jul/96	121	0 h 50 min	$28.60°C$ / 51.42%rH	7
ϕ	θ_d	$D(\mathbf{y}_0, \mathbf{y}_{120})$	$rms(\mathbf{y}_0, \mathbf{y}_{120})$	
0°	0°	-0.73%	9.35	

Table B.7: General information on niva10

Experiment 10 *niva12*

Target: *Flavocetraria nivalis.* Dry, same rotated 180° from niva11
$FOV = 15°$, $\theta_s = -55°$
$\theta_d = \{60°$ to $-60°$ step $5°\}$, $\phi = \{0°, 45°, 90°, 135°\}$

Experiment 11 *gortex13*

Target: GORE–TEX^{TM} reference panel.
$FOV = 15°$, $\theta_s = -55°$
$\theta_d = \{60°$ to $-60°$ step $5°\}$, $\phi = \{0°, 45°, 90°, 135°\}$

Experiment 12 *stela14*

Target: *Cladina stellaris.* Dry on top, wet underneath.
$FOV = 15°$, $\theta_s = -55°$
$\theta_d = \{60°$ to $-60°$ step $5°\}$, $\phi = \{0°, 45°, 90°, 135°\}$

Experiment 13 *gortex09b*

Target: GORE–TEX^{TM} reference panel.
$FOV = 15°$, $\theta_s = -60°$
$\theta_d = \{-70°$ to $70°$ step $5°\}$, $\phi = \{0°, 45°, 90°, 135°\}$

Experiment 14 *gortex10b*

Date	I	time	temp/humidity	I_{nadir}
17/Jul/96	121	0 h 50 min	$25.88°C$ / 59.42%rH	7
ϕ	θ_d	$D(\mathbf{y}_0, \mathbf{y}_{120})$	$rms(\mathbf{y}_0, \mathbf{y}_{120})$	
0°	0°	2.54%	19.63	

Table B.8: General information on niva11

Date	I	time	temp/humidity	I_{nadir}
17/Jul/96	121	0 h 50 min	23.59°C / 65.80%rH	7
ϕ	θ_d	$D(\mathbf{y}_0, \mathbf{y}_{120})$	$rms(\mathbf{y}_0, \mathbf{y}_{120})$	
0°	0°	-4.63%	52.87	

Table B.9: General information on niva12

Date	I	time	temp/humidity	I_{nadir}
18/Jul/96	121	0 h 50 min		7
ϕ	θ_d	$D(\mathbf{y}_0, \mathbf{y}_{120})$	$rms(\mathbf{y}_0, \mathbf{y}_{120})$	
0°	0°	1.65%	56.28	

Table B.10: General information on gortex13

Target: GORE–TEX^{TM} reference panel.
$FOV = 15°$, $\theta_s = -30°$
$\theta_d = \{-70°$ to $70°$ step $5°\}$, $\phi = \{0°, 45°, 90°, 135°\}$

Experiment 15 *gortex01c*

Target: GORE–TEX^{TM} reference panel.
$FOV = 6°$ with arm, $\theta_s = -30°$
$\theta_d = \{-70°$ to $70°$ step $5°\}$, $\phi = \{0°, 45°, 90°, 135°\}$

Experiment 16 *gortex02c*

Target: GORE–TEX^{TM} reference panel. Measurement 112 to 155 were taken to determine the size of the view area.
$FOV = 6°$ with arm, $\theta_s = -55°$
$\theta_d = \{-70°$ to $70°$ step $5°\}$, $\phi = \{0°, 45°, 90°, 135°\}$

Experiment 17 *stela03c*

Target: *Cladina stellaris*. Dry, last nine measurements are from nadir, with the target shifted (10 cm) between each measurement.
$FOV = 6°$ with arm, $\theta_s = -55°$
$\theta_d = \{-70°$ to $70°$ step $5°\}$, $\phi = \{0°, 45°, 90°, 135°\}$

Experiment 18 *niva04c*

Date	I	time	temp/humidity	I_{nadir}
18/Jul/96	121	0 h 53 min	21.58°C / 73.12%rH	7
ϕ	θ_d	$D(\mathbf{y}_0, \mathbf{y}_{120})$	$rms(\mathbf{y}_0, \mathbf{y}_{120})$	
0°	0°	1.16%	12.45	

Table B.11: General information on stela14

Date	I	time	temp/humidity	I_{nadir}
23/Jul/96	113	0 h 46 min		4
ϕ	θ_d	$D(\mathbf{y}_0, \mathbf{y}_{112})$	$rms(\mathbf{y}_0, \mathbf{y}_{112})$	
0°	−65°	-1.87%	123.95	

Table B.12: General information on gortex09b

Date	I	time	temp/humidity	I_{nadir}
23/Jul/96	113	0 h 51 min		4
ϕ	θ_d	$D(\mathbf{y}_0, \mathbf{y}_{112})$	$rms(\mathbf{y}_0, \mathbf{y}_{112})$	
0°	−70°	-1.00%	43.28	

Table B.13: General information on gortex10b

Target: *Flavocetraria nivalis.* Dry, last nine measurements are from nadir, with the target shifted (10 cm) between each measurement.
$FOV = 6°$ with arm, $\theta_s = -55°$
$\theta_d = \{-70°$ to $70°$ step $5°\}$, $\phi = \{0°, 45°, 90°, 135°\}$

B.3 The long series

Experiment 19 *niva01b*

Target: *Flavocetraria nivalis.* Dry, humid underneath
$FOV = 15°$, $\theta_s = -60°$
$\theta_d = \{-70°$ to $70°$ step $5°\}$
$\phi = \{0°, 5°, 10°, 15°, 30°, 45°, 60°, 90°, 120°, 135°, 150°, 165°, 170°, 175°\}$

Experiment 20 *niva03b*

Target: *Flavocetraria nivalis.* Dry, humid underneath, possible shadow of detector at positions $\phi = 10°$ for $\theta_d \in \{25°, 30°, 35°\}$ and $\phi = 170°$ for $\theta_d \in \{-25°, -30°, -35°\}$
$FOV = 15°$, $\theta_s = -30°$
$\theta_d = \{-70°$ to $70°$ step $5°\}$
$\phi = \{0°, 5°, 10°, 15°, 30°, 45°, 60°, 90°, 120°, 135°, 150°, 165°, 170°, 175°\}$

Experiment 21 *stela05b*

Date	I	time	temp/humidity	I_{nadir}
23/Jul/96	112	0 h 49 min		4
ϕ	θ_d	$D(\mathbf{y}_0, \mathbf{y}_{111})$	$rms(\mathbf{y}_0, \mathbf{y}_{111})$	
0°	−70°	0.52%	52.22	

Table B.14: General information on gortex01c

Date	I	time	temp/humidity	I_{nadir}
23/Jul/96	111	0 h 43 min		4
ϕ	θ_d	$D(\mathbf{y}_{14}, \mathbf{y}_{96})$	$rms(\mathbf{y}_{14}, \mathbf{y}_{96})$	
0°/135°	0°	-1.38%	74.12	

Table B.15: General information on gortex02c

Date	I	time	temp/humidity	I_{nadir}
23/Jul/96	121	0 h 3 min	21.34°C / 99.00%rH	13
ϕ	θ_d	$D(\mathbf{y}_0, \mathbf{y}_{111})$	$rms(\mathbf{y}_0, \mathbf{y}_{111})$	
0°	−70°	-0.82%	6.25	

Table B.16: General information on stela03c

Target: *Cladina stellaris.* Dry, possible shadow of detector at position $\phi = 10°$ for $\theta_d \in \{25°, 30°, 35°\}$ and $\phi = 170°$ for $\theta_d \in \{-25°, -30°, -35°\}$
$FOV = 15°$, $\theta_s = -30°$
$\theta_d = \{-70°$ to $70°$ step $5°\}$
$\phi = \{0°, 5°, 10°, 15°, 30°, 45°, 60°, 90°, 120°, 135°, 150°, 165°, 170°, 175°\}$

Experiment 22 *stela07b*

Target: *Cladina stellaris.* Dry
$FOV = 15°$, $\theta_s = -60°$
$\theta_d = \{-70°$ to $70°$ step $5°\}$
$\phi = \{0°, 5°, 10°, 15°, 30°, 45°, 60°, 90°, 120°, 135°, 150°, 165°, 170°, 175°\}$

Experiment 23 *niva05c*

Target: *Flavocetraria nivalis.* Dry
$FOV = 6°$ with arm, $\theta_s = -60°$
$\theta_d = \{-70°$ to $70°$ step $5°\}$
$\phi = \{0°, 5°, 10°, 15°, 30°, 45°, 60°, 90°, 120°, 135°, 150°, 165°, 170°, 175°\}$

Experiment 24 *niva07c*

Target: *Flavocetraria nivalis.* Dry. Time reference of first 198 measurements lost.
$FOV = 6°$ with arm, $\theta_s = -30°$
$\theta_d = \{-70°$ to $70°$ step $5°\}$
$\phi = \{0°, 5°, 10°, 15°, 30°, 45°, 60°, 90°, 120°, 135°, 150°, 165°, 170°, 175°\}$

Date	I	time	temp/humidity	I_{nadir}
23/Jul/96	121	0 h 55 min	21.44°C / 90.68%rH	13
ϕ	θ_d	$D(\mathbf{y}_0, \mathbf{y}_{111})$	$rms(\mathbf{y}_0, \mathbf{y}_{111})$	
0°	−70°	0.79%	12.57	

Table B.17: General information on niva04c

Date	I	time	temp/humidity	I_{nadir}
19/Jul/96	394	3 h 12 min	$21.89°C$ / 70.65%rH	14
ϕ	θ_d	$D(\mathbf{y}_0, \mathbf{y}_{393})$	$rms(\mathbf{y}_0, \mathbf{y}_{393})$	
0°	−70°	2.31%	9.43	

Table B.18: General information on niva01b

Date	I	time	temp/humidity	I_{nadir}
19/Jul/96	391	2 h 58 min	$22.78°C$ / 68.45%rH	14
ϕ	θ_d	$D(\mathbf{y}_0, \mathbf{y}_{381})$	$rms(\mathbf{y}_0, \mathbf{y}_{381})$	
0°	−70°	2.45%	39.26	

Table B.19: General information on niva03b

Experiment 25 *stela08c*

Target: *Cladina stellaris.* Dry, the $\phi = 0°$ and $\phi = 180°$ is the same slice with the detector upside down. Time reference of first 193 measurements lost.
$FOV = 6°$ with arm, $\theta_s = -30°$
$\theta_d = \{-70°$ to $70°$ step $5°\}$
$\phi = \{0°, 5°, 10°, 15°, 30°, 45°, 60°, 90°, 120°, 135°, 150°, 165°, 170°, 175°, 180°\}$

Experiment 26 *stela09c*

Target: *Cladina stellaris.* Dry
$FOV = 6°$ with arm, $\theta_s = -60°$
$\theta_d = \{-70°$ to $70°$ step $5°\}$
$\phi = \{0°, 5°, 10°, 15°, 30°, 45°, 60°, 90°, 120°, 135°, 150°, 165°, 170°, 175°\}$

Experiment 27 *racom10c*

Target: *Racomitrium lanuginosum.* Moss, dry, time reference of first 193 measurements lost
$FOV = 6°$ with arm, $\theta_s = -60°$
$\theta_d = \{-70°$ to $70°$ step $5°\}$
$\phi = \{0°, 5°, 10°, 15°, 30°, 45°, 60°, 90°, 120°, 135°, 150°, 165°, 170°, 175°, 180°\}$

Experiment 28 *racom11c*

Date	I	time	temp/humidity	I_{nadir}
22/Jul/96	391	3 h 6 min	$20.15°C$ / 98.62%rH	14
ϕ	θ_d	$D(\mathbf{y}_0, \mathbf{y}_{381})$	$rms(\mathbf{y}_0, \mathbf{y}_{381})$	
0°	−70°	2.95%	27.25	

Table B.20: General information on stela05b

Date	I	time	temp/humidity	I_{nadir}
22/Jul/96	392	2 h 38 min	20.95°C / 98.92%rH	14
ϕ	θ_d	$D(\mathbf{y}_{35}, \mathbf{y}_{381})$	$rms(\mathbf{y}_{35}, \mathbf{y}_{381})$	
5°/175°	0°	0.96%	47.49	

Table B.21: General information on stela07b

Date	I	time	temp/humidity	I_{nadir}
24/Jul/96	393	2 h 49 min	21.32°C / 71.16%rH	14
ϕ	θ_d	$D(\mathbf{y}_0, \mathbf{y}_{392})$	$rms(\mathbf{y}_0, \mathbf{y}_{392})$	
0°	−70°	-0.31%	7.47	

Table B.22: General information on niva05c

Target: *Racomitrium lanuginosum.* Moss, dry
$FOV = 6°$ with arm, $\theta_s = -60°$
$\theta_d = \{-70°$ to $70°$ step $5°\}$
$\phi = \{0°, 5°, 10°, 15°, 30°, 45°, 60°, 90°, 120°, 135°, 150°, 165°, 170°, 175°\}$

Experiment 29 *gortex01d*

Target: GORE–TEX^{TM} reference panel
$FOV = 6°$ with arm, $\theta_s = -60°$
$\theta_d = \{-70°$ to $70°$ step $10°\}$
$\phi = \{0°, 5°, 10°, 15°, 30°, 45°, 60°, 90°, 120°, 135°, 150°, 165°, 175°\}$

Experiment 30 *gortex02d*

Target: GORE–TEX^{TM} reference panel, additions to gortex01c
$FOV = 6°$ with arm, $\theta_s = -30°$
$\theta_d = \{-70°$ to $70°$ step $10°\}$
$\phi = \{5°, 15°, 30°, 45°, 60°, 75°, 120°, 150°, 165°, 175°\}$

Experiment 31 *gortex30*

Target: GORE–TEX^{TM} reference panel, combination of gortex01c and gortex02d
$FOV = 6°$ with arm, $\theta_s = -30°$
$\theta_d = \{-70°$ to $70°$ step $10°\}$
$\phi = \{5°, 15°, 30°, 45°, 60°, 75°, 120°, 150°, 165°, 175°\}$
$\theta_d = \{-70°$ to $70°$ step $5°\}$
$\phi = \{0°, 45°, 90°, 135°\}$

Date	I	time	temp/humidity	I_{nadir}
24/Jul/96	394			
ϕ	θ_d	$D(\mathbf{y}_{23}, \mathbf{y}_{369})$	$rms(\mathbf{y}_{14}, \mathbf{y}_{369})$	
5°/175°	0°	-3.98%	93.61	

Table B.23: General information on niva07c

Date	I	time	temp/humidity	I_{nadir}
25/Jul/96	417			
ϕ	θ_d	$D(\mathbf{y}_{14}, \mathbf{y}_{402})$	$rms(\mathbf{y}_{14}, \mathbf{y}_{402})$	
0°/180°	0°	-1.73%	47.00	

Table B.24: General information on stela08c

Date	I	time	temp/humidity	I_{nadir}
25/Jul/96	393	2 h 42 min	21.45°C / 99.01%rH	14
ϕ	θ_d	$D(\mathbf{y}_0, \mathbf{y}_{392})$	$rms(\mathbf{y}_0, \mathbf{y}_{392})$	
0°	−70°	-0.76%	10.69	

Table B.25: General information on stela09c

B.4 Supplementary measurements

Experiment 32 *gortex03d*

Target: GORE–TEX^{TM} reference panel
$FOV = 6°$ with arm, $\theta_s = -10°$
$\theta_d = \{-70°$ to $70°$ step $10°\}$, $\phi = \{0°, 45°, 90°\}$

Experiment 33 *racom04d*

Target: *Racomitrium lanuginosum.* Moss, dry, $FOV = 6°$ with arm
$\theta_s = \{-60°, -50°, -40°, -20°, -10°\}$
$\theta_d = \{-70°$ to $70°$ step $10°\}$, $\phi = \{0°, 45°, 90°\}$

Experiment 34 *racom05d*

Target: *Racomitrium lanuginosum.* Moss, wet at start of experiment.
$FOV = 6°$ with arm,$\theta_s = \{-30°, -60°\}$
$\theta_d = \{-70°$ to $70°$ step $10°\}$, $\phi = \{0°, 45°, 90°\}$

Experiment 35 *racom06d*

Target: *Racomitrium lanuginosum.* Moss, wet at start of experiment, rotated 90°
$FOV = 6°$ with arm, $\theta_s = \{-30°, -60°\}$
$\theta_d = \{-70°$ to $70°$ step $10°\}$, $\phi = \{0°, 45°, 90°\}$

Date	I	time	temp/humidity	I_{nadir}
26/Jul/96	418			
ϕ	θ_d	$D(\mathbf{y}_{14}, \mathbf{y}_{403})$	$rms(\mathbf{y}_{14}, \mathbf{y}_{403})$	
0°/180°	0°	-2.77%	109.67	

Table B.26: General information on racom10c

Date	I	time	temp/humidity	I_{nadir}
26/Jul/96	393	2 h 57 min	22.99°C / 67.42%rH	14
ϕ	θ_d	$D(\mathbf{y}_0, \mathbf{y}_{392})$	$rms(\mathbf{y}_0, \mathbf{y}_{392})$	
0°	−70°	1.83%	29.19	

Table B.27: General information on racom11c

Date	I	time	temp/humidity	I_{nadir}
29/Jul/96	188	1 h 50 min		13
ϕ	θ_d	$D(\mathbf{y}_0, \mathbf{y}_{187})$	$rms(\mathbf{y}_0, \mathbf{y}_{187})$	
0°	−70°	-1.60%	144.06	

Table B.28: General information on goretex01d

Experiment 36 *stela07d*

Target: *Cladina stellaris* Dry
$FOV = 6°$ with arm, $\theta_s = \{60°, 50°, 40°, 20°, 10°\}$
$\theta_d = \{-70°$ to $70°$ step $10°\}$, $\phi = \{0°, 45°, 90°\}$

Experiment 37 *niva08d*

Target: *Flavocetraria nivalis.* Dry
$FOV = 6°$ with arm, $\theta_s = \{60°, 50°, 40°, 20°, 10°\}$
$\theta_d = \{-70°$ to $70°$ step $10°\}$, $\phi = \{0°, 45°, 90°\}$

Experiment 38 *stela09da*

Target: *Cladina stellaris.* Lichen, wet
$FOV = 6°$ with arm, $\theta_s = \{-30°, -60°\}$
$\theta_d = \{-70°$ to $70°$ step $10°\}$, $\phi = \{0°, 45°, 90°\}$

Experiment 39 *stela09db*

Target: *Cladina stellaris.* Lichen, wet, rotated 90° from stela09da
$FOV = 6°$ with arm, $\theta_s = \{-30°, -60°\}$
$\theta_d = \{-70°$ to $70°$ step $10°\}$, $\phi = \{0°, 45°, 90°\}$

Experiment 40 *niva10da*

Date	I	time	temp/humidity	I_{nadir}
29/Jul/96	148	1 h 34 min		10
ϕ	θ_d	$D(\mathbf{y}_7, \mathbf{y}_{140})$	$rms(\mathbf{y}_7, \mathbf{y}_{140})$	
0°	5°/175°	-0.68%	116.65	

Table B.29: General information on gortex02d

Date	I	time	temp/humidity	I_{nadir}
23 and 28/Jul/96	412			
ϕ	θ_d	$D(\mathbf{y}_7, \mathbf{y}_{253})$	$rms(\mathbf{y}_7, \mathbf{y}_{253})$	
5°/10°	0°	0.92%	51.72	

Table B.30: General information on gortex30

Date	I	time	temp/humidity	I_{nadir}
29/Jul/96	44	0 h 54 min		4
ϕ	θ_d	$D(\mathbf{y}_8, \mathbf{y}_{38})$	$rms(\mathbf{y}_8, \mathbf{y}_{38})$	
45°	0°	-0.09%	23.76	

Table B.31: General information on gortex03d

Target: *Flavocetraria nivalis.* Lichen, wet
$FOV = 6°$ with arm, $\theta_s = \{-30°, -60°\}$
$\theta_d = \{-70°$ to $70°$ step $10°\}$, $\phi = \{0°, 45°, 90°\}$

Experiment 41 *niva10db*

Target: *Flavocetraria nivalis.* Lichen, wet, rotated 90° from niva10da
$FOV = 6°$ with arm, $\theta_s = \{-30°, -60°\}$
$\theta_d = \{-70°$ to $70°$ step $10°\}$, $\phi = \{0°, 45°, 90°\}$

Experiment 42 *card11d*

Target: Black card, card base dry
$FOV = 6°$ with arm, $\theta_s = \{-10°, -30°, -60°\}$
$\theta_d = \{-70°$ to $70°$ step $10°\}$, $\phi = \{0°, 45°, 90°\}$

Experiment 43 *card12d*

Target: White card, card base dry
$FOV = 6°$ with arm, $\theta_s = \{-10°, -30°, -60°\}$
$\theta_d = \{-70°$ to $70°$ step $10°\}$, $\phi = \{0°, 45°, 90°\}$

Experiment 44 *niva13d*

Target: *Flavocetraria nivalis*, on white card
$FOV = 6°$ with arm, $\theta_s = \{-10°, -30°, -60°\}$
$\theta_d = \{-70°$ to $70°$ step $10°\}$, $\phi = \{0°, 45°, 90°\}$

Date	I	time	temp/humidity	I_{nadir}
30/Jul/96	215	2 h 13 min	21.44°C / 71.27%rH	15
ϕ	θ_d	$D(\mathbf{y}_7, \mathbf{y}_{157})$	$rms(\mathbf{y}_7, \mathbf{y}_{157})$	
0°/90°	0°	-3.12%	35.18	

Table B.32: General information on racom04d

Date	I	time	temp/humidity	I_{nadir}
30/Jul/96	86	0 h 56 min	$23.28°C$ / 73.98%rH	6
ϕ	θ_d	$D(\mathbf{y}_7, \mathbf{y}_{67})$	$rms(\mathbf{y}_7, \mathbf{y}_{67})$	
0°/90°	0°	9.68%	98.35	

Table B.33: General information on racom05d

Date	I	time	temp/humidity	I_{nadir}
30/Jul/96	86	1 h 19 min	$25.19°C$ / 67.16%rH	6
ϕ	θ_d	$D(\mathbf{y}_{25}, \mathbf{y}_{78})$	$rms(\mathbf{y}_{25}, \mathbf{y}_{78})$	
0°/90°	0°	-1.57%	47.74	

Table B.34: General information on racom06d

Experiment 45 *cetra14d*

Target: *Cetraria spp.*, six species of *Cetraria.*
$FOV = 6°$ with arm, $\theta_s = -60°$
θ_d: nadir , $\phi = \{0°, 45°, 90°\}$

Experiment 46 *baseo415d*

Target: Barium Sulphate WP03 70 cm reference panel
$FOV = 6°$ with arm, $\theta_s = \{-10°, -30°, -60°\}$
$\theta_d = \{-70°$ to $70°$ step $10°\}$, $\phi = \{0°, 45°, 90°\}$

Experiment 47 *gortex1e*

Target: GORE–TEX^{TM} reference panel.
After each repetition of positions the panel was either rotated 90° or shifted 15 cm.
$FOV = 6°$ with arm, $\theta_s = \{-30°, -60°\}$
$\theta_d = \{-0°, -10°, -60°\}$, $\phi = \{0°\}$

Experiment 48 *gortex2e*

Target: GORE–TEX^{TM} reference panel.
Time series NADIR. Temperature and lux as auxiliary data.
$FOV = 6°$ with arm, $\theta_s = \{-30°\}$
$\theta_d = \{0°\}$, $\phi = \{0°\}$

Date	I	time	temp/humidity	I_{nadir}
31/Jul/96	215	2 h 1 min	$23.74°C$ / 59.50%rH	15
ϕ	θ_d	$D(\mathbf{y}_7, \mathbf{y}_{157})$	$rms(\mathbf{y}_7, \mathbf{y}_{157})$	
0°/90°	0°	2.84%	20.25	

Table B.35: General information on stela07d

Date	I	time	temp/humidity	I_{nadir}
31/Jul/96	215	2 h 0 min	22.45°C / 58.20%rH	15
ϕ	θ_d	$D(\mathbf{y}_7, \mathbf{y}_{157})$	$rms(\mathbf{y}_7, \mathbf{y}_{157})$	
0°/90°	0°	-1.16%	21.48	

Table B.36: General information on niva08d

Date	I	time	temp/humidity	I_{nadir}
31/Jul/96	76	0 h 42 min	23.89°C / 59.40%rH	6
ϕ	θ_d	$D(\mathbf{y}_7, \mathbf{y}_{67})$	$rms(\mathbf{y}_7, \mathbf{y}_{67})$	
0°/90°	0°	6.47%	54.64	

Table B.37: General information on stela09da

Experiment 49 *gortex3e*

Target: GORE–TEX^{TM} reference panel.
Time series cross plane
$FOV = 6°$ with arm, $\theta_s = \{-30°\}$
$\theta_d = \{-50°$ to $50°$ step $5°\}$, $\phi = \{90°\}$

Experiment 50 *gortex6e*

Target: GORE–TEX^{TM} reference panel.
Time series NADIR, with stabilized power.
$FOV = 6°$ with arm, $\theta_s = \{-30°\}$
$\theta_d = \{0°\}$, $\phi = \{0°\}$

Experiment 51 *gortex6x*

Target: GORE–TEX^{TM} reference panel.
Time series NADIR, with stabilized power, SE590-G1, simultaneous with gortex6e. The SE590-G1 detector head was taped to the SE590.
$FOV = 6°$ with arm, $\theta_s = \{-30°\}$
$\theta_d = \{0°\}$, $\phi = \{0°\}$

Experiment 52 *gortex8e*

Date	I	time	temp/humidity	I_{nadir}
01/Aug/96	86	0 h 55 min	23.89°C / 59.40%rH	6
ϕ	θ_d	$D(\mathbf{y}_{25}, \mathbf{y}_{78})$	$rms(\mathbf{y}_{25}, \mathbf{y}_{78})$	
0°/90°	0°	1.69%	67.16	

Table B.38: General information on stela09db

Date	I	time	temp/humidity	I_{nadir}
01/Aug/96	86	0 h 54 min	20.88°C / 86.04%rH	6
ϕ	θ_d	$D(\mathbf{y}_{22}, \mathbf{y}_{75})$	$rms(\mathbf{y}_{22}, \mathbf{y}_{75})$	
0°/90°	0°	-2.22%	75.47	

Table B.39: General information on niva10da

Date	I	time	temp/humidity	I_{nadir}
01/Aug/96	86	0 h 55 min	21.25°C / 82.38%rH	6
ϕ	θ_d	$D(\mathbf{y}_{25}, \mathbf{y}_{78})$	$rms(\mathbf{y}_{25}, \mathbf{y}_{78})$	
0°/90°	0°	2.58%	102.13	

Table B.40: General information on niva10db

Target: GORE–TEX^{TM} reference panel, stabilized power
Symmetry measurements.
Auxiliary measurements: Lux
$FOV = 6°$ with arm, $\theta_s = \{-10°, -30°\}$
$\theta_d = \{-70°$ to $70°$ step $5°\}$, $\phi = \{0°, 30°, 60°, 90°, 120°, 150°, 180°\}$

Experiment 53 *gortex8x*

Target: GORE–TEX^{TM} reference panel, stabilized power
SE590-G1 mounted on a tripod outside the goniometer, simultaneous measurements with gortex8e and gortex9e. Manually acquired measurements.
$FOV = 6°$

Experiment 54 *gortex9e*

Target:GORE–TEX^{TM} reference panel
Symmetry measurements.
Auxiliary measurements: Lux
$FOV = 6°$ with arm, $\theta_s = \{-60°, -30, -10\}$
$\theta_d = \{-70°$ to $70°$ step $5°\}$, $\phi = \{0°, 90°, 180°, 210°, 240°, 270°, 330°, 300°\}$

Experiment 55 *halon11e*

Target: Halon Withe Panel 05reference panel
Stabilized power
$FOV = 1°$ with arm, $\theta_s = -60°$

Date	I	time	temp/humidity	I_{nadir}
01/Aug/96	129	2 h 55 min		9
ϕ	θ_d	$D(\mathbf{y}_7, \mathbf{y}_{67})$	$rms(\mathbf{y}_7, \mathbf{y}_{67})$	
0°/90°	0°	-9.98%	25.07	

Table B.41: General information on card11d

Date	I	time	temp/humidity	I_{nadir}
01/Aug/96	128	1 h 39 min		11
ϕ	θ_d	$D(y_{52}, y_{112})$	$rms(y_{52}, y_{112})$	
0°/90°	0°	-3.60%	122.5	

Table B.42: General information on card12d

Date	I	time	temp/humidity	I_{nadir}
01/Aug/96	91	1 h 7 min		6
ϕ	θ_d	$D(y_{30}, y_{83})$	$rms(y_{30}, y_{83})$	
0°/90°	0°	-4.30%	131.77	

Table B.43: General information on niva13d

$\theta_d = \{-60°$ to $60°$ step $10°\}$
$\phi = \{0°, 10°, 15°, 30°, 45°, 60°, 90°, 120°, 135°, 150°, 165°, 175°\}$

Experiment 56 *gortex12e*

Target: GORE–TEX^{TM} reference panel
Stabilized power
$FOV = 1°$ with arm, $\theta_s = -60°$
$\theta_d = \{-60°$ to $60°$ step $10°\}$
$\phi = \{0°, 10°, 15°, 30°, 45°, 60°, 90°, 120°, 135°, 150°, 165°, 175°\}$

Experiment 57 *gortex13e*

Target: GORE–TEX^{TM} reference panel
Stabilized power
$FOV = 1°$ with arm, $\theta_s = -30°$
$\theta_d = \{-60°$ to $60°$ step $10°\}$
$\phi = \{0°, 10°, 15°, 30°, 45°, 60°, 90°, 120°, 135°, 150°, 165°, 175°\}$

Experiment 58 *halon14e*

Target: Halon White Panel 05reference panel
Stabilized power
$FOV = 1°$ with arm, $\theta_s = -30°$
$\theta_d = \{-60°$ to $60°$ step $10°\}$
$\phi = \{0°, 10°, 15°, 30°, 45°, 60°, 90°, 120°, 135°, 150°, 165°, 175°\}$

Date	I	time	temp/humidity	I_{nadir}
02/Aug/96	130	1 h 46 min		9
ϕ	θ_d	$D(y_{30}, y_{83})$	$rms(y_{30}, y_{83})$	
0°/90°	0°	-2.16%	119.02	

Table B.44: General information on baseo415d

Date	I	time	temp/humidity	I_{nadir}
9/Sep/96	54	1 h 30 min		18
ϕ	θ_d	$D(\mathbf{y}_0, \mathbf{y}_{48})$	$rms(\mathbf{y}_0, \mathbf{y}_{48})$	
0°	0°	2.77%	186.56	

Table B.45: General information on gortex1e

Date	I	time	temp/humidity	I_{nadir}
13/Sep/96	150	6 h 34 min		150
ϕ	θ_d	$D(\mathbf{y}_0, \mathbf{y}_{149})$	$rms(\mathbf{y}_0, \mathbf{y}_{149})$	
0°	0°	0.38%	42.12	

Table B.46: General information on gortex2e

Experiment 59 *halog15e*

Target: Halon Gray Panel 05reference panel
Stabilized power
$FOV = 1°$ with arm, $\theta_s = -30°$
$\theta_d = \{-60° \text{ to } 60° \text{ step } 10°\}$
$\phi = \{0°, 10°, 15°, 30°, 45°, 60°, 90°, 120°, 135°, 150°, 165°, 175°\}$

Experiment 60 *halon16e*

Target: Halon white Panel 50 x 50. Reference panel
Stabilized power
$FOV = 1°$ with arm, $\theta_s = -30°$
$\theta_d = \{-60° \text{ to } 60° \text{ step } 10°\}$
$\phi = \{0°, 10°, 15°, 30°, 45°, 60°, 90°, 120°, 135°, 150°, 165°, 175°\}$

Experiment 61 *halon17e*

Target: Halon white Panel 05. Reference panel
Stabilized power
$FOV = 1°$ with arm, $\theta_s = -10°$
$\theta_d = \{-60° \text{ to } 60° \text{ step } 10°\}$, $\phi = \{0°, 45°, 90°, 135°\}$

Experiment 62 *gortex18e*

Date	I	time	temp/humidity	I_{nadir}
16/Sep/96	820	8 h and 20 min		
ϕ	θ_d	$D(\mathbf{y}_{31}, \mathbf{y}_{808})$	$rms(\mathbf{y}_{31}, \mathbf{y}_{808})$	
90°	0°	2.85%	164.52	

Table B.47: General information on gortex3e

Date	I	time	temp/humidity	I_{nadir}
18/Sep/96	170	7 h and 15 min		170
ϕ	θ_d	$D(\mathbf{y}_0, \mathbf{y}_{169})$	$rms(\mathbf{y}_0, \mathbf{y}_{169})$	
0°	0°	-2.89%		182.39

Table B.48: General information on gortex6e

Date	I	time	temp/humidity	I_{nadir}
18/Sep/96	155	6 h 40 min		155
ϕ	θ_d	$D(\mathbf{y}_0, \mathbf{y}_{154})$	$rms(\mathbf{y}_0, \mathbf{y}_{154})$	
0°	0°	-3.35%		13.54

Table B.49: General information on gortex6x

Target: GORE–TEX^{TM} reference panel
Stabilized power
$FOV = 1°$ with arm, $\theta_s = -10°$
$\theta_d = \{-60°$ to $60°$ step $10°\}$, $\phi = \{0°, 45°, 90°, 135°\}$

B.5 Field measurements

Date	I	time	temp/humidity	I_{nadir}
25/Sep/96	242	1 h 58 min		10
ϕ	θ_d	$D(\mathbf{y}_{63}, \mathbf{y}_{237})$	$rms(\mathbf{y}_{63}, \mathbf{y}_{237})$	
0°/180°	0°	0.9%	160.47	

Table B.50: General information on gortex8e

Date	I	time	temp/humidity	I_{nadir}
25/Sep/96	502	6 h 15 min		
ϕ	θ_d	$D(\mathbf{y},\mathbf{y})$	$rms(\mathbf{y},\mathbf{y})$	
		-4.68%	18.48	

Table B.51: General information on gortex8e

Date	I	time	temp/humidity	I_{nadir}
25/Sep/96	260	4 h 8 min		9
ϕ	θ_d	$D(\mathbf{y}_{10},\mathbf{y}_{93})$	$rms(\mathbf{y}_{10},\mathbf{y}_{93})$	
		1.08%	49.08	

Table B.52: General information on gortex9e

Date	I	time		I_{nadir}
04/Feb/97	154	1 h 49 min		12
ϕ	θ_d	$D(\mathbf{y}_0,\mathbf{y}_{153})$	$rms(\mathbf{y}_0,\mathbf{y}_{153})$	
0°	−60°	-0.41%	20.64	

Table B.53: General information on halon11e

Date	I	time		I_{nadir}
04/Feb/97	155	2 h 2 min		12
ϕ	θ_d	$D(\mathbf{y}_0,\mathbf{y}_{154})$	$rms(\mathbf{y}_0,\mathbf{y}_{154})$	
0°	−60°	-0.79%	56.53	

Table B.54: General information on gortex12e

Date	I	time		I_{nadir}
05/Feb/97	150			
ϕ	θ_d	$D(\mathbf{y}_0,\mathbf{y}_{149})$	$rms(\mathbf{y}_0,\mathbf{y}_{149})$	
0°	−60°	0.01%	40.59	

Table B.55: General information on gortex13e

Date	I	time		I_{nadir}
05/Feb/97	151			
ϕ	θ_d	$D(\mathbf{y}_0,\mathbf{y}_{150})$	$rms(\mathbf{y}_0,\mathbf{y}_{150})$	
0°	−60°	-0.39%	32.50	

Table B.56: General information on halon14e

Date	I	time		I_{nadir}
06/Feb/97	151			
ϕ	θ_d	$D(\mathbf{y}_0,\mathbf{y}_{150})$	$rms(\mathbf{y}_0,\mathbf{y}_{150})$	
0°	−60°	-0.53%	24.14	

Table B.57: General information on halog15e

Date	I	time		I_{nadir}
06/Feb/97	151			
ϕ	θ_d	$D(\mathbf{y}_0, \mathbf{y}_{150})$	$rms(\mathbf{y}_0, \mathbf{y}_{150})$	
0°	−60°	0.08%	12.01	

Table B.58: General information on halon16e

Date	I	time		I_{nadir}
11/Feb/97	51			
ϕ	θ_d	$D(\mathbf{y}_0, \mathbf{y}_{50})$	$rms(\mathbf{y}_0, \mathbf{y}_{50})$	
0°	−60°	-0.27%	26.41	

Table B.59: General information on halon17e

Date	I	time		I_{nadir}
11/Feb/97	51			
ϕ	θ_d	$D(\mathbf{y}_0, \mathbf{y}_{50})$	$rms(\mathbf{y}_0, \mathbf{y}_{50})$	
0°	−60°	0.16%	22.09	

Table B.60: General information on gortex18e

Target	Name	I	REF($\hat{s}_{abs}$)	TAR($\hat{s}_{abs}$)	FAC($\hat{s}_{abs}$)
mose021	*Racomitrium lanuginosum*	5	1.63%	0.91%	1.65%
mose022	*Racomitrium lanuginosum*	5	7.72%	2.16%	6.66%
mose023	*Racomitrium lanuginosum*	5	3.44%	3.61%	2.20%
mose024	*Racomitrium lanuginosum*	5	5.20%	4.34%	1.70%
graa031	*Racomitrium lanuginosum*	5	4.97%	3.37%	2.09%
graa032	*Racomitrium lanuginosum*	5	3.97%	3.49%	1.73%
graa033	*Racomitrium lanuginosum*	5	3.42%	1.04%	2.59%
graa034	*Racomitrium lanuginosum*	5	2.81%	2.33%	1.08%
graa042	*Racomitrium lanuginosum*	5	3.77%	2.43%	4.81%
graa041	*Racomitrium lanuginosum*	5	8.64%	0.61%	8.32%
vaar043	*Brachythecium albicans*	5	9.58%	1.75%	9.25%
vaar041	*Brachythecium albicans*	2	2.69%	1.22%	3.39%
vaar042	*Brachythecium albicans*	5	5.56%	2.69%	4.75%
vaar044	*Brachythecium albicans*	5	5.83%	4.72%	3.81%
cet021	*Cetraria delisei*	5	8.42%	11.09%	3.63%
cet022	*Cetraria delisei*	5	7.96%	10.09%	3.60%
cet023	*Cetraria delisei*	5	2.69%	4.00%	4.91%
cet024	*Cetraria delisei*	5	4.01%	3.75%	1.64%
cet026	*Cetraria delisei*	5	2.03%	1.92%	2.18%
cet027	*Cetraria delisei*	4	1.19%	0.85%	1.18%
cet025	*Cetraria delisei*	5	7.27%	5.91%	5.66%
gul032	*Flavocetraria nivalis*	5	4.40%	5.82%	2.85%
gul033	*Flavocetraria nivalis*	5	5.45%	4.05%	1.97%
gul034	*Flavocetraria nivalis*	5	4.03%	3.77%	1.78%
gul031	*Flavocetraria nivalis*	5	18.27%	15.32%	4.83%
lys031	*Cladonia arbuscula*	5	3.42%	4.34%	1.90%
lys032	*Cladonia arbuscula*	5	1.94%	2.19%	3.02%
lys033	*Cladonia arbuscula*	5	1.66%	2.67%	2.37%
lys037	*Cladonia arbuscula*	4	1.63%	0.87%	1.58%
lys036	*Cladonia arbuscula*	3	1.09%	1.59%	0.61%
lys035	*Cladonia arbuscula*	4	2.44%	25.33%	24.28%
lys034	*Cladonia arbuscula*	5	7.35%	2.67%	6.34%
grus041	*Gravel*	3	2.85%	0.85%	2.86%
grus044	*Gravel*	5	6.03%	2.32%	7.48%
grus042n	*Gravel*	5	8.69%	2.67%	11.06%
grus043	*Gravel*	5	3.78%	0.62%	3.57%
pol042	*Salix polaris*	5	1.63%	1.50%	1.75%
smell022	*Silene acaulis*	5	8.89%	1.37%	8.19%
smell021	*Silene acaulis*	5	5.48%	4.97%	7.26%

Table B.61: Summary of SE590 data Svalbard

Target	Name	I	REF($\hat{s}_{abs}$)	TAR($\hat{s}_{abs}$)	FAC($\hat{s}_{abs}$)
cet283	*Flavocetraria nivalis*	2	1.34%	0.15%	1.34%
cet286	*Flavocetraria nivalis*	3	3.08%	4.72%	4.47%
cet287	*Flavocetraria nivalis*	3	4.49%	3.47%	4.25%
cet288	*Flavocetraria nivalis*	1	0.00%	0.00%	0.00%
svart283	*Cladina stygia*	5	6.39%	3.81%	4.96%
lys281	*Cladina arbuscula*	4	2.72%	3.07%	0.97%
graa281	*Cladina rangiferina*	2	0.40%	1.00%	0.86%
graa282	*Cladina rangiferina*	5	11.58%	18.13%	6.83%
salt281	*Stereocaulon paschale*	5	5.76%	6.39%	5.44%
kre282	*Empetrum hermaphroditi*	4	24.45%	28.94%	11.92%
salt282	*Stereocaulon paschale*	5	9.00%	3.19%	10.14%
cet282	*Flavocetraria nivalis*	3	2.32%	4.97%	6.87%
svart281	*Cladina stygia*	1	0.00%	0.00%	0.00%
cet281	*Flavocetraria nivalis*	4	31.94%	25.48%	18.88%
cet284	*Flavocetraria nivalis*	2	5.26%	9.44%	14.62%
cet285	*Flavocetraria nivalis*	2	0.61%	11.99%	11.60%
svart282	*Cladina stygia*	5	18.33%	9.61%	11.76%
graa282	*Cladina rangiferina*	5	11.58%	18.13%	6.83%
kre281	*Empetrum hermaphroditi*	3	4.00%	13.25%	12.41%
lys282	*Cladina arbuscula*	5	32.81%	22.06%	17.68%
cet271	*Flavocetraria nivalis*	5	0.24%	0.58%	0.00 %
cet272	*Flavocetraria nivalis*	5	0.65%	0.97%	0.00 %
cet273	*Flavocetraria nivalis*	5	0.68%	1.25%	0.00 %
cet275	*Flavocetraria nivalis*	5	0.17%	1.18%	0.00 %
cet276	*Flavocetraria nivalis*	5	0.51%	1.70%	0.00 %
mix271	*Mixed vegetation*	5	0.88%	0.17%	0.00 %
mix272	*Mixed vegetation*	5	1.14%	3.74%	0.00 %
mix273	*Mixed vegetation*	5	0.24%	6.40%	0.00 %
mix274	*Mixed vegetation*	5	0.52%	1.26%	0.00 %
dverg271	*Betula nana*	5	0.32%	0.67%	0.00 %
dverg272	*Betula nana*	5	0.38%	2.97%	0.00 %
kvitk271	*Cladina stellaris*	5	0.12%	0.48%	0.00 %
kvitk272	*Cladina stellaris*	5	0.25%	0.33%	0.00 %
kvitk273	*Cladina stellaris*	5	0.10%	0.43%	0.00 %
kvitk275	*Cladina stellaris*	5	0.22%	0.24%	0.00 %
kvitk277	*Cladina stellaris*	5	0.33%	0.87%	0.00 %
kvitk278	*Cladina stellaris*	5	0.21%	0.73%	0.00 %
krek271	*Empetrum hermaphroditi*	5	0.21%	0.68%	0.00 %
krek272	*Empetrum hermaphroditi*	5	0.30%	0.56%	0.00 %
krek273	*Empetrum hermaphroditi*	5	1.52%	1.40%	0.00 %
krek274	*Empetrum hermaphroditi*	5	1.02%	1.82%	0.00 %

Table B.62: Summary of SE590 data Finnmark

Date	Target and Coverage	temp(a/g) humidity (a/g/gm)
2/7	*Racomitrium lanuginosum*	3.5/5.0 $C°$, 82/73/84%
2/7	*Cetraria delisei* 65%	4/7 $C°$, 77/65/73%
2/7	*Silene acaulis*	
3/7	*Flavocetraria nivalis*	3.2/3.5 °, 89/90%
3/7	*Flavocetraria nivalis*	3.2/4.7 °, 89/89%
3/7	*Cladonia arbuscula*	/5.8 °, /92%
4/7	Gravel	2.7/3.6 °, 88/85 %
4/7	*Flavocetraria nivalis*	2.7/4.7 °, 88/80/92%
4/7	*Salix polaris*	
4/7	*Aulacomnium turgidum*	3/3.5 °, 88/85%

Table B.63: Summary of temperature and humidity condition for data from Svalbard a-air, g-ground, gm-ground after moistening